Chem Soc Rev

REVIEW ARTICLE

View Article Online
View Journal | View Issue



Cite this: *Chem. Soc. Rev.*, 2025, **54**, 7174

# Advancements and prospects of near-infrared-light driven $CO_2$ reduction reaction†

Siheng Yang,‡[a] Wei Che,‡[b] Yanhua Shao,[b] Woo Jin Byun,[b] Xiaodong Li,[c] Xingchen Jiao,[d] Ruixiang Li,*[a] Jae Sung Lee,[b] Jiaqi Xu*[ae] and Jong-Beom Baek*[b]

In the realm of photoconversion of $CO_2$ into high-value chemicals, the importance of near-infrared (NIR) light is gradually gaining recognition. Relative to ultraviolet (UV) and visible light, NIR light (700–2500 nm), accounting for *ca.* 50% of solar energy, offers unique advantages such as deeper penetration depth and stronger photothermal effects. Thus, utilizing NIR light can not only compensate for the inherent limitations of UV/visible light-based $CO_2$ reduction systems, but also maximize the use of solar energy. However, efficiently harnessing NIR light remains challenging because of its low photon energy, making it difficult to drive $CO_2$ reduction. Additionally, the limited knowledge of the reduction mechanism driven by low-energy photons further hinders progress in this field. In this review, we systematically introduce the motivation and fundamental principles of NIR-light-driven $CO_2$ reduction, the design strategies for NIR-light-activated photocatalysts (including the energy band structure regulation strategy, the energy transfer strategy, and the photothermal utilization strategy), NIR-light absorption mechanisms of these catalysts, and representative applications of these strategies. Finally, we present our perspectives on the challenges facing NIR-light-driven $CO_2$ reduction and provide suggestions for improving current photocatalysts, characterization techniques, evaluation procedures, and potential large-scale applications in future research. With further advancements in NIR-light-driven $CO_2$ reduction, it holds great promise to maximize the exploitation of solar energy, ultimately achieving efficient $CO_2$ photoconversion for industrial applications.

Received 9th October 2024

DOI: 10.1039/d4cs00721b

rsc.li/chem-soc-rev



## 1. Introduction

Global fossil fuel consumption releases around 35 billion tons of $CO_2$ into the atmosphere annually. This amount is nearly double that can be absorbed by the natural carbon sinks, such as forests and oceans (Fig. 1A).[1] As a result, the average global $CO_2$ level has reached 417.06 parts per million (ppm), showing an increase of 2.13 ppm compared to the last year, a rate consistent with the trend observed over the past decade. Currently, atmospheric $CO_2$ levels are 50% higher than they were before the industrial era.[2] The rapid increase of atmospheric $CO_2$ levels has resulted in obvious issues: global warming, abnormal changes in the climate, and the alarming threat of species extinction, all posing serious risks to human existence. For instance, since 1890, the average temperature anomaly has shown a continuous upward trend (Fig. 1B). The issues of global temperature anomalies over land and oceans are primarily linked to the overemission of greenhouse gases from human activities.[3] Therefore, it is crucial to reduce our dependence on fossil fuels and decrease $CO_2$ emissions. While utilizing $CO_2$ as a one-carbon ($C_1$) feedstock for the production of value-added products is recognized as a promising strategy to mitigate these issues, $CO_2$ is a chemically stable molecule ($\Delta_f G^{\circ}_{298K} = -394.36$ kJ mol$^{-1}$) with a strong C=O bond energy of 750 kJ mol$^{-1}$, making it thermodynamically inert and challenging to be activated.[4] Consequently, the chemical conversion of $CO_2$ often requires harsh reaction conditions to drive the energetically uphill reactions. To accomplish efficient $CO_2$ activation, many approaches have been explored, including thermal catalysis, electrocatalysis, photocatalysis,

[a] *Key Laboratory of Green Chemistry & Technology, Ministry of Education, College of Chemistry, Sichuan University, Chengdu, Sichuan 610064, P. R. China. E-mail: liruixiang@scu.edu.cn, jqxu@scu.edu.cn*
[b] *Ulsan National Institute of Science and Technology (UNIST), 50 UNIST, Ulsan 44919, South Korea. E-mail: jbbaek@unist.ac.kr*
[c] *Max Planck Institute of Microstructure Physics, Weinberg 2, Halle 06120, Germany*
[d] *Key Laboratory of Synthetic and Biological Colloids, Ministry of Education, School of Chemical and Material Engineering, Jiangnan University, Wuxi 214122, P. R. China*
[e] *Laboratory of Photonics and Interfaces, École Polytechnique Fédérale de Lausanne, 1015 Lausanne, Switzerland. E-mail: jiaqi.xu@epfl.ch*
† Dedicated to Prof. Michael Grätzel on the occasion of his 80th birthday.
‡ These authors have contributed equally to the work.

photoelectrocatalysis, mechanochemical catalysis, and enzymatic catalysis.[5–13] Among these strategies, harnessing renewable solar energy for photochemically converting $CO_2$ into fine products and fuels is a potential alternative to both mitigate $CO_2$ emissions and meet the global energy demand.

To fully harness solar energy for photocatalytic $CO_2$ conversion, mastery is required not only in the design and synthesis of single component catalysts (composition, nanostructure, *etc.*) but also in the nanoscale assembly of these photocatalytic active units with effective auxiliary nanomaterials. It is reasonable to anticipate that, given the considerable contemporary emphasis on $CO_2$ capture and utilization in the context of carbon neutrality, the coming years will witness significant advancements in $CO_2$ photochemical fixation, including the development of effective light absorption models, synthetic approaches for tailored photocatalysts, and the design of high-efficiency photocatalytic reactors. All of these are developed for the maximal solar energy exploitation and efficient $CO_2$ conversion. To reach the goal, one of the tasks is to fully utilize the low-energy photons from solar light. Although the concept of $CO_2$ photoreduction has existed for a long time, unlike the well-established ultraviolet (UV) or visible light photocatalysis, the utilization of near-infrared (NIR) light for $CO_2$ upgrading has gained prominence only recently. That is because, even though NIR light (700–2500 nm) accounts for *ca.* 50% of the solar spectrum, its low photon energy makes it difficult to drive the uphill $CO_2$ reduction reaction ($CO_2$RR). Consequently, studies on the utilization of NIR light to drive $CO_2$RR are still rare. Meanwhile, the lack of basic understanding of the reaction mechanisms driven by low-energy photons also has resulted in slow progress in this field.

Photocatalysts serve as crucial "tools" in the process of NIR-light-driven $CO_2$RR, where the inherent properties of incident photons dictate how these "tools" are designed and engineered. In this case, precisely matching the characteristics of incident photons and the electronic structures of the photocatalysts is particularly crucial. In this review, we outline the state-of-the-art photocatalysts for NIR-light-driven $CO_2$RR, focusing on the light absorption mechanisms and design strategies of these NIR-light-responsive photocatalysts, and their applications in $CO_2$RR. First of all, we begin with brief discussions on the basic principles of $CO_2$ photoconversion, as

**Siheng Yang**

*Siheng Yang received his bachelor's and master's degrees in Chemistry from Sichuan University under the supervision of Dr Jiaqi Xu and Prof. Ruixiang Li. He is currently a research assistant at Sichuan University. His research interests include the design and fabrication of NIR-light-responsive photocatalysts and their applications in $CO_2$ reduction.*

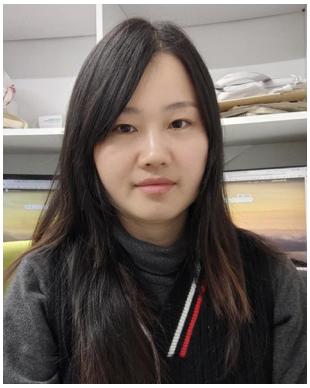

**Wei Che**

*Wei Che received her PhD in 2019 from the University of Science and Technology of China (USTC). After receiving her PhD, she joined the Guangdong University of Technology as a postdoctoral. She is currently a postdoctoral fellow in the School of Energy and Chemical Engineering, Center for Dimension-Controllable Organic Frameworks, at Ulsan National Institute of Science and Technology (UNIST), South Korea. Her current research focuses on photocatalysis for solar energy conversion and advanced organic catalysis.*

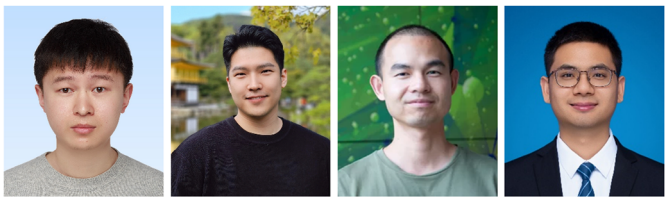

**Left to Right: Yanhua Shao; Woo Jin Byun; Xiaodong Li; Xingchen Jiao**

*Yanhua Shao obtained his PhD degree from Nanjing Tech University under the supervision of Prof. Rizhi Chen. His research focuses on the development of advanced carbon materials based on heterogeneous catalysis. Woo Jin Byun received his PhD from the School of Energy and Chemical Engineering from the UNIST. His research focuses on the development of advanced materials for solar fuel production, including photocatalytic hydrogen production and $CO_2$ reduction. Xiaodong Li received his BS degree from Jilin University (2014) and PhD degree from the USTC (2019). Now he is a postdoc at Max Planck Institute for Microstructure Physics in Germany. His current interests include the theoretical computation, synthesis and characterization of nanostructures and their application in energy storage and conversion. Xingchen Jiao received his BS degree from the Hefei University of Technology (2010) and PhD degree from USTC (2019). In 2022, he joined Jiangnan University as a professor. His current interests include the synthesis and characterization of nanostructures, as well as their applications in $CO_2$ photo-/electro-conversion into hydrocarbon fuels.*

well as the motivation and fundamentals of NIR-light-driven $CO_2$RR, to offer a contextual backdrop. This is followed by a discussion of design strategies for NIR-light-responsive photocatalysts. For instance, NIR light can be directly harnessed to achieve $CO_2$RR through energy band structure regulation strategies, including the construction of narrow-bandgap, intermediate-band, metallic, and heterojunction photocatalysts. Moreover, to enable the indirect utilization of NIR light for $CO_2$RR, energy transfer strategies are proposed, including pure surface plasmon resonance (SPR) systems, SPR-semiconductor synergetic systems, and up-conversion systems. Especially, significant progress focused on photothermal utilization, which can improve conversion and/or yield in the NIR-light-driven $CO_2$ reduction systems, has also been discussed. Finally, we highlight the future directions for constructing advanced NIR-photocatalytic $CO_2$RR systems, including developing an advanced multifunctional photocatalytic system (referred to as a "more-in-one" system), constructing electron-rich sites and enhancing local $CO_2$ concentration for deep $CO_2$RR, and quantifying light and thermal contributions in photothermal $CO_2$RR systems driven by NIR light. To push the advancement of NIR-light-driven $CO_2$RR, we also provide insights into developing advanced techniques, conducting reliable evaluations of catalytic performance, and increasing the feasibility of $CO_2$ photoreduction for practical applications. Throughout the review, we aim to identify the challenges in NIR-light-driven $CO_2$RR, provide feasible design strategies for NIR-responsive photocatalysts, and propose strategic directions for future development in this area.

**Ruixiang Li**

*Ruixiang Li obtained his master's degree and PhD degree from Lanzhou University and City University of Hong Kong, respectively. He is now a professor in the Department of Chemistry, Sichuan University. Prof. Li's research interests include the design and synthesis of homogeneous and heterogeneous catalysts, and green and industrial catalysis.*

**Jae Sung Lee**

*Jae Sung Lee received his BS from Seoul National University in 1975, MS from Korea Advanced Institute of Science and Technology (KAIST) in 1977, and PhD under Prof. Michel Boudart from Stanford University in 1984. Following a brief tenure at Catalytica Inc., he became a professor at POSTECH and later moved to Ulsan National Institute of Science and Technology (UNIST) in 2013. He leads the eco-friendly catalysis and energy laboratory, focusing on photocatalysis for solar energy conversion, electrocatalysis for fuel cells and electrolyzers, and heterogeneous catalysis for $CO_2$ utilization.*

**Jiaqi Xu**

*Jiaqi Xu received his BS degree in Applied Chemistry from Tianjin University in 2014 and PhD degree in Inorganic Chemistry from the University of Science and Technology of China in 2019. He then worked as a postdoctoral fellow at Sichuan University. Currently, he is working as an associate research professor at Sichuan University. In 2024, he joined Prof. Michael Grätzel's lab at École Polytechnique Fédérale de Lausanne as a visiting postdoctoral researcher. His interests include the design and fabrication of low-dimensional materials and their applications in $CO_2$ conversion.*

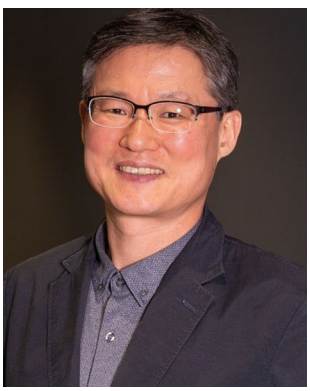

**Jong-Beom Baek**

*Jong-Beom Baek is a distinguished professor of the Department of Energy and Chemical Engineering, and a director of Center for Dimension Controllable Organic Frameworks (CDCOF), at Ulsan National Institute of Science and Technology (UNIST), South Korea. After receiving his PhD from the University of Akron, USA (Polymer Science, 1998), he joined the Wright-Patterson Air Force Research Laboratory (AFRL). He returned to South Korea to take a position as an assistant professor at Chungbuk National University in 2003, before moving to UNIST in 2008. His current research interests include the synthesis of 2D high-performance polymers, chemical modification of carbon-based materials for multifunctional applications, and mechanochemistry for sustainable applications.*

 

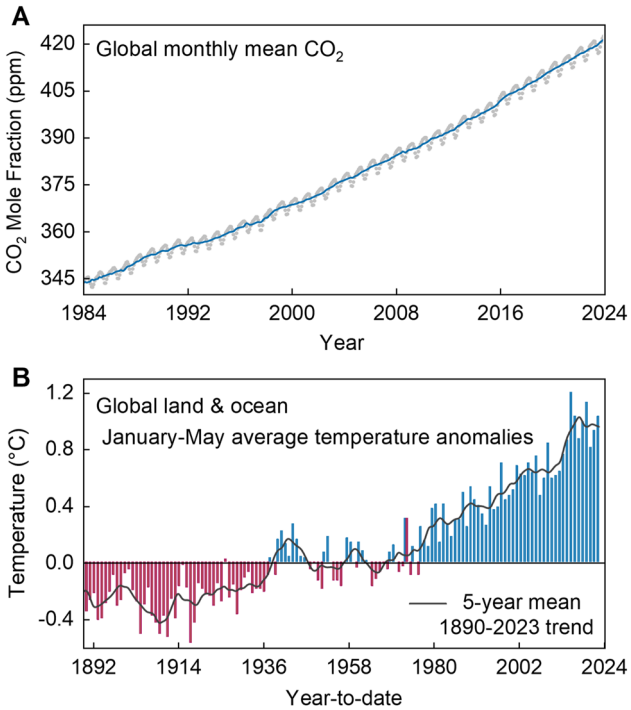


Fig. 1 (A) Global trends in the increase in $CO_2$ concentration are shown *via* globally averaged $CO_2$ mole fraction since 1980. Reproduced with permission from ref. 2. Copyright 2024, NOAA. (B) Global land and ocean average temperature anomalies since 1850. Coordinate anomalies are concerning the 1890–2020 average. Data adapted from the National Ocean and Atmospheric Administration (NOAA) website. Reproduced with permission from ref. 3. Copyright 2024, NOAA.

## 2. Principles and development of photocatalytic $CO_2$ recycling

### 2.1. Principles of photocatalytic $CO_2$ recycling

Utilization of solar energy to construct an efficient artificial carbon cycle holds immense promise for reducing fossil fuel consumption and mitigating climate change (Fig. 2A). In nature, photosynthetic organisms adeptly harness solar energy through intricate supramolecular assemblies to synthesize energy-rich compounds from water and atmospheric $CO_2$.[14] The robust stability and exceptional selectivity of photosynthesis hinge upon the precise spatial arrangement of chromophore molecules and catalytic centers achieved through self-assembly. However, the efficiency of natural photosynthesis is too low to effectively reduce current atmospheric $CO_2$ level on its own. Inspired by photosynthetic organisms, the synthesized photocatalysts have been successfully integrated into the carbon cycle to achieve an artificial photosynthesis process. The widespread adoption of such artificial photosynthesis can facilitate $CO_2$ utilization, lower atmospheric $CO_2$ concentration, and transform $CO_2$ into energy-dense fuels, thus diminishing the reliance on traditional fossil fuels. The underlying mechanism of photosynthesis in nature offers invaluable design principles for developing artificial photosynthesis systems aiming at capturing and storing $CO_2$ on a global scale.

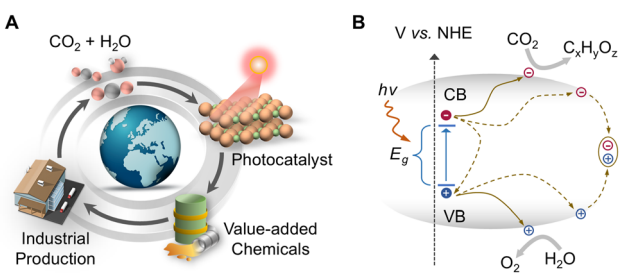


Fig. 2 (A) Scheme of the artificial carbon cycle aiming at upgrading $CO_2$ into value-added chemicals. (B) The diagram of a typical photocatalytic $CO_2$ reduction process on semiconductors.

Photocatalytic $CO_2$ reduction ($PCO_2R$) is a complicated process, which involves a variety of intricate elementary reactions that work together to facilitate $CO_2$ conversion. In a typical $PCO_2R$ process, activated by the incident photons whose energy ($h\nu$) exceeds the energy bandgap ($E_g$) of the catalyst, the electrons in the valence band (VB) will transition to the conduction band (CB), producing active holes and electrons. Most of the electrons and holes suffer from severe recombination either within the bulk material or at the surface. However, a fraction of long-lived photogenerated carriers can successfully transfer to the surface, where they are engaged in the $PCO_2R$ process (Fig. 2B). To enable $CO_2$ reduction, the conduction band minimum (CBM) of the catalyst must be more negative than the $CO_2RR$ potential ($E_{red}$), while its valence band maximum (VBM) is required to be more positive than the water ($H_2O$) oxidation potential ($E_{ox}$) or the oxidation potentials of other substituted agents (*e.g.*, $H_2$[17] and amines[18]) (Table 1). This enables photogenerated electrons to drive the $CO_2$ reduction reaction ($CO_2RR$), while the photogenerated holes drive the oxidation reaction.

Ideally, $H_2O$ oxidation is the recommended oxidation half-reaction for $PCO_2R$. Most cases discussed in this review are based on the water-assisted $PCO_2R$. However, it is sometimes replaced by the oxidation reactions of the reagents that possess lower oxidation potential to enhance the $PCO_2R$ efficiency. One should be aware that the overall reaction of $PCO_2R$ varies according to the oxidation half-reaction, which suggests that

Table 1 Theoretical thermodynamic values (pH = 7) for $CO_2$ photoreduction[a]

| Product | Half reaction | $E^0$/V *vs.* NHE | $\Delta G_{half}$/kJ mol$^{-1}$ |
|---|---|---|---|
| CO | $CO_2 + 2H^+ + 2e^- \rightarrow CO + H_2O$ | −0.53 | 102.29 |
| HCOOH | $CO_2 + 2H^+ + 2e^- \rightarrow HCOOH$ | −0.61 | 117.73 |
| HCHO | $CO_2 + 4H^+ + 4e^- \rightarrow HCHO + H_2O$ | −0.48 | 185.28 |
| $CH_3OH$ | $CO_2 + 6H^+ + 6e^- \rightarrow CH_3OH + 2H_2O$ | −0.38 | 220.02 |
| $CH_4$ | $CO_2 + 8H^+ + 8e^- \rightarrow CH_4 + 2H_2O$ | −0.24 | 185.28 |
| $C_2H_4$ | $CO_2 + 12H^+ + 12e^- \rightarrow C_2H_4 + 4H_2O$ | −0.34 | 393.72 |
| $C_2H_5OH$ | $CO_2 + 12H^+ + 12e^- \rightarrow C_2H_5OH + 3H_2O$ | −0.33 | 382.14 |
| $C_2H_6$ | $CO_2 + 14H^+ + 14e^- \rightarrow C_2H_6 + 4H_2O$ | −0.27 | 364.77 |
| $C_3H_7OH$ | $CO_2 + 18H^+ + 18e^- \rightarrow C_3H_7OH + 5H_2O$ | −0.32 | 555.84 |
| $O_2$ | $1/2O_2 + 2H^+ + 2e^- \rightarrow H_2O$ | +0.82 | −158.26 |

[a] Reproduced with permission from ref. 15. Copyright 2021, Wiley-VCH. Reproduced with permission from ref. 16. Copyright 2022, Wiley-VCH.

the thermodynamics and kinetics may be different as well.[19,20] Due to the diversity of oxidation half-reactions, we will refrain from delving into detailed discussions of specific oxidation half-reactions, in order not to distract the review's focus from the $CO_2$RR half-reaction.

### 2.2. Development of photocatalytic $CO_2$ recycling

Demonstrating artificial photocatalytic $CO_2$ conversion systems with high efficiency, comparable to or even better than natural photosynthesis systems, has been a long-standing dream for scientists. This aspiration has also propelled photocatalysis to become one of the most dynamic fields in chemical research. However, replicating the natural light-harvesting superstructure through synthetic pathways is difficult to achieve and far from cost-effective. In this case, precise modulation of the photocatalyst structure is a highly attractive solution to this challenge. Particularly, regulating the light-harvesting ability by adjusting the electronic structures of catalysts is pivotal for artificial photosynthesis. To efficiently activate the photocatalysts for $CO_2$RR, UV and visible light-driven $CO_2$RR systems have been extensively studied in the past few decades. By contrast, although the concept of NIR photocatalysis has existed for a long time, there are few reports on using NIR irradiation, which comprises about 50% of the solar energy, to enable $CO_2$RR as a result of the low energy of NIR photons (Fig. 3A). The first discovery of heterogeneous photoelectrochemical $CO_2$RR over a *p*-type GaP semiconductor was reported by Halmann[21] in 1978, and the first demonstration of pure photocatalytic $CO_2$RR was presented by Inoue *et al.*[22] in 1979. Since then, light-driven $CO_2$ reduction has attracted broad scientific attention. As shown in Fig. 3B, a cursory search of the term "light driven $CO_2$ reduction" in the Web of Science database indicates significant growth in related research over the last decade, driven by rapid advancements in nanotechnology and characterization techniques.

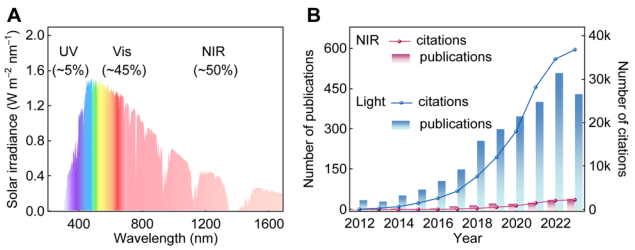


Fig. 3 (A) The solar spectrum primarily comprises visible and NIR light, constituting ~45% and ~50% of the total irradiance, respectively. (B) Publication and citation statistics of photocatalytic $CO_2$ reduction reports for the topics "light driven $CO_2$ reduction" and "infrared light driven $CO_2$ reduction". (Data adapted from the Web of Science, timespan from 2012 to 2023, collected on August 14, 2024.)

Reactors and reaction modes are critical factors for $PCO_2R$. So far, four fundamental reaction modes have been developed: solid–gas mode, solid–vapor mode, solid–gas–liquid mode, and liquid–gas mode (Fig. 4).[23] For both solid–gas and solid–vapor modes, the solid photocatalyst is deposited on a substrate, such as quartz tray[24–26] or foam-type metals,[27,28] to form a catalyst film. Fig. 4A and B display that the solid–gas mode consists of $CO_2$, a catalyst film, and reducing gas (*e.g.*, $H_2$[17,29]), while the solid–vapor mode consists of $CO_2$, a catalyst film, and water vapor,[30,31] with the water vapor being generated from a trace of $H_2O$ at the bottom of the reactor. These modes are relatively simple catalytic systems and their $CO_2$RR activity is strongly

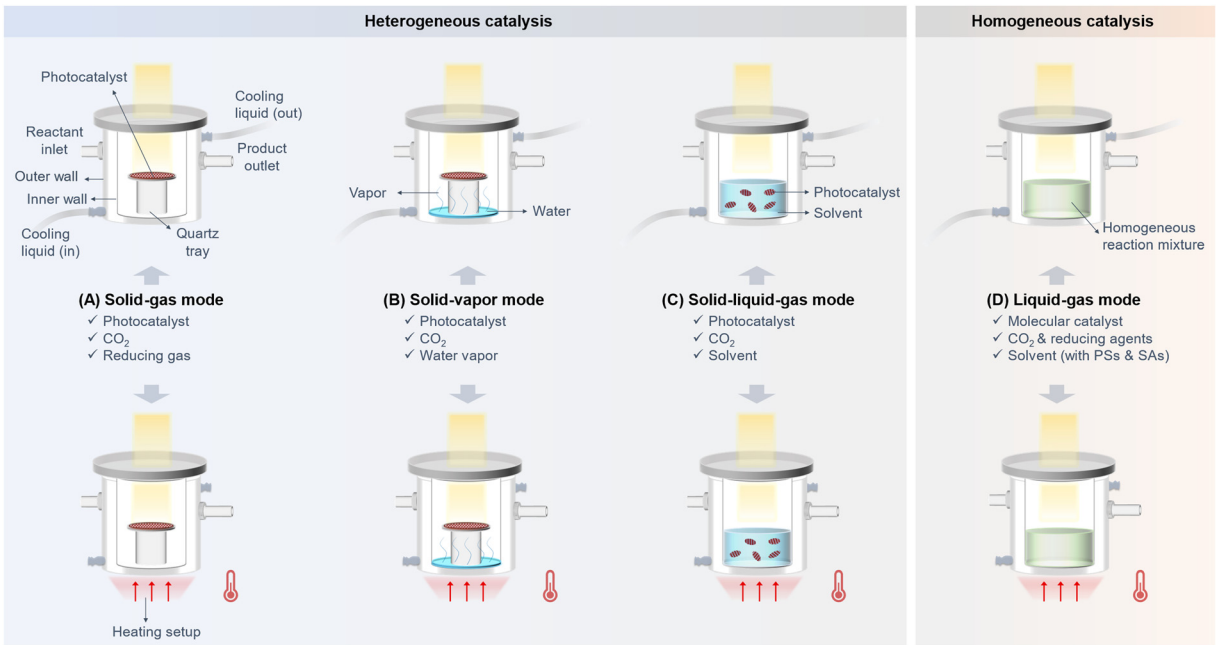


Fig. 4 Different reaction modes for $CO_2$ photoreduction: (A) solid–gas mode, (B) solid–vapor mode, (C) solid–liquid–gas mode, and (D) liquid–gas mode, where PS represents the photosensitizer and SA represents the sacrificial agents.

 

relevant to the intrinsic properties of the catalysts. Different from the solid–gas and solid–vapor modes, the solid–liquid–gas mode involves dispersing the photocatalyst powder in a solvent, where $CO_2$RR occurs at the solid–liquid–gas interface (Fig. 4C).[32] The solvent can be water or organic solvents (*e.g.*, acetonitrile).[18] In this mode, hole sacrificial agents or co-catalysts are sometimes added to the solvent to boost the $CO_2$RR.[33] The liquid–gas mode, on the other hand, is designed for homogeneous $PCO_2R$, where molecular catalysts, organic photosensitizers, reducing agents, and dissolved $CO_2$ are involved (Fig. 4D).[34,35] Based on these four reaction modes, various reactors have been developed as well, including offline batch reactors, online batch reactors, and flow reactors, most of which are kettle type or tubular reactors.[24,27,36–38]

Moreover, a circulating liquid is usually used to dissipate photoinduced heat and keep the system at a steady and low temperature (*e.g.*, 10 °C), which is conducive to investigating the roles of heat and light separately. For instance, Xu *et al.*[25] utilized this method to identify the effect of photoinduced heat on UiO-66/$Co_9S_8$ photocatalysts. As shown in Fig. 5A, after 5 h NIR irradiation, the central temperature of the photocatalyst reaches *ca.* 106 °C, exhibiting a strong photothermal effect. To investigate the role of light and heat, separately, two control experiments are performed: (i) eliminating the photoinduced heat by cycling cool water (Fig. 5B), and (ii) conducting the $PCO_2R$ at 120 °C without light irradiation. When the reaction temperature was held at 10 °C by cycling cool water, the UiO-66/$Co_9S_8$ photocatalyst still exhibited the ability of converting $CO_2$ into $CH_4$, although the $CH_4$ production rate significantly decreased (Fig. 5C). On the other hand, when the $PCO_2R$ was performed at 120 °C without light irradiation, no gas product was observed (Fig. 5D), which indicated that the light

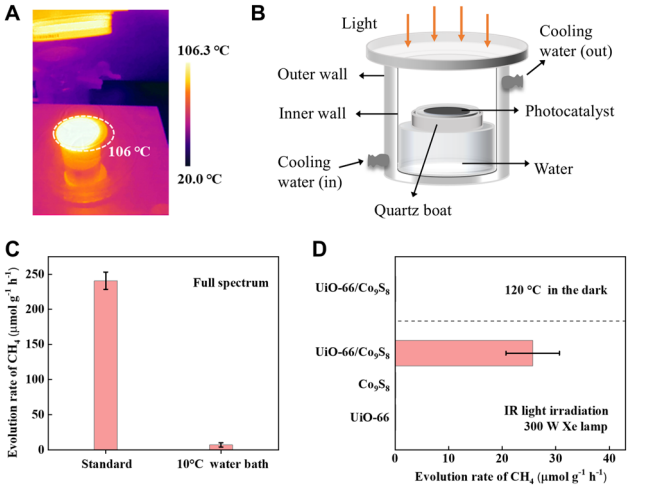


Fig. 5 Identifying the effect of light and heat on UiO-66/$Co_9S_8$. (A) The central temperature of the catalyst after NIR irradiation for 5 h. (B) Typical photoreactor configuration for excluding the photoinduced heat. (C) The influence of photoinduced heat on $PCO_2R$ performance. (D) The $PCO_2R$ performance under standard photothermal catalytic conditions and 120 °C in the dark. Reproduced with permission from ref. 25. Copyright 2024, Wiley-VCH.

illumination was the key factor in triggering the photoreduction of $CO_2$ to $CH_4$, while the photoinduced heat played a vital role in accelerating the reaction.

Also, to enhance photocatalytic efficiency, heating setups can be equipped to provide additional heat, thereby facilitating $CO_2$ photoreduction.[17,29] In addition, novel supports, such as monolith supports[39] and optical fibers,[40,41] have been recently introduced for $PCO_2R$ to ensure sufficient contact between $CO_2$ and photocatalysts as well as uniform light irradiation. Besides, solar concentrators, like Fresnel lens,[27] are usually employed to enhance light absorption and utilization, thereby improving the feasibility of utilizing natural sunlight for $CO_2$RR.

The majority of the materials are only responsive to UV or visible light that possesses high photon energy, and these include metal chalcogenides,[42–45] metal–organic frameworks (MOFs),[18,36,46] and non-metallic materials.[47,48] With the rapid development of reaction modes and reactors, diverse photocatalysts have been explored for $PCO_2R$, such as metal complexes,[34,49,50] metal oxides,[51–53] and metal nitrides,[54–56] for the utilization of NIR light. Given that NIR light constitutes *ca.* 50% of the solar spectrum, enhancing its utilization is crucial for making full use of solar energy during the $PCO_2R$ process. To this end, many researchers have turned their focus on harvesting NIR photons for $PCO_2R$ (Fig. 3B). However, the low energy of NIR light poses significant challenges to its effective use in photocatalysis for an extended period. In 2016, Ye *et al.* introduced a defect level into the band gap of BiOI by constructing oxygen defects, successfully achieving NIR-light-driven transformation of $CO_2$ to CO for the first time.[37] Since then, more and more materials, such as metallic materials,[24,57] SPR materials,[58,59] up-conversion nanoparticles (UCNPs)[60,61] and intermediate-band semiconductors,[62,63] have been developed for driving $CO_2$ conversion by NIR light activation (Fig. 6). These photocatalysts can efficiently harness NIR photons for the transformation of $CO_2$ to high-value chemicals. Besides light absorption ability, $CO_2$ affinity is also a critical property of photocatalysts. With future practical applications in mind, $PCO_2R$ is supposed to be operated under low $CO_2$ concentration atmospheres, which is unfavored by many traditional photocatalysts due to their weak $CO_2$ affinity. Recent studies have demonstrated that photocatalysts with strong NIR light absorption ability, for instance, metallic materials, have the potential to achieve efficient $CO_2$ activation and conversion in the air.[29,64] Moreover, owing to the biocompatibility of NIR light, the NIR-light-driven $CO_2$ reduction can be realized *in vivo*,[65] gradually expanding the applications to biomedical research. Therefore, NIR-light responsive photocatalysts exhibit huge potential for future $CO_2$ photoreduction.

## 3. Motivation and fundamentals of NIR photocatalytic $CO_2$ recycling

### 3.1. NIR light *versus* UV/visible light

As a clean and sustainable energy source, solar light can be utilized to mitigate both energy and environmental challenges.

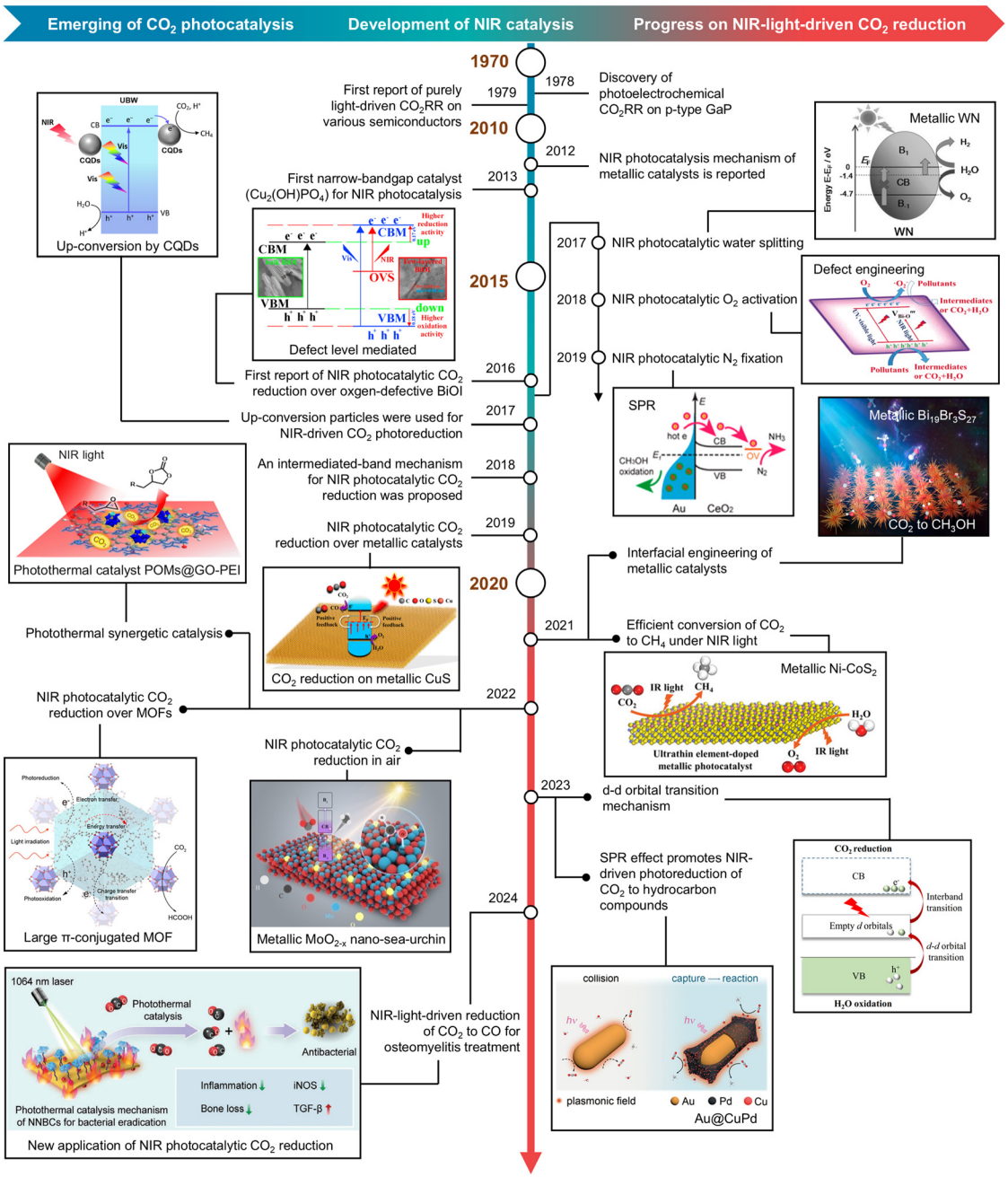


Fig. 6 The timeline highlights key developments in NIR light harvesting and $CO_2$ photoreduction over the past few decades. Reproduced with permission from ref. 21. Copyright 1978, Springer Nature. Reproduced with permission from ref. 22. Copyright 1979, Springer Nature. Reproduced with permission from ref. 66. Copyright 2012, Springer Nature. Reproduced with permission from ref. 67. Copyright 2013, Wiley-VCH. Reproduced with permission from ref. 37. Copyright 2015, Elsevier. Reproduced with permission from ref. 68. Copyright 2017, Springer Nature. Reproduced with permission from ref. 62. Copyright 2018, Elsevier. Reproduced with permission from ref. 57. Copyright 2018, American Chemical Society. Reproduced with permission from ref. 69. Copyright 2017, Wiley-VCH. Reproduced with permission from ref. 70. Copyright 2018, Wiley-VCH. Reproduced with permission from ref. 71. Copyright 2019, American Chemical Society. Reproduced with permission from ref. 72. Copyright 2021, American Chemical Society. Reproduced with permission from ref. 24. Copyright 2021, Wiley-VCH. Reproduced with permission from ref. 73. Copyright 2022, American Chemical Society. Reproduced with permission from ref. 18. Copyright 2022, American Chemical Society. Reproduced with permission from ref. 64. Copyright 2022, Wiley-VCH. Reproduced with permission from ref. 50 and 59. Copyright 2023, Springer Nature. Reproduced with permission from ref. 65. Copyright 2024, Wiley-VCH.

The solar light is composed of about 5% UV light (300–400 nm), about 45% visible light (400–700 nm), and about 50% NIR light (700–2500 nm) (Fig. 3A).[74] In the catalytic system of artificial photosynthesis, light absorption is the first step, directly affecting the solar-to-chemical conversion efficiency (SCC). To date, numerous catalysts have been widely explored for $PCO_2R$, but

the majority of them are triggered only by UV and visible light. Owing to the high energy of UV or visible photons, most photocatalysts can be efficiently activated to generate carriers. Furthermore, photocatalysts with a wide band gap can thermodynamically drive a broader range of reactions, making UV/visible-light photocatalytic systems the most extensively studied photocatalytic systems for $CO_2$RR. Conversely, research on efficient NIR-light-driven $CO_2$ reduction remains in its early stage. Currently, the energy conversion efficiency and economic viability of existing P$CO_2$R systems fall short of industrialization requirements, primarily due to the insufficient utilization of solar energy. This has led researchers to increasingly focus on the exploration of novel NIR-photocatalysts to fully use solar energy. Additionally, there are inherent challenges associated with using UV/visible radiation as a light source. Therefore, it is crucial to thoroughly compare NIR light with UV and visible light, given their significant differences in energy distribution, physicochemical properties, and effects on the earth and life. This comparison is especially important for understanding their roles and significance in P$CO_2$R, forming the foundation for maximizing the utilization of solar energy.

**3.1.1. Penetration depth.** UV or visible light penetrates to shallower depths and is more easily absorbed by the surface of the material, making it more prominent for surface or shallow reactions. However, the limited penetration ability of photons potentially restricts the large-scale operation of the reaction. Besides, the limitation of light penetration also accounts for the slow photocatalytic rate.[75,76] By contrast, NIR light possesses a remarkable penetration depth, leading to a full interaction between reactants and photons.[77,78] As depicted in Fig. 7A, three penetration conditions are considered: (i) catalyst penetration. NIR photons, with their longer wavelengths, can penetrate deeply into bulk catalysts, efficiently activating semiconductor materials to generate charge carriers or thermal energy. (ii) Medium penetration. In photocatalytic systems, infrared light generally has a lower molar absorption coefficient than UV and visible light in the same medium/solution. This results in superior light transmittance and deeper penetration, making NIR especially effective for photoredox reactions.[79,80] (iii) Tissue penetration. Expanding $CO_2$ photoreduction into the biochemical field necessitates the use of "mild" NIR light.[81,82] Unlike UV/visible light, NIR light offers deep tissue penetration depth while minimizing biological tissue damage, offering the opportunity for $CO_2$ conversion within organisms.[65] This penetration feature makes the use of NIR light in photocatalytic reactions potentially advantageous, especially where thicker catalysts are involved or where the reaction depth is large, as NIR light can penetrate the reaction medium to a greater depth.[83] In the actual catalytic process, NIR light is more beneficial for the homogeneous activation of substrates and photocatalysts in the reaction system, which further facilitates the realization of large-scale photocatalytic reactions.

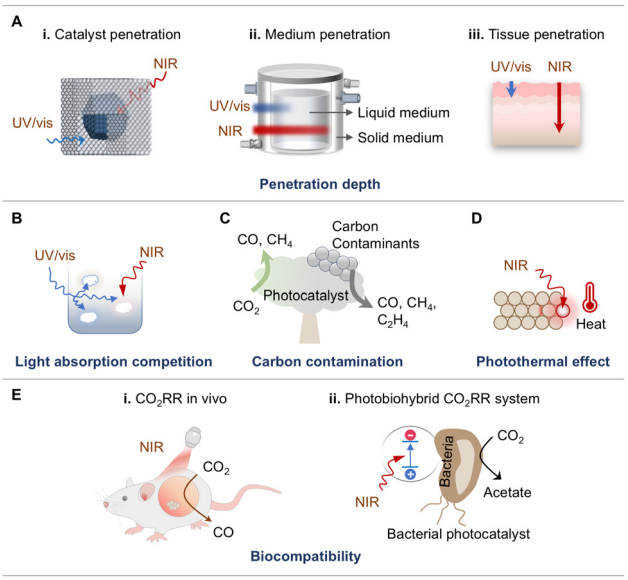


Fig. 7 Comparison of UV/visible light and NIR light. (A) Penetration depth: (i) catalyst penetration, (ii) medium penetration, and (iii) tissue penetration. (B) Light absorption competition. (C) Carbon contamination. (D) Photothermal effect. (E) Biocompatibility: (i) $CO_2$RR *in vivo* and (ii) photobiohybrid $CO_2$RR system.

**3.1.2. Light absorption competition.** Light absorption competition refers to a phenomenon where multiple substances that exist in a system compete for absorption of light from the same light source. UV and visible light are composed of high-energy photons; consequently, the photocatalyst may face competition from the substrate, cocatalyst, solvent, and even the reactor in terms of light absorption, thereby impairing the overall efficiency of photocatalysis.[84–87] Taking the graphene oxide/CdS@TaON photocatalyst as an example, when the ratio of graphene oxide to CdS@TaON becomes sufficiently high, the competitive light absorption between graphene oxide and the active component CdS@TaON becomes more pronounced, leading to a decrease in photocatalytic efficiency.[88] In contrast, NIR photons can reduce the absorption competition due to their low energy (Fig. 7B). We would like to point out that UV/visible photocatalysis is competitive with NIR photocatalysis when considering a fixed number of catalysts. Understanding the light absorption competition in photocatalysis, designing efficient light absorption photocatalysts, and reducing unnecessary light absorption competition are the keys to improving the efficiency of photocatalysis. The development of photocatalysts that selectively absorb specific wavelengths can effectively decrease the absorption competition of other substances and enhance the efficiency of the system. For example, in photocatalysis, using photocatalysts with narrow band gaps for NIR light absorption is a good choice. Recently, photocatalytic $CO_2$ reforming systems operated under NIR light without solvents and sacrificial agents have been highly sought after.[27] Therefore, an irradiation source with low photon energy does not always mean poor photocatalytic activity. NIR light constitutes most of the sunlight spectrum, so it is imperative to explore practical approaches to optimize the activity of the photocatalysts that absorb NIR light, thus minimizing light absorption competition.

**3.1.3. Carbon contamination.** Carbon contamination refers to the products obtained during the P$CO_2$R process that are not

generated from the $CO_2$ feed gas, leading to false-positive results in $PCO_2R$ (Fig. 7C). The sources of carbon contamination in $PCO_2R$ experiments are (i) carbon residues in the experimental setup, (ii) carbon residues on the surfaces of photocatalysts, and (iii) the instability of carbon-based photocatalysts.[89–91] For the first source of carbon pollution, residual carbon typically originates from organic reagents in the gas or inadequately cleaned equipment and reactors. This type of contamination can be effectively eliminated by employing rigorous cleaning procedures before conducting photocatalytic measurements. The second source involves carbon residues left on the photocatalyst surfaces from organic reagents such as solvents, reactants, and surfactants used during the synthesis of photocatalysts. These residues are often difficult to completely remove by washing and can lead to contamination within the system. During catalysis, these residues may convert into carbonaceous compounds, like methane ($CH_4$) and carbon monoxide (CO), which can severely interfere with the analysis of $CO_2$ conversion performance. The third source of contamination arises when carbon-containing photocatalysts decompose under light. This self-decomposition is often more thermodynamically favorable than the $CO_2RR$. For example, MOFs with poor photostability are prone to self-oxidation, which interferes with the analysis of $CO_2RR$ activity.[92]

According to previous reports, wide-bandgap photocatalysts, which require high-energy photons from UV/visible light to generate photocarriers, are more prone to form the products from carbon impurities or even from the carbon-containing photocatalyst itself through oxidation processes rather than through $CO_2$ photoreduction, resulting in false-positive $CO_2RR$ results.[92,93] Therefore, complex and expensive isotope labeling experiments and control experiments are often indispensable to confirm whether the detected products originate from $CO_2$ feedstock or not. By contrast, NIR light exhibits excellent photochemical compatibility and is less likely to generate those pollutants during $PCO_2R$.

Although photocatalysts with narrow bandgaps and NIR light absorption properties have received considerable attention for $CO_2$ photoreduction, there have been no reports of carbon contamination that severely affects the $PCO_2R$ results. The advantages of using NIR light include the following: (1) carbon impurities adsorbed on the surface are less likely to oxidize under low-energy NIR photons, ensuring that the $PCO_2R$ products originate from $CO_2RR$; (2) VB holes excited by NIR light have weaker oxidation capabilities, reducing the likelihood of self-decomposition of carbon-containing photocatalysts and avoiding false-positive $CO_2RR$ signals; and (3) the photothermal effect of NIR light heats the photocatalyst, acting similarly to high-temperature annealing and removing surface-adsorbed carbon impurities.[93] These impurities are rapidly consumed during stability tests at higher temperatures, thus reducing their potential interference with the $PCO_2R$ system.

Therefore, NIR light sources offer a cost-effective and time-efficient means to minimize and eliminate carbon contamination in $CO_2$ photoconversion systems, making NIR-light-driven $CO_2$ reduction a promising approach to avoid or mitigate carbon contamination in photocatalytic processes.

**3.1.4. Photothermal effects.** Benefiting greatly from the joint contributions of light and heat, NIR-light-induced photothermal catalysis has shown immense potential in enhancing chemical reactions that are typically driven solely by thermal energy or light energy (Fig. 7D).[4] The photothermal effects, associated with lattice vibrations and the non-radiative relaxation of carriers, have successfully regulated both electron-related and temperature-related catalytic behaviors in solar-driven $CO_2$-to-chemical processes.[52,94,95] In contrast to UV/visible light, the flux of NIR photons can be effectively channelled into heat to drive reactions, as it can induce non-radiative relaxation processes of carriers, such as Shockley-Read-Hall and Auger recombinations.[96,97] Interestingly, it has been observed that the photothermal $CO_2RR$ performance increases as the light intensity increases, due to the superlinear dependence of photothermal effects on light intensity.[98] Therefore, exploiting catalysts with strong NIR photoactivity and superior photothermal conversion efficiency has emerged as a hot topic in $CO_2$-conversion research.

**3.1.5. Biocompatibility.** High-energy photons, especially in the UV region, will damage the tissues of organisms, and their limited tissue penetration hinders the activation of reactions within deep-seated tissues, thereby limiting their potential in biochemical applications.[99] By contrast, NIR photons featuring low energy and deep penetration depth have shown superiority in converting $CO_2$ within organisms (Fig. 7E).[65] Since the pioneering work on driving $CO_2$ reduction by illuminating NIR light on deep-seated tissues or microorganisms, photocatalysis utilizing NIR energy for $CO_2$ reduction has been demonstrated to display the advantageous features of mild photocatalysis.[65,100] For example, the use of CO as a therapeutic agent has been tested in human clinical trials, with pre-clinical studies showing that CO gas administration provides benefits in animal models of various human diseases. However, developing an effective strategy for safer CO delivery remains a challenge, particularly in ensuring accurate and controlled delivery of CO to patients.[101] Recently, Huang *et al.*[65] made significant strides in this field by utilizing a photothermal $CO_2$-reducing nanocatalyst (abbreviated as NNBC) to convert $CO_2$ into CO within biological organisms under NIR light (1064 nm laser). This *in situ* CO generation proved to inhibit bacterial growth and reduce inflammation in tissues, confirming that NIR-triggered mild photocatalysis holds promise for *in vivo* $CO_2$ conversion. Moreover, due to its high biocompatibility, NIR light is particularly well-suited for biotic $CO_2$ catalysts, with great potential to overcome the challenge posed by the high overpotential required for $CO_2RR$ on inorganic $CO_2$-reducing catalysts.[100] This bio-photoreduction process could be realized in biophotochemical synthesis using $CO_2$-fixing microorganisms, such as members of Chromatiaceae, *Sporomusa ovata*, and *Chlorobium*.[100–102] For instance, Yang *et al.*[101] designed a microorganism (*Sporomusa ovata*)-integrated bias-free photochemical diode device, successfully converting $CO_2$ into multi-carbon ($C_{2+}$) products (*e.g.*, acetate) driven by NIR light (740 nm). This process harnesses NIR light for $CO_2RR$ under mild conditions, showcasing a great foreground in biochemical applications. Its effectiveness and advantages stem from

 

efficient $CO_2$ activation and conversion, enhanced photothermal effects, and mild operating conditions—primarily enabled by the long wavelength, low energy, and deep penetration capabilities of NIR photons. Therefore, expanding light absorption into the NIR region should be a high priority in the design of catalysts and photocatalytic systems.

In short, using NIR light to promote photocatalytic $CO_2$ recovery is mainly based on the following considerations.

**Solar energy utilization**. NIR light makes up a substantial part of solar light. Harnessing NIR light is conducive to maximizing the solar energy utilization for $CO_2$ conversion.

**Technological advancements**. Advancements in synthetic chemistry and characterization techniques ensure the possibility of $CO_2$ photoreduction by low-energy photons, further expanding the methods of $CO_2$ reduction.

**Photocatalytic efficiency**. Broadening the spectrum responsiveness of photocatalysts from the UV to the NIR region will enhance their overall efficiency in converting $CO_2$ into value-added products.

**Environmental and energy concerns**. Given the pressing environmental and energy challenges associated with $CO_2$ emissions, there is a growing imperative to explore novel strategies for $CO_2$ conversion. Utilizing NIR light for catalytic $CO_2$ recovery presents a promising avenue for addressing these concerns while leveraging renewable energy sources.

**Intrinsic advantages of NIR light**. NIR light, with its ability to deeply penetrate reaction media and material surfaces, can uniformly activate the bulk of catalysts. The lower energy of NIR photons helps minimize competitive light absorption and unwanted side reactions. Moreover, NIR light exhibits a unique photothermal effect, which aids in activating $CO_2$ molecules and modulating the selectivity-determining steps in the $PCO_2R$ process. This photothermal conversion enhances the reaction kinetics of $CO_2$ transformation. Additionally, due to their excellent tissue penetration and biocompatibility, NIR photons have found successful applications in biological $CO_2$ conversion systems.

In other words, developing NIR-light-driven photocatalytic systems for $CO_2$ recovery displays advantages in energy utilization, conversion efficiency and technical feasibility. It has great potential to solve the environmental and energy challenges by fully using solar energy from UV to NIR regions.

### 3.2. Fundamentals and challenges of NIR-light-driven $CO_2$ reduction

To accomplish NIR-light-driven $CO_2RR$, photocatalysts must have extremely narrow bandgaps in addition to well-matched band edge positions. Nevertheless, it is hard to simultaneously satisfy both the bandgap and band edge position requirements for NIR-light-driven $CO_2RR$ when designing a photocatalyst (Fig. 8). Because the energy of NIR photons is too low, it cannot excite most of the photocatalysts, which seriously impedes the progress of NIR-light-driven $CO_2RR$. As a result, only a limited number of narrow-bandgap photocatalysts are capable of directly achieving this objective.[62] However, although the narrow-bandgap photocatalysts exhibit excellent NIR light absorption,

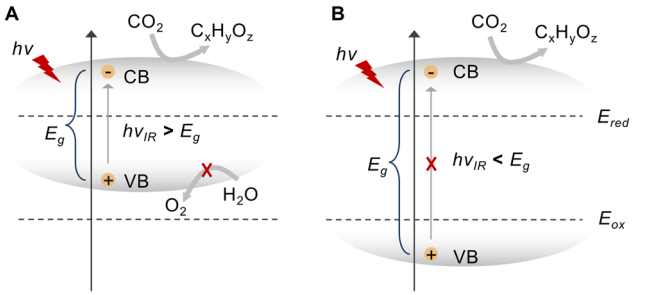


Fig. 8 Paradoxes in NIR-light-driven $CO_2$ reduction systems. (A) Unsuitable band edge position. (B) Unsuitable band gap for light absorption.

they often possess inappropriate band edge positions, making them unable to drive the overall $CO_2RR$.[18] Yet, only a few photocatalysts have been reported to realize NIR-light-driven $CO_2RR$, including oxygen-deficient $WO_3$ and metallic CuS nanosheets, but the efficiencies of these systems are still quite low.[56,57,62] Therefore, precisely tuning the band structures is key to achieving an efficient NIR-light-driven $CO_2RR$.

It is noted that $H_2O$ oxidation is the most recommended half-reaction for $CO_2$ photoreduction systems in overall photocatalysis due to its green and abundant features. For photocatalysts with narrow bandgaps, charge recombination occurs easily, which significantly impairs their overall efficiency. Moreover, such photocatalysts with small bandgaps usually fail to trigger sufficient potential for $H_2O$ oxidation due to their unsuitable VBM position, which further lowers the efficiency of NIR-light-driven $CO_2RR$ or even inhibits the reaction. To resolve these limitations, sacrificial reagents, like triethanolamine (TEOA), $Na_2S$, $Na_2S_2O_3$, *etc.*, are often introduced into the NIR-light-driven $CO_2$ reduction system.[56,60] The oxidation of these sacrificial agents is able to be triggered by a potential lower than that of $H_2O$ oxidation, which can not only overcome the limitation of VBM position but also narrow the required band gap for $CO_2RR$. These sacrificial agents facilitate charge separation by scavenging the holes, greatly promoting the reaction. However, the use of sacrificial agents is costly and environmentally unfriendly. Moreover, the use of sacrificial agents sometimes makes the system more complex, hindering the investigation of the mechanism of NIR-light-driven $CO_2$ reduction. Therefore, careful selection of sacrificial agents is essential for $PCO_2R$ investigation.

Furthermore, the typical $CO_2$ photoreduction assisted by $H_2O$ is an uphill process, and the efficiency of NIR-light-driven $CO_2$ reduction is still undesirable. Two critical hindrances in NIR-light-driven $CO_2RR$ are poor utilization of low-energy photons and low energy conversion efficiency. To advance the progress of NIR-light-driven $CO_2$ reduction, reasonable guidance should be developed, especially for the design of photocatalysts. Moreover, there are diverse possible products in $CO_2$ photoreduction, such as CO,[31,56] HCOOH,[18] $CH_4$,[24,30] $C_2H_4$,[49] $CH_3OH$,[72] *etc.* To trigger NIR-light-driven $CO_2$ reduction, the catalysts are required to efficiently absorb NIR light and generate free electrons for $CO_2RR$. However, the main product in reported NIR-light-driven $CO_2$ reduction systems is

Table 2 Reported NIR-light-driven $CO_2$ reduction systems and the corresponding products (the origin of products is verified by $^{13}C$-labelling experiments)

| Photocatalyst | Catalyst type | Light source | Photocatalytic system | $CO_2$RR performance ($\mu mol\ g^{-1}\ h^{-1}$) | Ref. |
|---|---|---|---|---|---|
| $V_o$-rich $WO_3$ | Intermediate-band photocatalyst | 40 W SiN lamp, $\lambda$: 0.8–17 μm | $CO_2$(g) + $H_2O$(g), solid–vapor mode | CO: 2.75 | 62 |
| $Cu_{2-x}S$/g-$C_3N_4$ | Intermediate-band photocatalyst | 300 W Xe lamp, $\lambda > 800$ nm | $CO_2$(g) + $H_2O$(g), solid–vapor mode | CO: 101.1, $CH_4$: 21.0 | 103 |
| HCNT-NA | Intermediate-band photocatalyst | 5 W white LED lamp, $\lambda$: 780–850 nm | ACN + TEOA + $CO_2$(g) + $CoCl_2$ + 2,2′-bipyridine, solid–liquid–gas mode | CO: 6.31 | 48 |
| $Cu_{2-x}S$/Ni–Al-LDH | Intermediate-band photocatalyst | 300 W Xe lamp, $\lambda > 800$ nm | $CO_2$(g) + $H_2O$(l), solid–liquid–gas mode | CO: 3.00, $CH_4$: 2.83 | 42 |
| $CuInS_2$ | Intermediate-band photocatalyst | 300 W Xe lamp, $\lambda > 800$ nm | $CO_2$(g) + $H_2O$(g), solid–vapor mode | CO: $<10.00$ | 63 |
| c-CSON | Intermediate-band photocatalyst | 71 mW $cm^{-2}$ Xe lamp, $\lambda > 800$ nm | $CO_2$(g) + $H_2O$(g), solid–vapor mode | CO: 21.95, $CH_4$: 4.11 | 50 |
| CuS | Metallic photocatalyst | 300 W Xe lamp, $\lambda > 800$ nm | $CO_2$(g) + $H_2O$(g), solid–vapor mode | CO: 14.5 | 57 |
| CoN | Metallic photocatalyst | 300 W Xe lamp, $\lambda > 800$ nm | $CO_2$(g) + $Na_2S$ (aq.), solid–liquid–gas mode | CO: 14.5 | 56 |
| $B_{13}P_2$ | Metallic photocatalyst | 300 W Xe lamp, $\lambda > 780$ nm | DMF + TEOA + $CO_2$(g) + $CoCl_2$ + 2,2′-bipyridine, solid–liquid–gas mode | CO: 0.13 | 104 |
| Ni-doped $CoS_2$ | Metallic photocatalyst | 300 W Xe lamp, $\lambda > 800$ nm | $CO_2$(g) + $H_2O$(g), solid–vapor mode | CO: 37.5, $CH_4$: 101.8 | 24 |
| $V_o$-rich $MoO_{2-x}$ | Metallic photocatalyst | 300 W Xe lamp, $\lambda > 700$ nm | $CO_2$(g) + $H_2O$(g), solid–vapor mode<br>Air + $H_2O$(g), solid–vapor mode | CO: 1.9, $CH_4$: 6.8<br>CO: 6.5, $CH_4$: 0.5 | 64 |
| Pt/Ni-MOF | Metallic photocatalyst + photothermal utilization | 940 nm LED light | $CO_2$(g) + $H_2$(g), solid–gas mode | CO: 606, $CH_4$: 135 | 29 |
| UiO-66/$Co_9S_8$ | Metallic photocatalyst + photothermal utilization | 300 W Xe lamp, $\lambda > 800$ nm | $CO_2$(g) + $H_2O$(g), solid–vapor mode | $CH_4$: 25.7 | 25 |
| HO-Ru/TiN | Metallic photocatalyst + photothermal utilization | 300 W Xe lamp, $\lambda > 800$ nm | $CO_2$(g) + $H_2O$(g), solid–vapor mode | CO: 2.76 | 55 |
| Bismuthene | Metallic photocatalyst + photothermal utilization | 300 W Xe lamp, $\lambda \geq 700$ nm | $CO_2$(g) + $H_2O$(g), solid–vapor mode | CO: 0.66, $CH_4$: 0.11 | 105 |
| C@$Fe_2C$/TiO | Metallic + heterojunction photocatalyst | 300 W Xe lamp, $\lambda > 700$ nm | $CO_2$(g) + $H_2O$(l) + TEOA, solid–liquid–gas mode | $CH_4$: 18.315 | 106 |
| $WS_2$/$Bi_2S_3$ | Heterojunction photocatalyst | 300 W Xe lamp, 0.45 mW $cm^{-2}$, $\lambda$: 800–1100 nm | $CO_2$(g) + $H_2O$(l), solid–liquid–gas mode | $CH_3OH$ + $C_2H_5OH$: 10.5 | 107 |
| 10% $Ag_2S$/$Sb_2S_3$ | Heterojunction photocatalyst | 300 W Xe lamp, NIR light | $CO_2$(g) + $H_2O$(g), solid–vapor mode | CO: 0.81, $CH_4$: 4.11 | 108 |
| $Bi_2O_{3-x}$ | SPR system | LED lamp, $\lambda$ = 940 nm | $CO_2$(g) + $H_2$(g), solid–gas mode | CO: 4.5 | 17 |
| $Ru_1$@H-$MoO_{3-x}$ | SPR system | 300 W Xe lamp, $\lambda > 700$ nm | $CO_2$(g) + $H_2O$(g), solid–vapor mode | $CH_4$: 9.75 | 109 |
| 10-BP/WO | SPR system | 300 W Xe lamp, $\lambda > 800$ nm | $CO_2$(g) + $H_2O$(l), solid–liquid–gas mode | CO: 4.17 | 110 |
| Au rod@CuPd | SPR system | Xe lamp, 400 mW $cm^{-2}$, $\lambda > 600$ nm | $CO_2$(g) + $H_2O$(g), solid–vapor mode | $CH_4$: 13.0 | 59 |
| $Au_n$/$Au_1$-CMS | SPR system | 300 W Xe lamp, 200 mW $cm^{-2}$, NIR light | $CO_2$(g) + $H_2O$(l), solid–liquid–gas mode | $CH_3COOH$: 8.2 | 58 |
| NiAl–Ru-LDH | Narrow-bandgap photocatalyst | 300 W Xe lamp (79 mW $cm^{-2}$), $\lambda$ = 1200 nm | $CO_2$(g) + $H_2O$(l) + TEOA + ACN, solid–liquid–gas mode | CO: 110.8 | 111 |
| PSCN | Narrow-bandgap photocatalyst | 300 W Xe lamp, $\lambda > 800$ nm | $CO_2$(g) + $H_2O$(g), solid–vapor mode | CO: 58.5 | 112 |
| TNP-MOF | Narrow-bandgap photocatalyst | 300 W Xe lamp, $\lambda > 730$ nm | ACN + TEOA + $CO_2$(g), solid–liquid–gas mode | HCOOH: 6630 | 18 |

CO, a kinetically favored product, because of the low photon energy of NIR light (Tables 2 and 3). It is challenging to convert $CO_2$ to hydrocarbon compounds or $C_{2+}$ products. To obtain multi-electron transfer products, the photocatalysts should generate a high concentration of electrons. Additionally, to selectively produce $C_1$ or $C_{2+}$ products, the catalytic sites ought to be precisely designed to ensure appropriate adsorption intensity towards intermediates (Fig. 9). Thus, developing catalysts with excellent NIR light absorption is the key to achieving highly efficient NIR-light-driven $CO_2$RR. Therefore, it is pivotal to explore innovative strategies and catalysts for NIR-light-driven $CO_2$ reduction. Several strategies have been explored to accomplish NIR-light-driven $CO_2$ reduction, including the energy band structure regulation strategy, the energy transfer strategy, and the photothermal strategy (Fig. 10). The energy band structure regulation strategy mainly focuses on band structure engineering to meet the requirements of efficient NIR light absorption and band edge position matching simultaneously. Typical examples include narrow-bandgap photocatalysts, intermediate-band photocatalysts, metallic photocatalysts, and heterojunction photocatalysts (Fig. 10A–D), which are able to directly utilize NIR light for $CO_2$ conversion due to their narrow or relay band structure features. The energy transfer strategy is an indirect method for NIR light utilization. For traditional semiconductors that can only harvest UV or visible light, it is a very attractive way to combine them with up-conversion nanoparticles (UCNPs) or plasmonic components (Fig. 10E and F). UCNPs are capable of transforming NIR light into UV or visible light, which can be harvested by most semiconductors. Plasmonic components can absorb NIR light through the SPR effect and subsequently transfer hot electrons and resonance energy to traditional semiconductors *via* direct electron transfer (DET) and plasmon-induced resonant energy transfer (PIRET). As a result, the UCNP and SPR material-based photocatalytic systems can utilize NIR light effectively. In addition, NIR light possesses a unique photothermal effect, which is conducive to accelerating the photocatalytic reaction. Therefore, creating a photothermal synergetic catalysis system is also a good strategy to utilize NIR light (Fig. 10G). In the following sections, we will discuss the fundamental principles and applications of these strategies for NIR-light-driven $CO_2$ reduction in detail.

# 4. Strategies for harvesting NIR photons for photocatalytic $CO_2$ reduction

## 4.1. Energy band structure regulation strategy

**4.1.1. Narrow-bandgap photocatalysts.** Narrow-bandgap semiconductors can achieve $PCO_2R$ by directly absorbing NIR light. However, designing narrow-bandgap photocatalysts with apposite electronic structures that meet the requirements for NIR-light-driven $CO_2$ reduction remains challenging. Narrowing the semiconductor's band gap allows it to absorb lower-energy photons, facilitating the transition of electrons from the VB to the CB and thereby extending the spectral absorption

Table 3 Reported NIR-light-driven $CO_2$ reduction systems and the corresponding products (the origin of products is verified by control experiments)

| Photocatalyst | Catalyst type | Light source | Photocatalytic system | $CO_2$RR performance ($\mu mol\ g^{-1}\ h^{-1}$) | Ref. |
|---|---|---|---|---|---|
| UCNPs/ZIS | Up-conversion photocatalyst | 300 W Xe lamp, $\lambda > 800$ nm | ACN + TEOA + $CO_2$(g), solid–liquid–gas mode | CO: 1.50, $CH_4$: 0.22 | 60 |
| CQDs/$Bi_2WO_6$ | Up-conversion photocatalyst | 500 W Xe lamp, $\lambda > 700$ nm | $CO_2$(g) + $H_2O$(g), solid–vapor mode | $CH_4$: 0.051 | 68 |
| $ZnO_{1-x}$/C | Up-conversion photocatalyst | 400 W Xe lamp, $\lambda$: 715–900 nm | $CO_2$(g) + $H_2O$(g), solid–vapor mode | CO: 15.98 | 61 |
| OD-ZnO/C | Up-conversion photocatalyst | 400 W Xe lamp, $\lambda$: 715–900 nm | $CO_2$(g) + $H_2O$(g), solid–vapor mode | CO: 31.2 | 113 |
| Few-layered BiOI | Intermediate-band photocatalyst | 300 W Xe lamp, $\lambda > 700$ nm | $CO_2$(g) + $H_2O$(g), solid–vapor mode | CO: 0.119, $CH_4$: 0.021 | 37 |
| $Bi_2WO_6$-OV | Intermediate-band photocatalyst | 500 W Xe lamp, $\lambda > 700$ nm | $CO_2$(g) + $H_2O$(g), solid–vapor mode | $CH_4$: 0.049 | 114 |
| V-$Bi_{19}Br_3S_{27}$ | Metallic photocatalyst | 300 W Xe lamp, $\lambda > 720$ nm | $CO_2$(g) + $H_2O$(l), solid–liquid–gas mode | $CH_3OH$: 0.4 | 72 |
| CuNi/C | SPR system | 300 W Xe lamp, $\lambda > 700$ nm | $H_2O$(l) + TEOA + $CO_2$(g), solid–liquid–gas mode | CO: 11.205, $CH_4$: 0.9 | 115 |
| 8Ni/$TiO_2$ | Photothermal utilization | 375 W IR lamp, 1230 mW $cm^{-2}$ | $CO_2$(g) + $H_2$(g), solid–gas mode | $CH_4$: 271.9 | 116 |

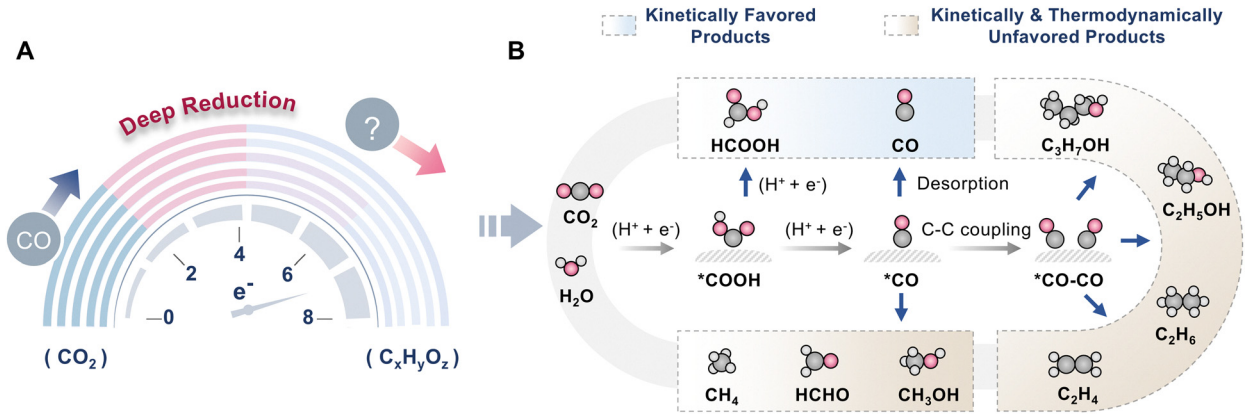


Fig. 9 (A) Deep photocatalytic $CO_2$ reduction. (B) Various pathways of photocatalytic $CO_2$ reduction.

range of the semiconductor. Concerning MOFs, narrowing their band gaps can often be achieved by adjusting their structural composition (such as extending the π-conjugated system), which enhances NIR light absorption efficiency and promotes $CO_2$RR. For example, Zeng and co-workers[18] synthesized a series of NIR-light-driven MOF photocatalysts by incorporating large π-conjugated porphyrin linkers and metal clusters ($Zr_6O_8$), namely, TBCP-MOF, TBML-MOF, TML-MOF, TM-MOF, and TNP-MOF, respectively (Fig. 11A–C). These five organic porphyrin linkers (TBCP, TBML, TML, TM, and TNP), with a key feature of macrocyclic π-conjugated electrons, have suitable lowest unoccupied molecular orbital (LUMO) energy levels that are thermodynamically feasible for catalyzing $CO_2$RR (Fig. 11D). The optical bandgaps of the MOFs gradually decrease with the enlargement of the π-conjugated systems. Specifically, among the MOF series, TNP-MOF, which has the most π-conjugated electrons (TNP, 58 π electrons), displayed the highest $CO_2$RR activity, converting $CO_2$ to formate with an unprecedentedly high activity of 6630 μmol $g^{-1}$ $h^{-1}$ under NIR illumination. The enlarged π-conjugated system in TNP-MOF, with its electron-rich feature from π-conjugated units, favors the charge transfer to the Zr clusters, thereby facilitating the electron–hole separation and migration, greatly improving the catalytic performance. As shown in Fig. 11E, activated by NIR light, TNP-MOF firstly generates excited electrons within the organic ligands, which are then transferred to the $Zr_6O_8$ clusters. Next, the NIR-induced electrons are transferred from the metal clusters to $CO_2$ molecules in contact with the substrates. Since the VBM of TNP-MOF is 0.55 V *vs.* NHE, which is below the water oxidation potential (0.82 V *vs.* NHE), adding a sacrificial agent is quite important for the overall NIR-light-driven $CO_2$RR system. Control experiments and $^{13}CO_2$-labelling experiments further confirm that the products originated from the NIR-light-driven $CO_2$ reduction. Moreover, AQE tests also demonstrate that TNP-MOF possesses excellent NIR-light-response performance for photochemical $CO_2$ reduction (Fig. 11F).

Recently, Zhao *et al.*[111] synthesized an organic–inorganic hybrid catalyst (NiAl–Ru-LDH) by introducing an anionic Ru coordination compound into the NiAl–$NO_3^-$-LDH interlayer, which successfully improved the spectral response of the LDH towards NIR light (Fig. 11G). The calculated total density of states (TDOS) and projected density of states (PDOS) indicate that introducing the Ru complex into the LDH interlayer significantly reduces its theoretical band gap from 2.41 to 0.74 eV (Fig. 11H). Consequently, this desirable band gap endows the NiAl–Ru-LDH catalyst with wide spectral response and impressive $PCO_2R$ performance. As shown in Fig. 11I, even at an irradiation wavelength of 1200 nm, the NiAl–Ru-LDH catalyst can still exhibit an activity of 1.108 μmol $h^{-1}$ (*ca.* 110.8 μmol $g^{-1}$ $h^{-1}$, given a specific photocatalyst amount of 10 mg).

Hence, constructing narrow-bandgap photocatalysts represents a promising strategy for NIR-light-driven $CO_2$RR.

**4.1.2. Intermediate-band photocatalysts.** To achieve both suitable CBM and VBM positions for $CO_2$RR and water oxidation, traditional semiconductors typically require relatively large band gaps. As a result, these materials are limited to absorbing visible or UV light, which restricts their ability to utilize the broader solar spectrum—particularly when attempting to extend absorption into the NIR region, which is crucial for maximizing solar energy conversion. To cope with this situation, an intermediate band (IB) was introduced within the forbidden band of semiconductors, which can function as a "springboard" for cascading electron transitions under NIR light excitation.[50,117] This strategy enables the material to effectively absorb NIR light and promote electron excitation through sequential transitions. In other words, with the existence of the IB, electron–hole pairs can be separated by a two-step electron transfer process: (1) VB to IB and (2) IB to CB, meeting the energy requirements for NIR-driven $CO_2$RR (Fig. 10B).

Defect engineering is a powerful method for introducing an IB into the forbidden band of semiconductors, as the structural defects will lead to defect states within the forbidden band, enabling the semiconductor to absorb lower-energy photons. A common example is the creation of oxygen vacancies ($V_o$), which can be introduced during material synthesis in a reducing atmosphere. For instance, Liang *et al.*[62] prepared defective $WO_3$ atomic layers by calcining the $WO_3$ precursor under a 20% $H_2$/Ar atmosphere (Fig. 12A). The density of states (DOS) and

 

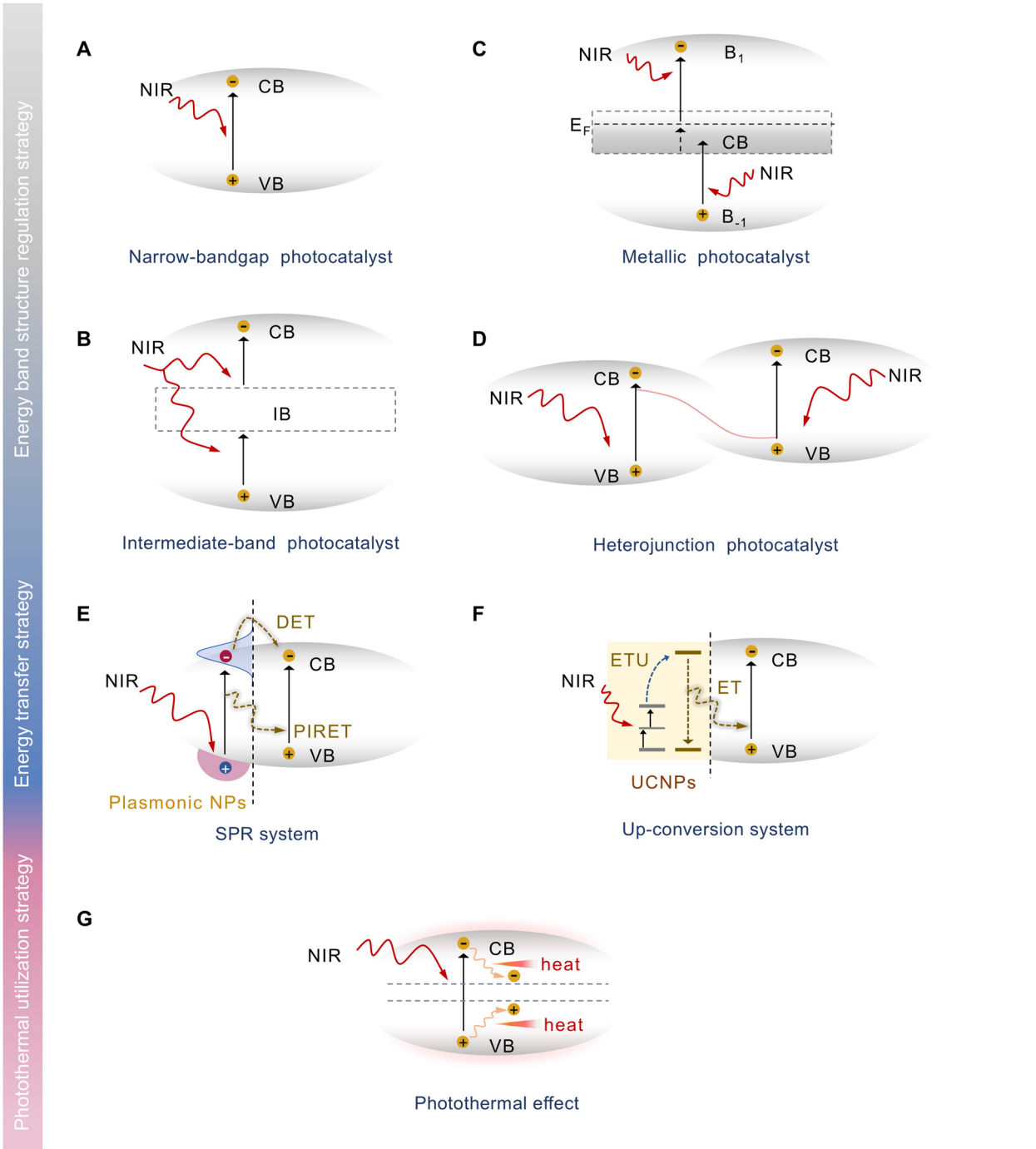


Fig. 10 Schematic illustration of different NIR photocatalysis mechanisms. Energy band structures of (A) narrow bandgap photocatalysts, (B) intermediate-band photocatalysts, (C) metallic photocatalysts, and (D) heterojunction photocatalysts. Illustrations of the (E) SPR system, (F) up-conversion system, and (G) photothermal synergetic system. CB = conduction band, VB = valence band, IB = intermediate band, $B_{-1}$ = the highest occupied band, $B_1$ = the lowest unoccupied band, DET = direct electron transfer, PIRET = plasmon induced resonant energy transfer, ET = energy transfer, and ETU = energy transfer up-conversion.

electronic structures reveal that a new energy level forms in the band gap of $WO_3$ when sufficient oxygen vacancies are introduced (Fig. 12B). The photoluminescence (PL) spectra of defective $WO_3$ atomic layers indicate that the IB is *ca.* 1.4 eV above the VB. As the defect concentration in the $WO_3$ atomic layers increases, the emission wavelength shifts to longer values, suggesting a narrower band gap between the IB and the VB. Consequently, $V_o$-rich $WO_3$ atomic layers exhibit the best NIR-light-driven catalytic activity in the conversion of $CO_2$ to CO, outperforming both the $V_o$-poor $WO_3$ and the original $WO_3$ atomic layers (Fig. 12C). Besides introducing oxygen vacancies, constructing metal-site defects is another feasible way to

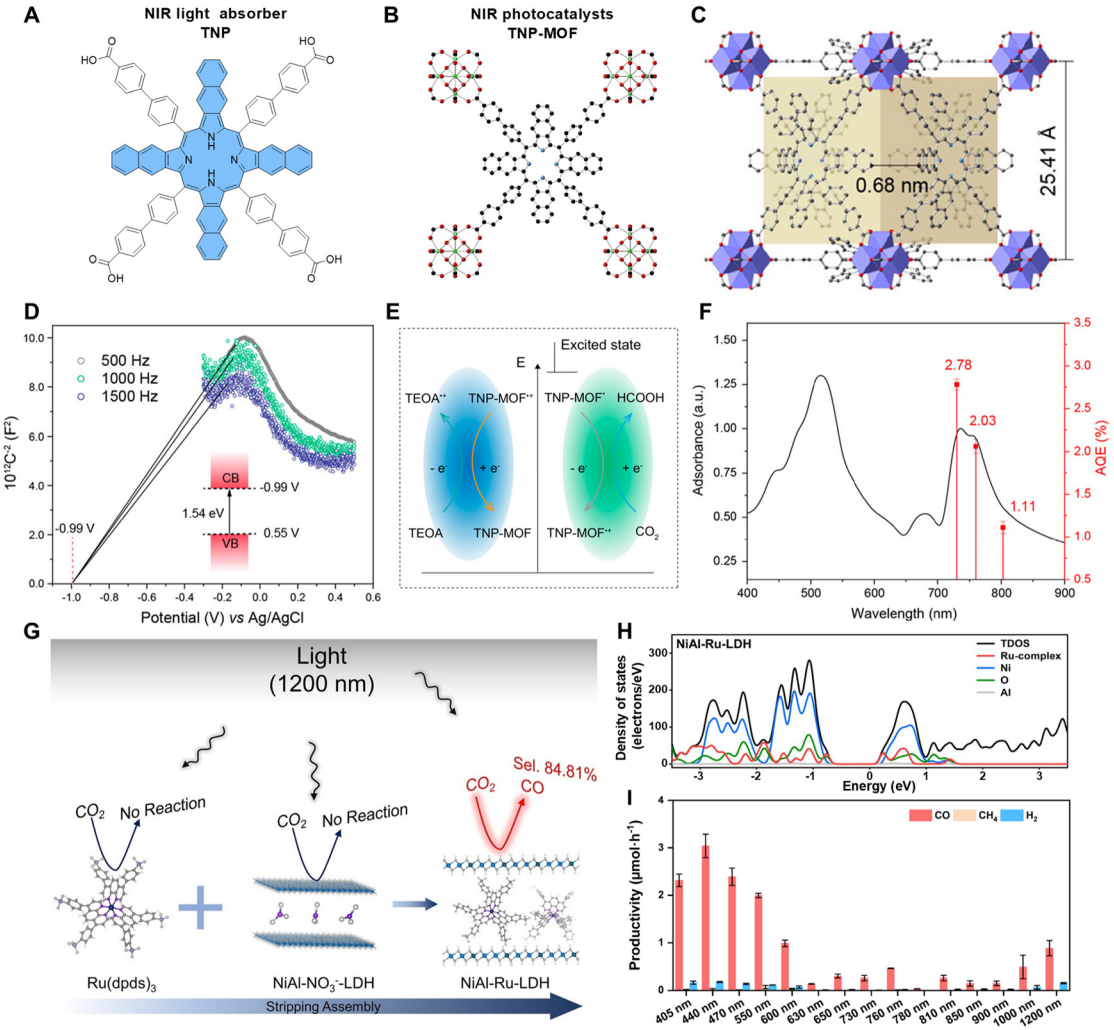


Fig. 11 Narrow-bandgap photocatalysts for harvesting NIR photons. (A) Molecular structure of the TNP linker. (B) and (C) Crystal structure of TNP-MOF. (D) Mott–Schottky curves and measured energy band structure of TNP-MOF. (E) NIR-light-driven $CO_2$ reduction mechanism for TNP-MOF. (F) AQE results for TNP-MOF measured under monochromatic light of different wavelengths. Reproduced with permission from ref. 18. Copyright 2022, American Chemical Society. (G) Schematic illustration of the NiAl–Ru-LDH preparation route. (H) TDOS and PDOS of NiAl–Ru-LDH. (I) The $CO_2$ photoreduction performance of NiAl–Ru-LDH at different irradiation wavelengths. Reproduced with permission from ref. 111. Copyright 2024, Wiley-VCH.

establish an IB.[42,103] For example, Zhang and co-workers fabricated a $Cu_{2-x}S$/g-$C_3N_4$ catalyst (CSCN) *via* the ethylene glycol-assisted solvothermal method.[103] The Cu vacancies generated by reducing ethylene glycol lead to the formation of an IB in $Cu_{2-x}S$, enhancing its absorption of NIR light (Fig. 12D). In the $Cu_{2-x}S$/g-$C_3N_4$ composite, the band gap of g-$C_3N_4$ is too large to utilize NIR light (Fig. 12E), which is why $Cu_{2-x}S$ acts as the NIR light absorber. The NIR-light-driven $CO_2$ reduction activity of the composite (CSCN) surpasses that of $Cu_{2-x}S$ alone (Fig. 12F). This increased activity stems from the enhanced $CO_2$ adsorption ability of g-$C_3N_4$.

Polymerized carbon nitrides (PCN) have drawn widespread interest in the area of photocatalysis because of their lamellar structures, chemical inertness, and affordable cost.[118,119] However, in terms of $PCO_2R$ efficiency, the original PCN is far from satisfactory. An attractive strategy is to modify their structures with specific organic groups to tune their band structures for photocatalysis. For example, the amino groups on the edge of pristine PCN have a propensity to adsorb the polar water molecules over nonpolar $CO_2$ molecules. This might potentially trigger the photocatalytic water-splitting process, thereby lowering the $CO_2$ photoreduction efficiency. Thus, Liu *et al.* introduced hydroxyethyl groups into porous PCN using *N*-acetylethanolamine (NA) as a modifier to activate its edge sites.[48] Compared to bulk PCN (BCN), the NA-modified PCN microtube (HCNT-NA) exhibits a slightly narrowed band gap while simultaneously forming an intermediate band (IB) (Fig. 12G). As a result, the spectral response range of HCNT-NA is expanded to the NIR region (Fig. 12H and I), thereby reinforcing its NIR photocatalytic activity.

Similarly, the empty d orbitals in certain transition-metal complexes, along with the intense interaction between the

 

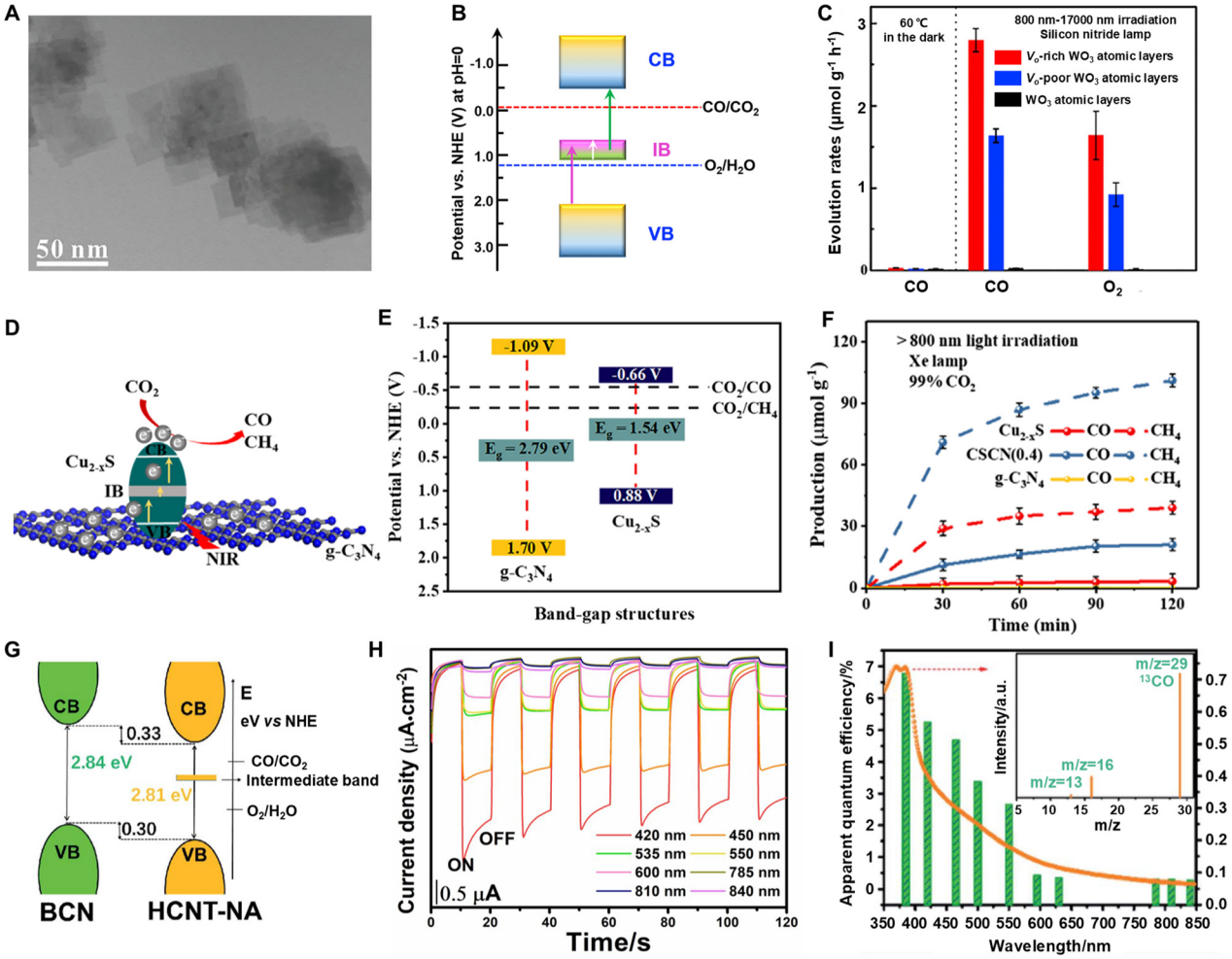


Fig. 12 Intermediate-band (IB) photocatalysts for $CO_2$RR under NIR illumination. (A) TEM image of the $V_o$-rich $WO_3$ atomic layers. (B) Measured electronic structures of $WO_3$ with oxygen defects. (C) NIR-light-driven $CO_2$ reduction activity under silicon nitride lamp irradiation (800 nm to 17 000 nm) for $WO_3$ atomic layers with different amounts of oxygen vacancies. Reproduced with permission from ref. 62. Copyright 2018, Elsevier. (D) Mechanism of PCO$_2$R over $Cu_{2-x}S/g\text{-}C_3N_4$ by NIR light irradiation. (E) Electronic structures of $Cu_{2-x}S$ and g-$C_3N_4$. (F) Catalytic performance of $Cu_{2-x}S/g\text{-}C_3N_4$ under NIR light irradiation. Reproduced with permission from ref. 103. Copyright 2020, Wiley-VCH. (G) Illustration of the band structures of bulk polymerized carbon nitride (BCN) and *N*-acetylethanolamine activated polymerized carbon nitride microtube (HCNT-NA). (H) Photocurrent response measurements over HCNT-NA. (I) AQE of HCNT-NA measured at different monochromatic wavelengths. The inset is the mass spectrum of a $^{13}$C-labelling experiment for $CO_2$ photoreduction over HCNT-NA. Reproduced with permission from ref. 48. Copyright 2020, Royal Society of Chemistry.

transition-metal ions and their associated ligands, have been reported to act as a natural intermediate band (Fig. 13A). These complexes absorb NIR light *via* d–d orbital transitions mediated by the vacant d orbitals. For instance, Li *et al.*[50] synthesized ultrathin $Cu_4(SO_4)(OH)_6$ nanosheets (CSON), which exhibited excellent NIR-photocatalytic performance, achieving the $CO_2$RR with evolution rates of 4.11 and 21.95 μmol $g^{-1}$ $h^{-1}$ for $CH_4$ and CO, respectively. The electronic structure and DOS of CSON reveal the presence of vacant d orbitals within the forbidden band (Fig. 13B and C). The Tauc curves and UV-vis-NIR diffuse reflectance spectra (DRS) demonstrate that both pristine CSON (p-CSON) and calcined CSON (c-CSON) samples display two narrow absorption bandgaps of 1.09 and 1.17 eV, which are attributed to electron transitions from the VB to vacant d orbitals and subsequent transfer to the CB (Fig. 13D–F). Moreover, the d–d electron transition mechanism has also been observed in other complexes similar to CSON, such as $Cu_2(NO_3)(OH)_3$, $Cu_3(PO_4)(OH)_3$, and $Cu_2(CO_3)(OH)_2$ nanosheets. Therefore, utilizing d-d orbital transitions in transition-metal complexes is a feasible strategy for achieving NIR-light-driven $CO_2$RR.

Hence, constructing an IB in photocatalysts—whether through defect engineering, structural modification, or d–d orbital transitions—presents a viable approach for fine-tuning their electronic structures to enable efficient NIR-light-driven $CO_2$ reduction.

**4.1.3. Metallic photocatalysts.** Although semiconductors with intermediate bands (IBs) have proven to be good choices for realizing NIR-light-driven $CO_2$ reduction, their development is hampered by the limited availability of suitable materials and the stringent processes required to introduce IBs. Besides, these photocatalysts often exhibit slow charge dynamics and

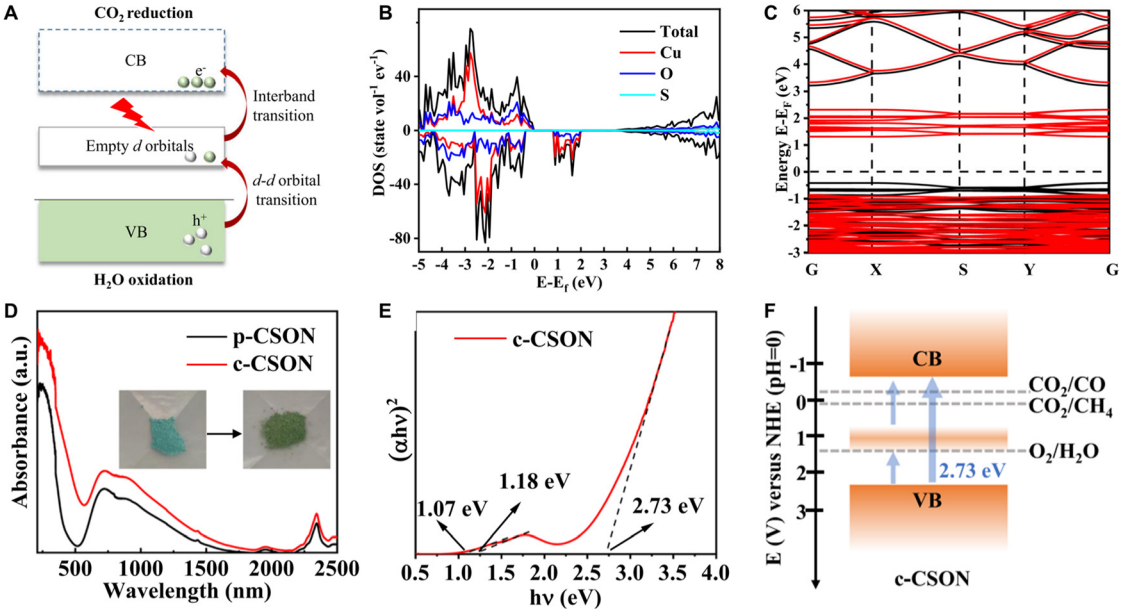


Fig. 13 Harvesting NIR photons *via* the d–d orbital transition mechanism. (A) Illustration of the d–d orbital transition mechanism. (B) Calculated DOS and (C) electronic structure of the CSON slab model. (D) UV-vis-NIR diffuse reflectance spectra of p-CSON and c-CSON. (E) Tauc plot of c-CSON. (F) NIR-light-driven $CO_2$ reduction mechanism over c-CSON. Reproduced with permission from ref. 50. Copyright 2023, Springer Nature.

low inherent carrier concentrations, which adversely affect the overall efficiency of $CO_2$ conversion. In contrast to traditional semiconductors, metallic catalysts, such as metal chalcogenides,[24,57] metal nitrides,[56] metal phosphides,[104] and some metal oxides,[64] stand out as viable alternatives for NIR-light-driven $CO_2$RR owing to their narrower or even zero bandgaps. With ideal band gap properties, metallic photocatalysts possess a broad spectrum response, ultra-high carrier density, and excellent electrical conductivity, which are the essential prerequisites for NIR light photocatalysis.[69,120] The energy band structures of metallic photocatalysts typically consist of the partially filled CB, the lowest unoccupied band ($B_1$), and the highest fully occupied band ($B_{-1}$) (Fig. 10C).[66] The carriers are produced through the intraband (*e.g.*, transitions from the lower position to the top in $B_{-1}$) and interband transitions (*e.g.*, transitions from $E_F$ to $B_1$, $E_F$ = Fermi energy level) in metallic photocatalysts (Fig. 14A). As a result of the existence of the partially occupied CB, metallic photocatalysts can simultaneously drive $CO_2$ reduction and $H_2O$ oxidation through either individual electron transition process or cascaded electron transition process. Based on this, the ultra-thin CuS conductor was first applied for NIR catalytic $CO_2$ reduction by Li *et al.*[57] The atomic layers of hexagonal lamellar metallic CuS were synthesized by a solvothermal method assisted by long-chain organic amines (Fig. 14B). As displayed in Fig. 14C, the resistivity of CuS nanosheets increases along with the increase of temperature, directly confirming their intrinsic metallic character. Valence-band X-ray photoelectron spectroscopy (VB-XPS), along with electronic structures and DOS obtained by DFT methods, further demonstrated that the $E_F$ crossed through the conduction band, corroborating the metallic characteristics of CuS nanosheets (Fig. 14D–F). This strong metallic property enhanced their catalytic performance, achieving an impressive CO production rate of 14.5 μmol $g^{-1}$ $h^{-1}$, while bulk CuS showed no NIR-photocatalytic activity because of its larger band gap.

Among the metallic photocatalysts, cobalt-based catalysts demonstrate remarkable NIR-light-driven $CO_2$ reduction performance. As depicted in Fig. 14G, Xie's group prepared metallic CoN atomic layers *via* nitriding CoO nanosheets, achieving conversion of $CO_2$ into CO with around 100% product selectivity under NIR light irradiation.[56] The femtosecond time-resolved transient absorption (*f*s-TA) spectra disclose interband recombination and intraband relaxation processes of charge carriers during NIR photocatalysis (Fig. 14H). Adding $Na_2S$ solution into the system significantly prolongs the lifetime of photo-generated electrons, increasing their intraband relaxation time by 9 times and interband recombination time by 1.6 times. Consequently, the CO release rate was dramatically enhanced to 14.5 μmol $g^{-1}$ $h^{-1}$ in the presence of $Na_2S$, a 16-fold increase compared to that without $Na_2S$ (Fig. 14I).

In light of their low carrier concentration, traditional catalysts find it challenging to deeply transform $CO_2$ into hydrocarbons *via* multiple proton–electron transfer processes under UV and visible light conditions, let alone under NIR light radiation. To achieve deep $CO_2$ reduction, the photocatalysts are required to generate a sufficient concentration of electrons and possess adequate adsorption capacity to form reaction intermediates. Here, metallic catalysts, with their near-zero bandgap, can generate a high density of charge carriers even under NIR light, making them advantageous for facilitating deep $CO_2$ reduction. Therefore, metallic photocatalysts show great potential for NIR-driven $CO_2$ conversion into hydrocarbons. In this context, Xu *et al.* designed metallic Ni-doped

 

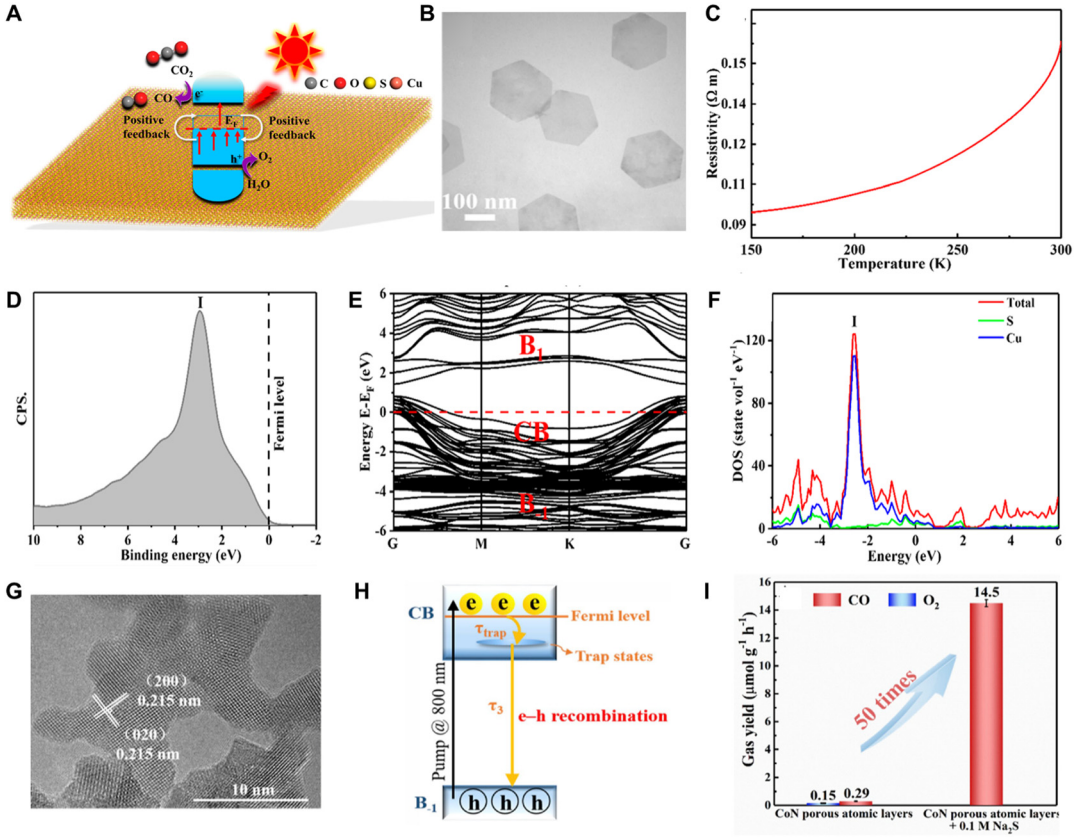


Fig. 14 Harvesting NIR photons *via* metallic photocatalysts. (A) Electron transition mechanisms in metallic CuS atomic layers under NIR light irradiation. (B) TEM image of CuS atomic layers. (C) Temperature dependence of resistivity and (D) VB-XPS spectrum of the ultrathin CuS conductor. (E) Calculated electronic band structure and (F) DOS of CuS nanosheets. Reproduced with permission from ref. 57. Copyright 2019, American Chemical Society. (G) HRTEM image of porous CoN atomic layers. (H) The electron transition mechanism within the CoN catalyst. (I) NIR-light-driven $CO_2$ reduction performance over porous CoN atomic layers. Reproduced with permission from ref. 56. Copyright 2019, Elsevier.

$CoS_2$ (Ni–$CoS_2$) nanosheets *via* a NaCl-mediated strategy and realized a remarkable $CH_4$ productivity of 101.8 μmol $g^{-1}$ $h^{-1}$ by NIR light excitation (Fig. 15A).[24] Both Arrhenius plots and PL spectra indicate that doping Ni atoms in $CoS_2$ nanosheets promotes carrier separation as well as reduces the activation energy required for $CO_2$ photocatalysis. Furthermore, DFT calculations reveal that Ni doping effectively reduces the generation energy of intermediates (*e.g.*, *CHO and *COOH), as well as the desorption energy of $CH_4$, thus leading to the high selectivity of $CH_4$ (90.6%) (Fig. 15B). To reinforce the $CO_2$ affinity of catalysts, Xu *et al.*[25] developed a UiO-66/$Co_9S_8$ composite photocatalyst, leveraging the $CO_2$ adsorption ability of UiO-66 and the metallic feature of $Co_9S_8$. The extended X-ray absorption fine structure (EXAFS) spectra reveal that two inequivalent Co sites (Co1 and Co2 site) present in $Co_9S_8$ and the adjacent Co1 sites have strong metal–metal interaction, which also induces the metallic property of $Co_9S_8$ (Fig. 15C and D). The electron-rich Co1 sites help stabilize the intermediates and reduce the reaction barriers for $CH_4$ production, leading to a high $CH_4$ selectivity of *ca.* 100%. Besides, finite element (FEM) simulations reveal that the local $CO_2$ concentration on $Co_9S_8$ is significantly increased (Fig. 15E), promoting the reaction kinetics of $CO_2$RR. The control experiments verified that the generation of $CH_4$ is attributed to the reduction of $CO_2$, rather than the carbon contamination in the reaction system. To achieve alcohol production through $CO_2$ photoreduction, Li *et al.*[72] reported the metallic $Bi_{19}Br_3S_{27}$ nanowires (V-$Bi_{19}Br_3S_{27}$) with abundant Br and S defects, as well as Bi-O bonds at the surface (Fig. 15F and G). The cooperative effect of both O doping and vacancies diminishes the energy barriers of the entire reaction and helps transform the conversion process of *CO to *CHO from being endothermic to exothermic. As a result, the V-$Bi_{19}Br_3S_{27}$ nanowires exhibit extraordinary activity for converting $CO_2$ into methanol ($CH_3OH$) without any sacrificial agent under NIR light excitation (Fig. 15H).

Moreover, metallic photocatalysts are more likely to achieve a reduction process under low $CO_2$ concentration atmospheres due to their ability to generate high carrier concentrations. Recently, Wu *et al.*[64] reported a metallic $MoO_2$ enriched with oxygen defects ($V_o$-rich $MoO_{2-x}$), which is not only suitable for $PCO_2R$ in the UV to NIR wavelength range but also achieves NIR-light-driven $CO_2$RR in ambient air. The existence of oxygen defects promotes the adsorption and activation of $CO_2$, and induces the generation of the Mo-C-O-Mo intermediate. This intermediate further enables the deep reduction of $CO_2$ to $CH_4$ by NIR irradiation in a pure $CO_2$ atmosphere (Fig. 15I).

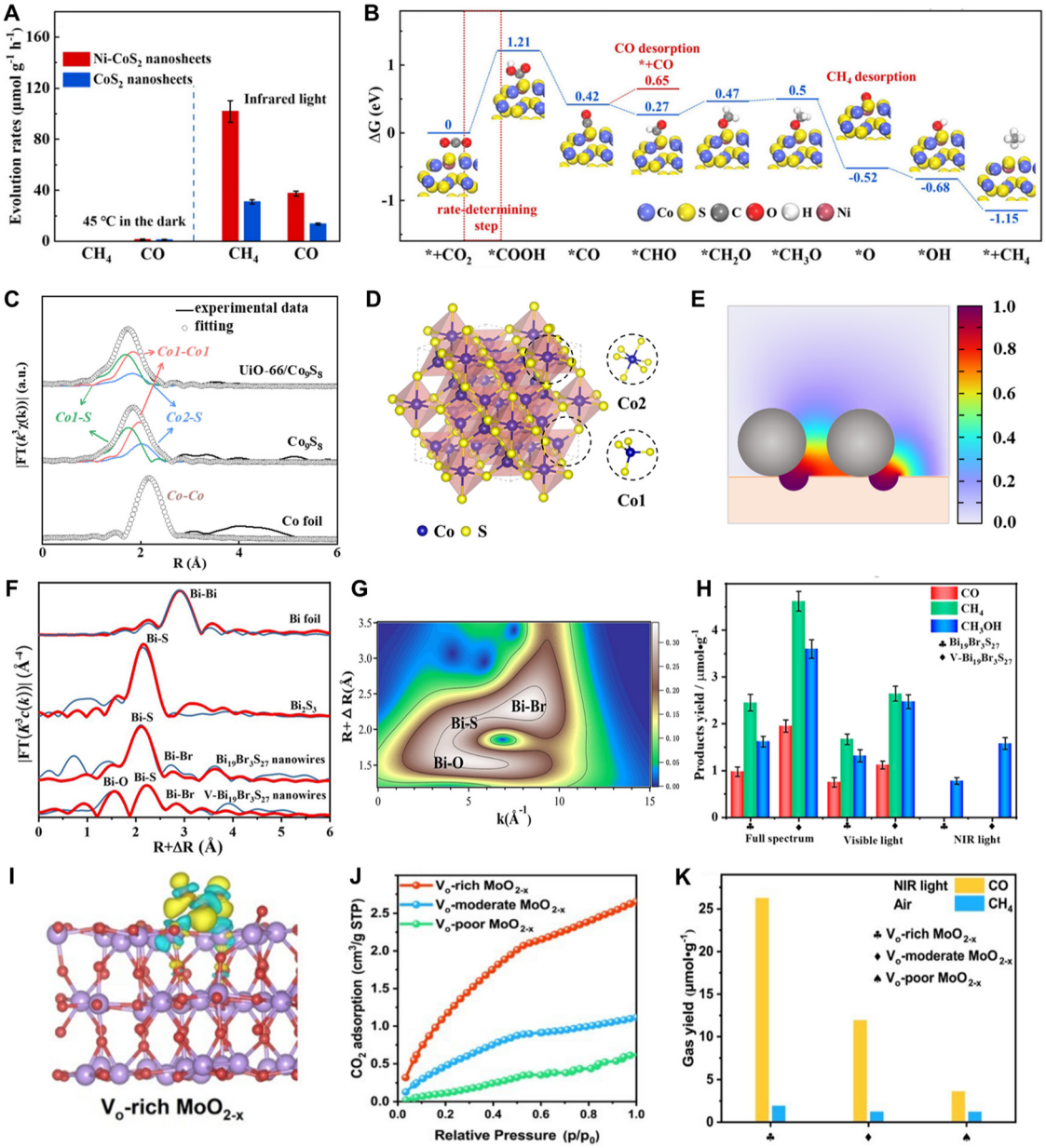


Fig. 15 Deep reduction of $CO_2$ into hydrocarbon compounds over metallic photocatalysts. (A) Formation rates of CO and $CH_4$ on Ni–$CoS_2$ nanosheets under NIR light excitation. (B) Gibbs energy changes during the NIR-light-driven $CO_2$RR over Ni–$CoS_2$ nanosheets. Reproduced with permission from ref. 24. Copyright 2021, Wiley-VCH. (C) Structural information derived from Co K-edge EXAFS spectra. (D) Crystal structure of $Co_9S_8$. (E) FEM simulation for $CO_2$ distribution around UiO-66/$Co_9S_8$. Reproduced with permission from ref. 25. Copyright 2024, Wiley-VCH. (F) Structural information derived from Bi K-edge EXAFS spectra and (G) corresponding wavelet transforms for $k^2$-weighted EXAFS curves for V-$Bi_{19}Br_3S_{27}$. (H) Photocatalytic $CH_3OH$ evolution over V-$Bi_{19}Br_3S_{27}$ nanowires. Reproduced with permission from ref. 72. Copyright 2021, American Chemical Society. (I) The charge density difference of $V_o$-rich $MoO_{2-x}$ with adsorption of $CO_2$. (J) $CO_2$ adsorption isotherms of $V_o$-poor, $V_o$-moderate, and $V_o$-rich $MoO_{2-x}$. (K) Yields of gas products from $CO_2$RR under NIR light. Reproduced with permission from ref. 64. Copyright 2022, Wiley-VCH.

Additionally, the enhanced $CO_2$ affinity contributes to highly selective photoconversion of $CO_2$ into CO under NIR light in air (Fig. 15J and K). In light of the foregoing analysis, metallic materials are regarded as promising candidates for NIR-light-driven $CO_2$ reduction.

**4.1.4. Heterojunction photocatalysts.** To date, few single-component photocatalysts have been reported to realize NIR-light-driven $CO_2$ reduction. This limitation arises from the severe carrier recombination and the intrinsic conflict between NIR light absorption and appropriate electronic structures of the photocatalysts. Constructing heterojunctions is a typical method to improve carrier separation efficiency, among which the Z-scheme heterojunction is a common composite structure.[27,121] For instance, Bai *et al.*[27] *in situ* grew a $Co_3O_4$/$CuO_x$ composite on copper foam (Fig. 16A), which could transform into a Z-scheme heterojunction catalyst ($Co_3O_4$/$Cu_2O$) under light irradiation. Photo-assisted Kelvin probe force microscopy (KPFM) results suggest that electrons transfer from

 

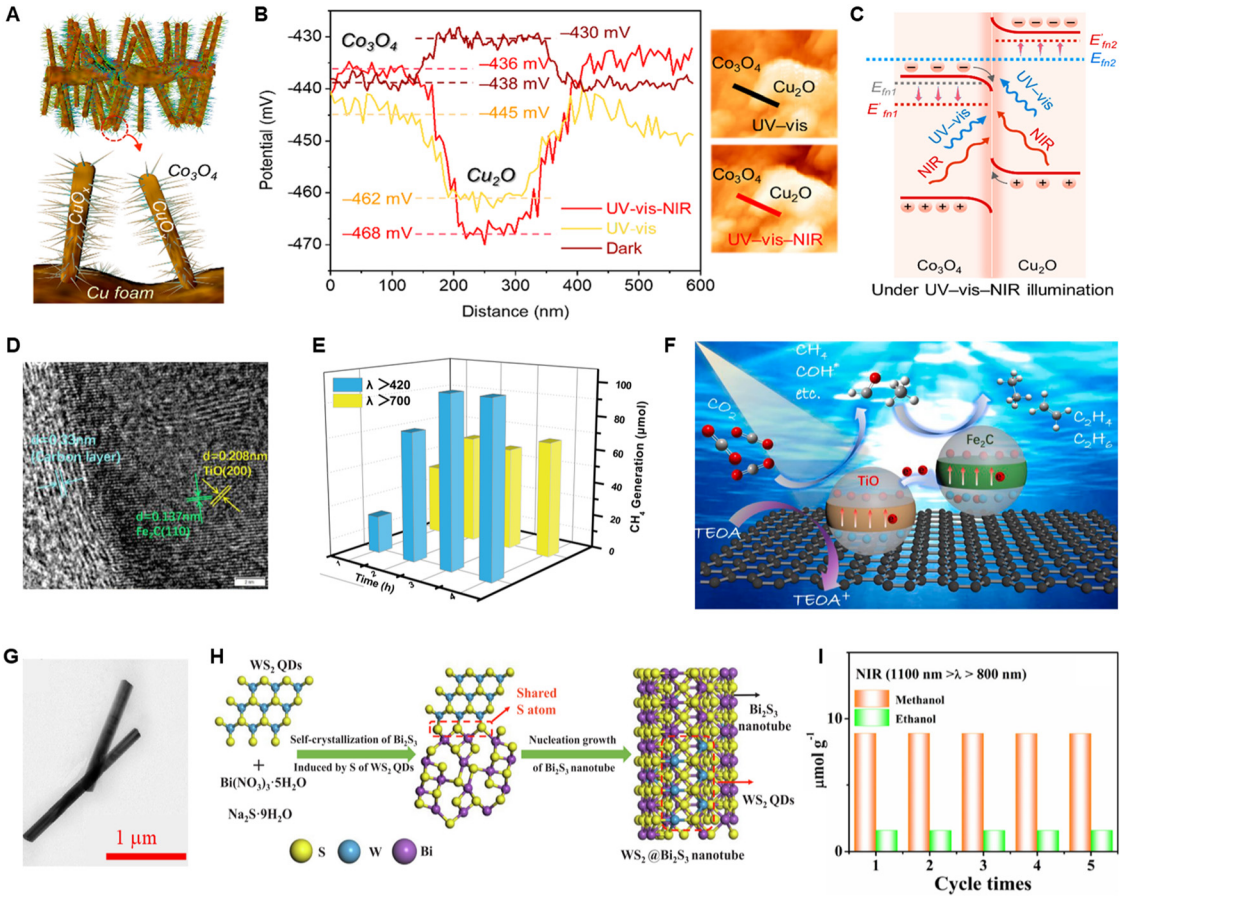


Fig. 16 Heterojunction structure promotes NIR-light-driven $CO_2$ reduction. (A) $CuO_x$/$Co_3O_4$ composites. (B) Surface potential profiles of the $Cu_2O$/$Co_3O_4$ heterojunction. (C) Electronic structure of $Cu_2O$/$Co_3O_4$. Reproduced with permission from ref. 27. Copyright 2023, American Chemical Society. (D) HRTEM image of C@$Fe_2C$/TiO. (E) The formation of $CH_4$ on C@$Fe_2C$/TiO by visible and NIR light irradiation. (F) Charge transfer pathway in C@$Fe_2C$/TiO. Reproduced with permission from ref. 106. Copyright 2021, Elsevier. (G) TEM characterization of $WS_2$@$Bi_2S_3$ nanotubes. (H) Synthetic procedure of the $WS_2$@$Bi_2S_3$ heterojunction. (I) Cycle measurement of $WS_2$@$Bi_2S_3$ under NIR irradiation. Reproduced with permission from ref. 107. Copyright 2019, Elsevier.

$Cu_2O$ to $Co_3O_4$ under dark conditions, while after applying light irradiation, electrons transfer from $Co_3O_4$ to $Cu_2O$ (Fig. 16B). This electron transfer mechanism confirms that a Z-scheme heterojunction between $Co_3O_4$ and $Cu_2O$ is formed (Fig. 16C). Intriguingly, introducing NIR light significantly enhances the surface potential difference between the two components, indicating improved charge transfer efficiency.

To deal with the problem of carrier recombination in metallic photocatalysts, Hao *et al.*[106] prepared a carbon-coated Z-scheme heterojunction catalyst (C@$Fe_2C$/TiO) using two metallic components, TiO and $Fe_2C$ (Fig. 16D). The Z-scheme heterojunction system significantly enhances the $PCO_2R$ activity of C@$Fe_2C$/TiO under NIR light illumination (Fig. 16E). As shown in Fig. 16F, the holes in the VB of $Fe_2C$ will recombine with the excited electrons in the CB of TiO, further enhancing carrier separation. Dai *et al.*[107] constructed a $WS_2$@$Bi_2S_3$ heterojunction catalyst by doping $WS_2$ quantum dots (QDs) into $Bi_2S_3$ nanotubes (Fig. 16G and H). The interface between $WS_2$ and $Bi_2S_3$ matches very perfectly, minimizing resistance and facilitating rapid electron transfer while ensuring efficient charge separation. Although $WS_2$ QDs ($E_g$ = 3.85 eV) cannot be activated upon NIR illumination, the NIR-light induced electrons in the CB of $Bi_2S_3$ will efficiently migrate to the CB of $WS_2$ QDs through the heterostructure. As a result, the $WS_2$@$Bi_2S_3$ heterojunction catalyst effectively converts $CO_2$ into $CH_3OH$ and $C_2H_5OH$ under NIR illumination (Fig. 16I). In a word, constructing heterostructures to accelerate electron–hole separation in NIR-light-driven $CO_2$ reduction is an effective method for improving catalytic performance.

### 4.2. Energy transfer strategy

**4.2.1. SPR system.** Surface plasmon resonance (SPR) occurs when incident light interacts with free electrons from a plasmonic material surface (usually metals). This resonance will result in the enhancement of the localized electromagnetic field.[122,123] Moreover, this resonance enables plasmonic nanostructures to strongly interact with electromagnetic radiation, and also leads to the localization of the subdiffraction-limit field and the enhancement of the high field. In photocatalysis, the SPR effect boosts light absorption and excitation efficiency

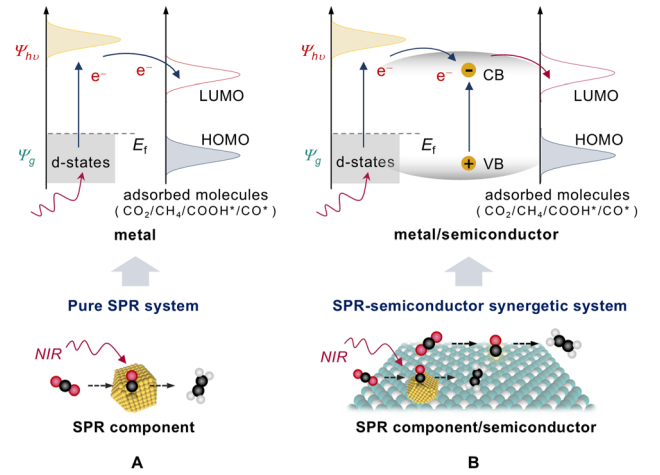


Fig. 17 Different SPR systems promote NIR-light-driven $CO_2$ reduction. (A) Pure SPR system. (B) SPR-semiconductor synergetic system.

in photocatalysts, thereby accelerating the reaction rate.[124] Therefore, precisely engineered plasmonic materials, designed with specific sizes, shapes, or structures, can resonate with incident light at targeted frequencies, making them highly effective for harvesting NIR light in $PCO_2R$.[17,80] Notably, many metals have proven to be effective $CO_2RR$ catalysts or cocatalysts at significantly low overpotentials, which may reduce the reaction energy barrier associated with $CO_2RR$. Furthermore, these nanostructures can steer the $CO_2$ photoreduction process *via* surface plasmon excitations. In this section, the SPR-mediated photocatalytic systems are divided into two categories: pure SPR system and SPR-semiconductor synergetic system (Fig. 17).

*4.2.1.1. Pure SPR system.* Unlike semiconductors, plasmonic materials, including precious metals (*e.g.*, Au, Pt, and Ag), non-precious metals (*e.g.*, Al and Cu), and specific carbon allotropes (*e.g.*, carbon nanotube), can induce SPR effects when irradiated by light.[59,125–128] These pure SPR systems can effectively utilize light energy to drive chemical reactions. By precisely modifying the size, morphology, and structure of nanomaterials, the SPR frequency of the plasmonic materials can be adjusted to match the frequency of low-energy photons, making these materials highly applicable for NIR-light-driven $CO_2RR$. For instance, Xiong's group[59] fabricated Au rod@CuPd composites through an alloying strategy, attaining the $CH_4$ release rate of 0.55 mmol $g^{-1}$ $h^{-1}$ and the hydrocarbon selectivity of 100% by full-spectrum light irradiation. Moreover, this SPR system can achieve $CO_2RR$ with an AQE of 0.38% at 800 nm, exhibiting impressive NIR photocatalytic activity (Fig. 18A–C). The *in situ* near ambient pressure X-ray photoelectron spectra (NAP-XPS) reveal that illumination increases the electron densities of Cu and Pd atoms in the Au rod@CuPd composite (Fig. 18D), indicating that the hot electrons induced by the SPR effect transfer from Au to the CuPd alloy and subsequently to the adsorbed $CO_2$. Meanwhile, the *quasi*-isolated trap states caused by the SPR effect prolong the lifespan of hot electrons, allowing their reactivation by additional low-energy photons (Fig. 18E). Moreover, the interaction between metal sites and $CO_2$ molecules is enhanced by the strong local electric fields created by the localized SPR effect, thereby boosting the migration of the electrons from the metal sites to $CO_2$ (Fig. 18F). To avoid the use of precious metals, Min *et al.* developed a CuNi/C bimetallic composite photocatalyst *via* pyrolysis of CuNi bimetallic MOF precursors (Fig. 18G and H).[115] As a consequence of the SPR effect generated by Cu and Ni, the CuNi/C catalyst responds to a broad spectral range from 200 to 2000 nm. Compared to monometallic Ni/C and Cu/C, the CuNi/C catalysts obtained by an alloying strategy also exhibit a higher CO production rate during the NIR-light-driven $CO_2$ reduction process (Fig. 18I).

*4.2.1.2. SPR-semiconductor synergetic system.* Integrating SPR components with traditional semiconductor photocatalysts is an innovative tactic for constructing efficient NIR-light-driven $CO_2$ reduction systems. In these SPR-semiconductor synergetic systems, the plasmonic component can efficiently harvest NIR photons and transfer hot electrons and resonance energy to the semiconductor *via* the SPR effect. Simultaneously, the semiconductor offers various active sites for $CO_2RR$ that can potentially be used to tune its photocatalytic activity and product selectivity. In addition, the metal/semiconductor contact could form a Schottky barrier, which improves photocatalytic efficiency by trapping and prolonging the lifespan of electrons and holes. Meanwhile, by adjusting the size and shape of SPR components, the SPR effect can be reinforced and the resonance frequency can be changed, leading to a wider light response suitable for the NIR photocatalytic system.[129–132] Therefore, integrating SPR materials into a semiconductor is a promising way to synthesize NIR-light responsive catalysts.

Constructing a SPR-semiconductor composite system enables the spectral response range to be expanded to the long-wavelength region; nevertheless, the supply of active hydrogen (*H) species and the efficiency of hot electron transfer in this system are still insufficient for effective $CO_2$ photoreduction. To address this, Xiao *et al.*[109] fabricated hydrogenated $MoO_{3-x}$ nanosheets with Ru single atom substitution ($Ru_1$@H-$MoO_{3-x}$), achieving an efficient transformation of $CO_2$ into $CH_4$ with a production rate of 9.75 μmol $g^{-1}$ $h^{-1}$ and a high selectivity of *ca.* 96% by NIR light irradiation (Fig. 19A). The Ru substitution and oxygen vacancy engineering induce the generation of the doped/defect energy band, which narrows the bandgap of the catalyst for enhancing NIR photon harvest. The fitting results of fs-TA kinetics curves indicate that the states of excited electrons within $Ru_1$@H-$MoO_{3-x}$ may undergo three relaxation processes (Fig. 19B): (i) from the excited state to the exciton state ($\tau_1$), (ii) from the exciton state to the defect trap state ($\tau_2$), and (iii) from the defect trap state to the ground state ($\tau_3$), where $\tau$ represents the consumed time for each transition process. As shown in Fig. 19B, $Ru_1$@H-$MoO_{3-x}$ possesses a shorter $\tau_1$ (0.50 ps) than that of H-$MoO_{3-x}$ (2.95 ps), suggesting a faster transition from excited states to exciton states. Besides, the $\tau_2$ (7.74 ps) and $\tau_3$ (167.46 ps) of $Ru_1$@H-$MoO_{3-x}$ are significantly higher than those of H-$MoO_{3-x}$ ($\tau_2$: 3.06 ps, $\tau_3$: 135.69 ps), verifying the longer carrier lifetime and higher charge separation efficiency. The surface photovoltage (SPV) analysis reveals that

 

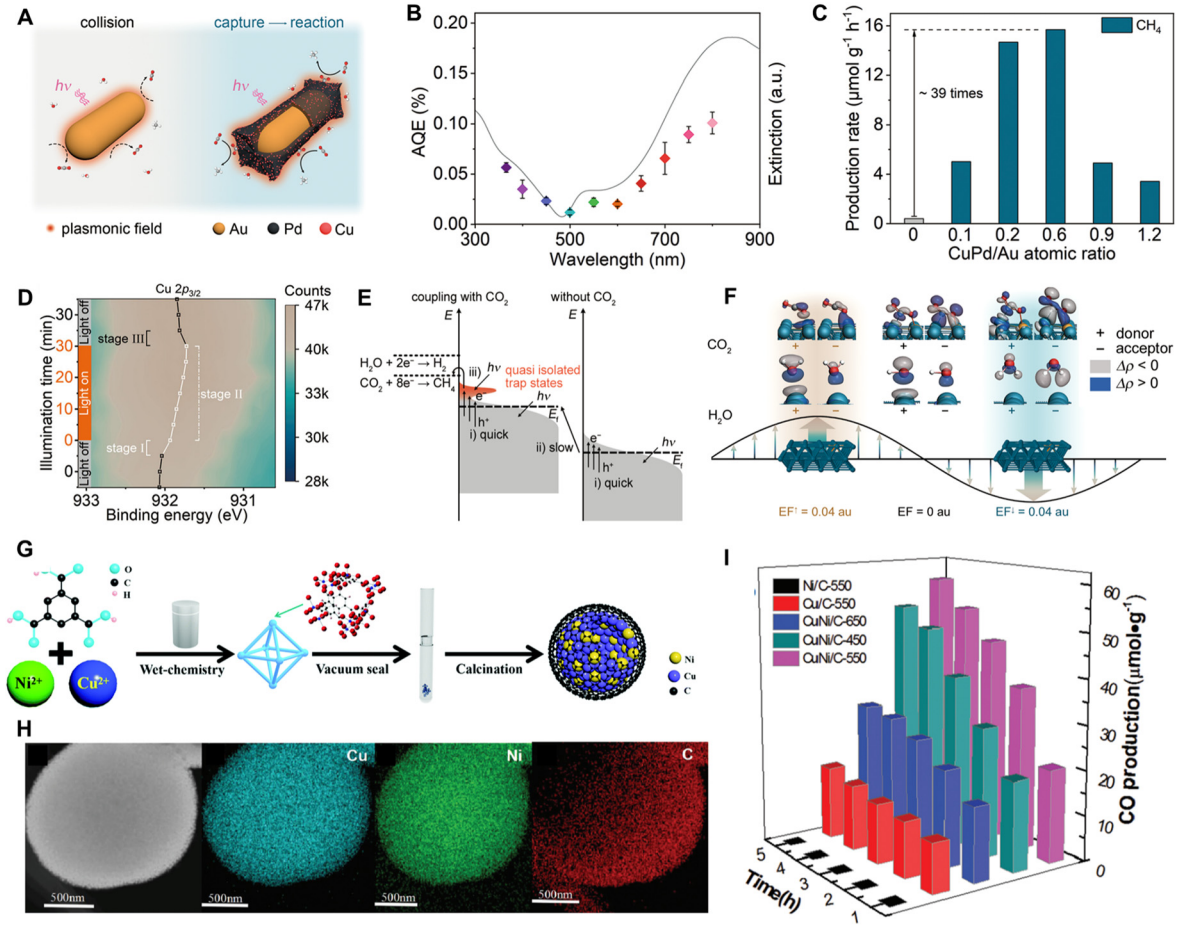


Fig. 18 Pure SPR system promotes NIR-light-driven $CO_2$ reduction. (A) The diagram of the $CO_2$ capture on the CuPd co-catalyst. (B) AQY of the Au rod@CuPd catalyst, measured under the illumination of monochromatic light of different wavelength. (C) $CH_4$ production over Au rod@CuPd with various CuPd/Au atomic ratios. (D) *In situ* NAP-XPS contour plot of Cu $2p^{3/2}$ over Au rod@CuPd. (E) Illustration of the SPR-mediated energy transfer mechanism during the $PCO_2R$ process. (F) Natural orbitals for chemical valence (NOCV) relate to the key deformation densities of $CO_2$ and $H_2O$ on the CuPd(100) plane. Reproduced with permission from ref. 59. Copyright 2023, Springer Nature. (G) Synthetic procedures of CuNi/C catalysts. (H) Elemental mapping images of CuNi/C catalysts. (I) $PCO_2R$ performance of CuNi-T/C catalysts ($T$ represents the calcination temperature, $T$ = 450, 550, and 650 °C) under NIR irradiation ($\lambda > 700$ nm). Reproduced with permission from ref. 115. Copyright 2020, Royal Society of Chemistry.

$Ru_1$@H-$MoO_{3-x}$ exhibits a larger SPV signal change (8 mV) than that of H-$MoO_{3-x}$ (6.5 mV), demonstrating a higher photogenerated electron concentration on the $Ru_1$@H-$MoO_{3-x}$ surface (Fig. 19C). Furthermore, theoretical calculations indicate that the doped Ru single atom can lower the energy barrier for *H generation and facilitate *H migration. With the synergy of Ru single atoms and oxygen vacancies, $Ru_1$@H-$MoO_{3-x}$ achieves the outstanding activation of $CO_2$ and $H_2O$, which ultimately contributes to its high selectivity towards $CH_4$.

The NIR-light-driven transformation of $CO_2$ into $C_{2+}$ products remains a challenge, primarily due to the low activation efficiency of $CO_2$, the low C–C coupling probability of $CO_2RR$ intermediates, and insufficient carrier utilization.[49,52,106,133] To accomplish this goal, Wu *et al.* developed a cross-scale heterojunction catalyst (denoted as $Au_n/Au_1$-CMS) by implanting Au nanoparticles ($Au_n$) and single atoms ($Au_1$) into unsaturated Mo atoms of edge-rich $MoS_2$ (CMS) (Fig. 19D).[58] Under NIR light irradiation, $Au_n/Au_1$-CMS presents high selectivity (95.1%) and activity (8.2 μmol $g^{-1}$ $h^{-1}$) for the photoreduction of $CO_2$ into acetate (Fig. 19E). The impressive NIR photocatalytic performance results from the SPR effect of Au nanoparticles. Additionally, the measured energy band structure of the $Au_n/Au_1$-CMS catalyst displays that the plasmonic Au metal, CMS semiconductor, and Au single atom form a SPR-semiconductor system, where hot electrons can transfer from Au nanoparticles to $Au_1$ through the CB of CMS, which remarkably inhibits the recombination of carriers (Fig. 19F). Hence, the SPR-semiconductor synergetic system exhibits huge potential in harvesting NIR photons for $CO_2RR$.

In brief, plasmonic materials are capable of efficiently harvesting NIR photons *via* the SPR effect, enabling the constructed photocatalysts to realize NIR-light-driven $CO_2$ reduction. Unfortunately, current plasmonic components are mainly based on noble metal nanoparticles, which are costly and obstructive to the development of SPR-photocatalytic systems. Besides, the carrier recombination is severe in the SPR-based $CO_2$ photoreduction system, which has an adverse impact on improving the efficiency of NIR-light-driven $CO_2RR$. Thus, novel and affordable

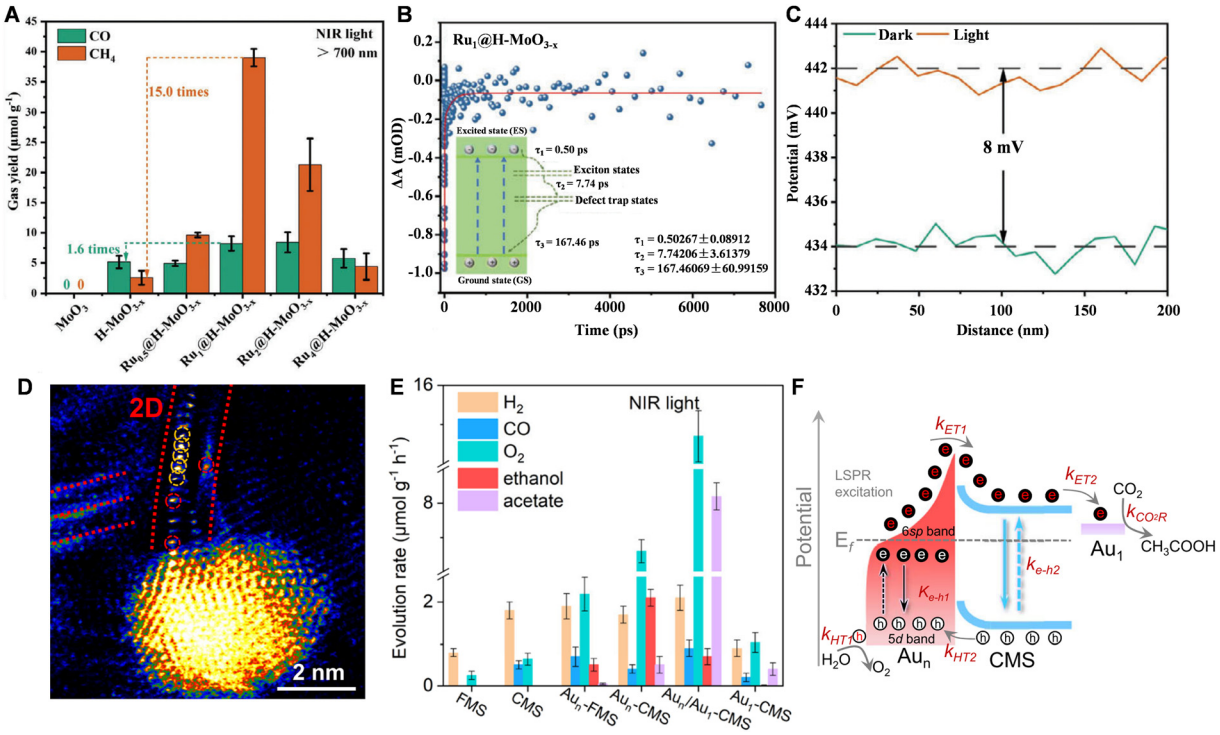


Fig. 19 SPR-semiconductor synergetic system promotes NIR-light-driven $CO_2$ reduction. (A) $PCO_2R$ performance over $MoO_3$ and $Ru_x$@H-$MoO_{3-x}$ ($x$ = 0, 0.5, 1, 2, 4) catalysts under NIR irradiation. (B) Transient absorption kinetics curves of $Ru_1$@H-$MoO_{3-x}$. (C) Surface photovoltage measurement of $Ru_1$@H-$MoO_{3-x}$. Reproduced with permission from ref. 109. Copyright 2024, Wiley-VCH. (D) The color-coded channel map of filtered atomic-resolution HAADF-STEM image for $Au_n/Au_1$-CMS catalysts. (E) NIR-light-driven $CO_2$ reduction performance over $Au_n/Au_1$-CMS and the control catalysts. (F) Electronic structure of $Au_n/Au_1$-CMS and the possible $PCO_2R$ mechanism. Reproduced with permission from ref. 58. Copyright 2024, Springer Nature.

plasmonic components and advanced SPR-semiconductor composite systems should be explored to reinforce SPR-promoted NIR-light-driven $CO_2RR$.

**4.2.2. Up-conversion system.** Up-conversion nanoparticles (UCNPs) can transform low-energy photons into high-energy photons, which can be further utilized by a wide range of semiconductors and SPR materials. This indirect approach enables NIR-light-driven $CO_2RR$ by integrating traditional photocatalysts with UCNPs. The process of up-conversion luminescence is attributed to the anti-Stokes effect, wherein UCNPs can continuously harness multiple low-energy photons, undergo non-radiative relaxation to reach an excited state, and then emit high-energy photons upon transitioning back to the ground state.[134–136] The up-conversion process can be achieved through five typical mechanisms, which include excited state absorption (ESA), energy transfer up-conversion (ETU), cooperative sensitization up-conversion (CSU), cross relaxation (CR), and photon avalanche (PA).[137,138] Currently, lanthanide-doped materials (Ln-doped materials) and carbon quantum dots (CQDs) are the most popular UCNPs utilized in NIR-light-driven $CO_2RR$.

Among Ln-doped materials, $Ln^{3+}$-doped materials exhibit efficient up-conversion performance due to their extremely long-lived intermediate energy states. For instance, UCNPs are typically formed by doping $Ln^{3+}$ ions into an appropriate host matrix, such as fluorides or oxides. Fluorides, particularly $NaYF_4$, are the common matrices due to their low phonon energy, high structural stability, and low non-irradiative energy losses. Moreover, by varying the type and concentration of the doped $Ln^{3+}$ ions, the wavelengths and intensities of the luminescence peaks of UCNPs can be fine-tuned to align with photocatalysts possessing different bandgaps. For instance, Yu *et al.* integrated UCNPs ($NaYF_4$: Yb, Tm) with $ZnIn_2S_4$ nanorods (ZIS), achieving $CO_2$ photoreduction into CO and $CH_4$ through NIR light activation (Fig. 20A and B).[60] As shown in Fig. 20C, ZIS displayed a spectral response in the region from 325 to 600 nm, while UCNPs emitted several peaks in the same range. Therefore, the up-conversion emission spectrum of UCNPs aligns well with the DRS spectrum of $ZnIn_2S_4$, indicating that the photons emitted by UCNPs are well-suited for exciting ZIS. However, since the VBM of ZIS was not sufficiently positive to drive water oxidation, a sacrificial agent (TEOA) was introduced to consume the holes and promote charge carrier separation, enhancing the overall photocatalytic performance.

While Ln-doped up-conversion materials show promise in utilizing NIR light, their low quantum efficiency (*ca.* 1–10%) and strong dependence on specific excitation wavelengths limit their practical applications.[138,139] Recently, carbon quantum dots (CQDs) have garnered wide attention in photocatalysis because of their impressive up-conversion capabilities and conductivity.[140] The conjugated π-electron transitions in CQDs enable increased spectral responsiveness to NIR light, effectively

 

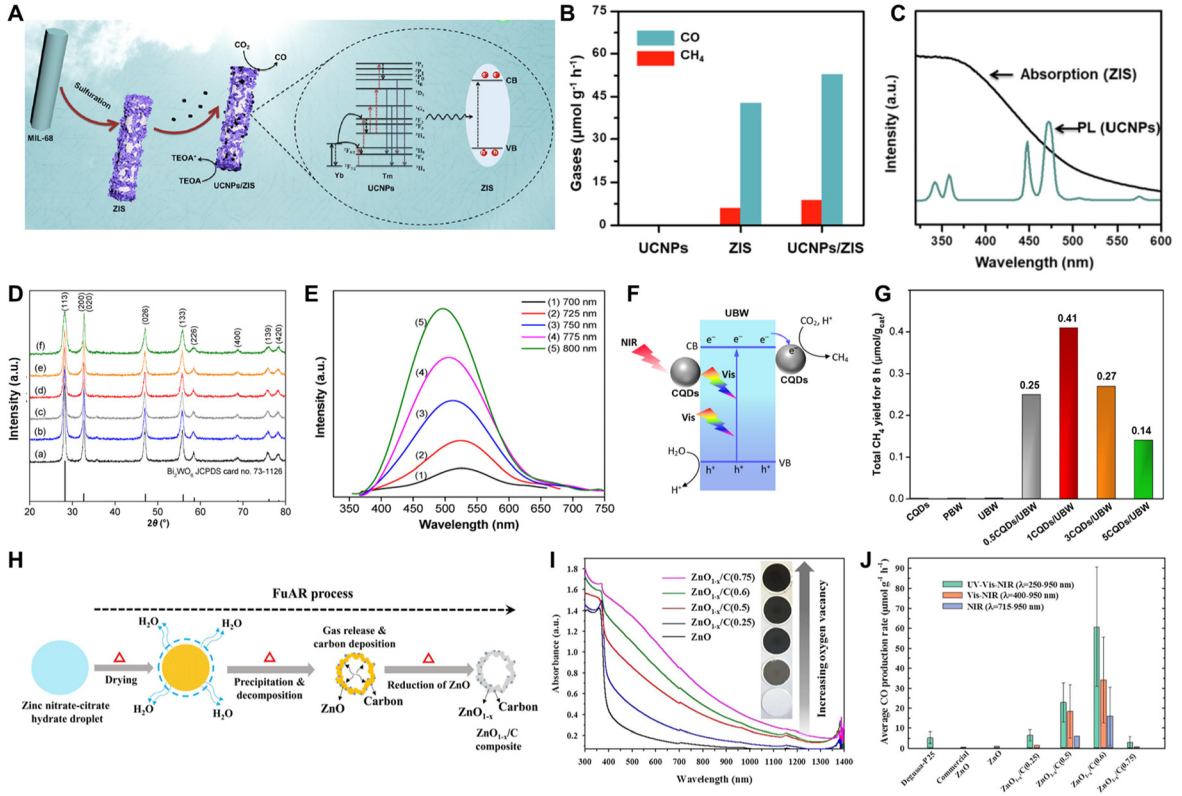


Fig. 20 Up-conversion systems promote NIR-light-driven $CO_2$ reduction. (A) Schematic diagram of the up-conversion mechanism and the $CO_2$ reduction process on UCNPs/ZIS. (B) The activity of UCNPs/ZIS. (C) PL spectrum of UCNPs overlaps with the DRS spectra of ZIS. Reproduced with permission from ref. 60. Copyright 2022, Elsevier. (D) XRD spectra. (E) Up-conversion PL spectra for CQDs. (F) $PCO_2R$ mechanism on CQDs/UBW catalysts. (G) The yield of $CH_4$ during $CO_2$ reduction by NIR light irradiation over the sample catalysts. Reproduced with permission from ref. 68. Copyright 2016, Springer Nature. (H) The diagram of the synthetic procedure of the $ZnO_{1-x}$/C composite catalyst. (I) UV-vis-NIR DRS spectra. (J) The CO evolution rate (5 h) on $ZnO_{1-x}$/C samples. Reproduced with permission from ref. 61. Copyright 2018, Elsevier.

overcoming the limitations associated with Ln-doped materials that require specific excitation wavelengths. For instance, Kong *et al.* decorated ultrathin $Bi_2WO_6$ nanosheets with CQDs, which enhanced the $CO_2$ reduction activity by broadening the spectral response range and enhancing the charge separation (Fig. 20D and E).[68] Under NIR light irradiation, the $Bi_2WO_6$ nanosheets, with the assistance of CQDs, achieved a $CH_4$ yield from 1 wt%-CQDs/$Bi_2WO_6$ that was 10.5-fold higher than that of original $Bi_2WO_6$ (Fig. 20F and G). Besides, CQDs/$Bi_2WO_6$ composites exhibited a larger transient photocurrent density and lower charge transfer resistance compared to pure $Bi_2WO_6$, possibly attributed to the exceptional electron conductivity of CQDs. In another case, Lin and co-workers synthesized a composite hollow sphere of $ZnO_{1-x}$/carbon dots ($ZnO_{1-x}$/C) for $CO_2$ photoreduction in the entire UV-vis-NIR spectral range (Fig. 20H–J).[61] Under NIR illumination alone, $ZnO_{1-x}$/C could also demonstrate a high $CO_2RR$ activity, achieving a CO formation rate of 15.98 μmol $g^{-1}$ $h^{-1}$. This performance can be attributed to the strong up-conversion photoluminescence emission capability of CQDs. Notably, no sacrificial agents were used in the CQDs/$Bi_2WO_6$ and $ZnO_{1-x}$/C systems mentioned above. The only reactants were $CO_2$ and water vapor (or humid $CO_2$ gas), rendering the photocatalytic system straightforward and environmentally friendly.

Consequently, up-conversion materials can be considered as a good medium for transforming long-wavelength light into short-wavelength light. By modifying the structures of these up-conversion materials, the energy of emission photons can be tailored to activate the catalysts with various bandgaps, thereby increasing the NIR-light responsiveness of the catalysts.

### 4.3. Photothermal utilization strategy

Compared with UV and visible light, NIR light exhibits a unique photothermal effect, and utilizing this effect is beneficial for promoting $CO_2$ reduction. Both the photochemical process and the thermochemical process caused by the NIR light are conducive to accelerating $CO_2RR$. The photochemical process can lower the activation barriers of $CO_2$ and the intermediates by increasing the acidity or alkalinity of the catalyst surface (carrier accumulation or depletion). In contrast, the thermochemical process promotes the overall reaction by elevating the temperature at active sites, leading to an increase of $k_BT$ ($k_B$ represents the Boltzmann constant, $T$ represents the reaction temperature), which is related to the kinetic energy of reaction molecules (Fig. 21).[141–144]

Hence, maximizing the photothermal effect of NIR light is crucial for improving $CO_2$ photoreduction. Below are the key advantages of photothermal utilization for $CO_2$ reduction.

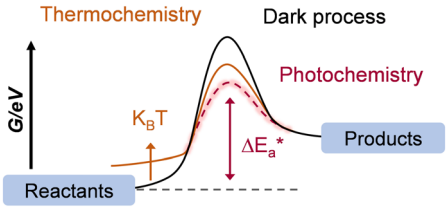


Fig. 21 Photothermal strategy for promoting NIR-light driven $CO_2$ conversion. Photochemistry contributes to reducing the reaction energy barrier, while thermochemistry helps the reactants overcome the barrier by elevating the temperature.

**Accelerating carrier migration.** In the solar-induced photothermal process, the extra heat induced by the photothermal effect could elevate the energy levels of charge carriers and accelerate their transport behavior.[145] For example, Yu *et al.*[146] synthesized $TiO_2$ with abundant oxygen vacancies *via* a solvothermal method, introducing defects that generated deep energy levels within the bandgap. Subsequently, post-solution plasma processing was used to dope hydrogen into the oxygen-vacancy-rich $TiO_2$, creating new shallow energy levels. These shallow energy levels were significantly closer to the CB of $TiO_2$ than those associated with oxygen vacancies (Fig. 22A and B). As a result, the modified $TiO_2$, enriched with mid-gap states, exhibited broad NIR absorption. During photothermal catalysis,

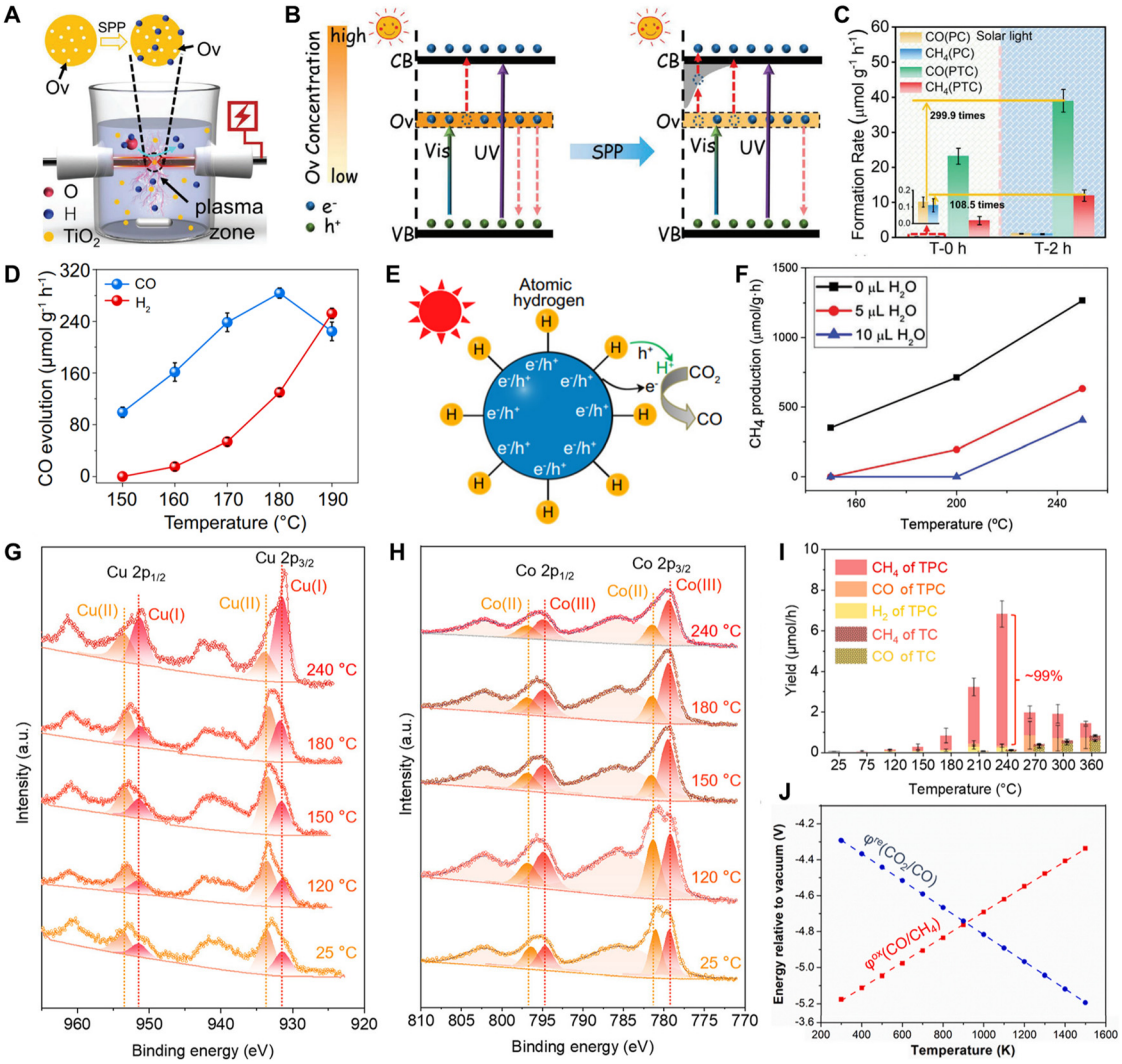


Fig. 22 The main potential advantages of the photothermal effect in $CO_2$ reduction. (A) The diagram of the solution plasma processing (SPP) method. (B) Carrier transfer process promoted by the photothermal effect in $O_V$-$TiO_2$ and SPP-treated $TiO_2$. (C) The photothermal catalytic performance (PTC) of $O_V$-$TiO_2$ (T-0 h) and SPP-treated $TiO_2$ (T-2 h). Reproduced with permission from ref. 146. Copyright 2020, Wiley-VCH. (D) Temperature-dependent CO and $H_2$ evolution rates over the Bi–$H_x$ catalyst. (E) Photothermal effect facilitating proton/electron transfer over the Bi–$H_x$ catalyst. Reproduced with permission from ref. 148. Copyright 2021, Springer Nature. (F) Influence of $H_2O$ on thermo-photo catalytic $H_2$-assisted $CO_2$ reduction over a $Cu_2O$/graphene catalyst. Reproduced with permission from ref. 149. Copyright 2017, Royal Society of Chemistry. Temperature-dependent quasi *in situ* XPS spectra of the (G) Cu 2p core level and (H) Co 2p core level for $Co_3O_4$/$CuO_x$. (I) Photothermal catalytic performance of $Co_3O_4$/$CuO_x$ under different temperatures. Reproduced with permission from ref. 27. Copyright 2023, American Chemical Society. (J) Temperature dependence of the redox potentials for $CO_2$ reduction. Reproduced with permission from ref. 152. Copyright 2020, Elsevier.

 

photogenerated electrons can be extracted from deep energy levels through shallow-level bridges and then thermally released to the catalyst surface (Fig. 22B). This photothermal effect not only promotes the electron extraction but also favors charge utilization and surface reactions. Compared to conventional photocatalysis, the catalyst demonstrated significantly higher formation rates for $CH_4$ (11.93 μmol $g^{-1}$ $h^{-1}$) and CO (38.99 μmol $g^{-1}$ $h^{-1}$) during photothermal reactions, representing 108-fold and 300-fold enhancements, respectively (Fig. 22C).

**Promoting the electron/proton mitigation**. The introduction of heat enhances proton/electron transfer, thereby boosting the $CO_2$ conversion rate.[147] For instance, Li *et al.* developed a hydrogen-stored bismuth (Bi–$H_x$) catalyst that significantly boosts $CO_2$-to-CO conversion during the thermal-assisted photocatalytic process (Fig. 22D and E).[148] Within the optimal temperature range of 150–180 °C, the additional thermal energy generated by the increasing temperature benefits the transfer of protons and electrons from Bi–$H_x$ species to the adsorbed $CO_2$, thereby contributing to the production of CO. However, above 180 °C, stored hydrogen in Bi–$H_x$ tends to form $H_2$, limiting proton/electron migration and reducing CO evolution.

**Regulating the desorption/adsorption of $CO_2$ and products**. The local temperature of catalysts can be effectively increased under light illumination *via* lattice vibrations or relaxation of carriers.[52,94] Within a specific temperature range, the elevated temperature promotes the desorption of products and by-products during $CO_2$ conversion, ensuring the timely renewal of catalytic sites and maintaining activity and stability.[149,150] For instance, photo-promoted $H_2$-assisted $CO_2$ reduction to produce $CH_4$ can be realized at 250 °C using $Cu_2O$/graphene as the photocatalyst. Studies have shown that in the gas-phase methanation process, the product $H_2O$ requires relatively high temperatures to desorb from the material surface.[149] As shown in Fig. 22F, control experiments in which the temperature and the amount of added $H_2O$ were varied have revealed the impact of $H_2O$ adsorption/desorption behavior on $CH_4$ production efficiency. These experiments indicate that the adsorbed $H_2O$ molecule on the catalyst surface inhibited $CH_4$ formation. Conversely, the increased temperature favors $H_2O$ desorption, therefore, enhancing $CH_4$ evolution. Generally, a moderate increase in the reaction temperature facilitates $CO_2$ diffusion in the photocatalytic process, thereby enhancing mass transfer efficiency and improving reaction kinetics.[4,151] However, excessively high temperatures can hinder $CO_2$ adsorption on the catalyst surface, reducing overall catalytic efficiency. This occurs because elevated temperatures weaken the interplay between $CO_2$ and active sites, resulting in desorption before the reaction can proceed effectively.[153] Therefore, precisely controlling the local temperature of the photocatalysts to regulate the desorption and adsorption of $CO_2$ and products is essential for enhancing photothermal catalytic efficiency.

**Modulating the catalyst structure**. The complex $CO_2$RR pathways and the imperfect structure of catalysts often result in low selectivity for specific products in light-driven $CO_2$ conversion. Recent studies indicate that during high-temperature photocatalysis, catalysts can undergo *in situ* restructuring under light and/or heat, refining their structure or surface properties to enhance activity and control product distribution.[4,141,144,154] For example, Bai *et al.*[27] used *quasi in situ* XPS to reveal that during thermal-assisted $CO_2$ photoreduction, the $Co_3O_4/CuO_x$ precursor underwent an *in situ* transformation (Fig. 22G and H). With the temperature increasing from 25 to 240 °C, the Cu(I) content in $CuO_x$ increased while the Co(II) content in $Co_3O_4$ decreased. This suggests that strong photothermal effects facilitated the conversion of the $Co_3O_4/CuO_x$ composite into the $Co_3O_4/Cu_2O$ heterojunction. As shown in Fig. 22I, at 240 °C, the $CO_2$-to-$CH_4$ conversion rate reached 6.5 μmol $h^{-1}$, with $CH_4$ selectivity exceeding 99%, which was promoted by the *in situ* formation of the $Co_3O_4/Cu_2O$ catalyst. Thus, understanding the impact of photo-thermal effects on catalyst reconstruction is crucial for improving NIR-light-driven $CO_2$ conversion efficiency.

**Tuning the redox potentials of half-reactions**. According to the Nernst equation, the standard redox potential can be significantly tuned by temperature.[152,155] The photothermal effect induces local temperature variations on the catalyst surface, resulting in either a positive or a negative shift in the redox potential. These potential shifts enable a broader range of catalysts to satisfy the thermodynamic requirements of reactions. For instance, as the temperature rises, the potential of $CO_2$RR shifts positively, indicating that this process is more thermodynamically favorable under elevated temperature conditions. Fig. 22J displays that when the reaction temperature is increased from 25 to 600 °C, the redox potential for $CO_2$ reduction to CO shifts positively from −0.526 V (*vs.* SHE, pH = 7) to −0.162 V (*vs.* SHE, pH = 7), significantly improving the thermodynamic feasibility of $CO_2$-to-CO conversion.[155] Therefore, the photothermal effect may allow more catalysts to reach the thermodynamic requirements for $CO_2$RR by tuning the standard redox potentials.

**4.3.1. Photothermal promoted $CO_2$RR.** The photothermal effect provides additional thermal energy that can accelerate reaction kinetics. It is generally accepted that light-induced heat enhances photoreaction kinetics by facilitating the formation of intermediates, increasing the desorption rate of products, accelerating charge carrier separation, and modifying redox potentials (Fig. 23A and B). The photothermal effect can be caused by the reinforced lattice vibration in the photocatalysts and the relaxation process of photogenerated carriers.[52,94] Typically, semiconductor photocatalysts under ultraviolet-visible (UV-vis) illumination can excite electrons to produce free charge carriers. These carriers may then interact with lattice vibrations or recombine, releasing energy as heat. In contrast, the lower-energy infrared light primarily induces heat accumulation through direct interaction with lattice vibrations. Meanwhile, many of the previously discussed catalysts, such as SPR-based catalysts and metallic catalysts, are capable of inducing a strong photothermal effect under NIR light irradiation.[17,29,116,156,157] Therefore, it is crucial to identify the primary origin of the thermal effect (such as SPR contribution, semiconductor contribution, *etc.*). A clear understanding of these factors is critical for designing rigorous control experiments

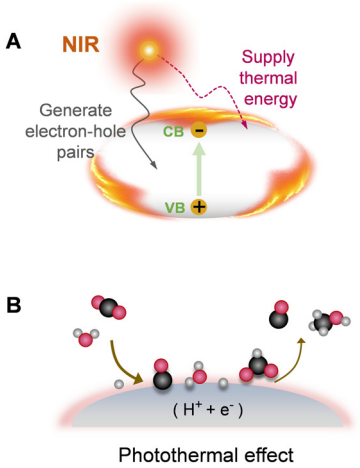


Fig. 23 (A) Photothermal effect for supplying thermal energy and generating electron–hole pairs. (B) Photothermal strategy for promoting NIR-light driven PCO$_2$R.

and uncovering the underlying mechanisms of $CO_2$ conversion driven by NIR light.

For instance, Guo *et al.* reported a $CO_2$RR process operating in a solid–vapor mode, in which a $CuInS_2$ catalyst was fabricated as a thin film, allowing a $CO_2$–$H_2O$ gas mixture to react on its surface.[63] The material exhibited an intrinsic absorption edge at 860 nm, corresponding to a bandgap of 1.44 eV (Fig. 24A). In their study, while maintaining the same light intensity but varying the wavelength range, temperatures of this system were monitored *via* an infrared camera (Fig. 24B). $CuInS_2$ rapidly heated within seconds, and its surface temperatures stabilized above 80 °C after five minutes of illumination, showing excellent photothermal performance. Notably, the photothermal response of $CuInS_2$ under UV-visible light was slower than

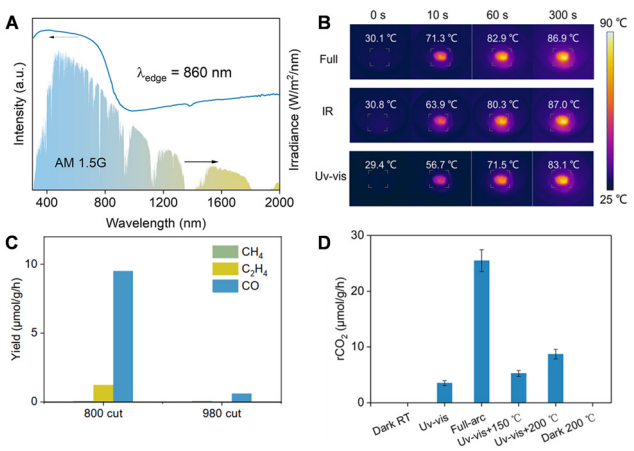


Fig. 24 Photothermal effect promotes $CO_2$ conversion performance. (A) Optical properties of $CuInS_2$ manifested by UV-vis-NIR DRS spectra. (B) Photothermal images of $CuInS_2$ under UV-vis, NIR, and full spectrum light irradiation. (C) Photocatalytic $CO_2$ reduction performance under different long-pass cut-off filters (800 nm and 980 nm). (D) $CO_2$ reduction performance under light irradiation and additional heating. Reproduced with permission from ref. 63. Copyright 2024, American Chemical Society.

under NIR and full-spectrum light, suggesting the inferior photothermal effect of UV-visible light. Under UV-visible light, CO production was only 2.8 μmol $g^{-1}$ $h^{-1}$, whereas it rose to 19.9 μmol $g^{-1}$ $h^{-1}$ when NIR light was also incorporated (UV-visible-NIR), highlighting the significant role of NIR in boosting the $CO_2$ conversion performance. Meanwhile, $CO_2$RR was tested under IR wavelengths above 800 and 980 nm (Fig. 24C), which showed that NIR photons alone (above 800 nm) could also efficiently drive $CO_2$RR. To differentiate between the thermal effect and the role of NIR photons, control experiments involving external heating were conducted (Fig. 24D). As shown, the activity increased from 80 to 200 °C, confirming the promoted effect of photothermal contribution. However, the activity under UV-vis light with external heating at 200 °C remained lower than that under full-spectrum illumination. Considering the photothermal temperature of *ca.* 90 °C, this emphasizes the crucial role of photon synergy over simple heating. It was found that UV-vis-NIR light led to a more negative surface potential than UV-vis alone, indicating that NIR light enhances electron accumulation. Moreover, *in situ* XPS and DRIFTS analyses further revealed that NIR improves $CO_2$ adsorption and activation. Thus, the superior photothermal effect of IR light, combined with enhanced physical adsorption and activation of $CO_2$ and $H_2O$, collectively promotes $CO_2$RR. Also, it has become increasingly important to explore innovative and highly effective strategies for achieving efficient NIR photothermal energy conversion to overcome the limitations of current catalyst designs.[143,158] Recent studies have highlighted that incorporating components with strong NIR photothermal properties into catalytic systems significantly enhances the photothermal conversion efficiency of composite catalysts. For instance, Chen *et al.* successfully developed a sequence of POMs@GO-PEI samples through a combination of covalent grafting and electrostatic adsorption methods (Fig. 25A).[73] In this system, the sheetlike graphene oxide (GO) matrix functions as a highly localized photothermal heater. Under mild and convenient reaction conditions, the synthesized POMs@GO-PEI catalysts efficiently promote the cycloaddition of $CO_2$ using NIR irradiation, utilizing $CO_2$ as a feedstock in organic synthesis. Notably, the heterogeneous catalysts display outstanding photothermal stability along with excellent recyclability. Among a sequence of POMs@GO-PEI samples, the designed SiWCo@GO-PEI materials leverage a low-energy photoredox-driven photothermal catalytic process to significantly boost the cycloaddition reaction (Fig. 25B and C). This approach achieves an outstanding 98.9% epoxide conversion and 99% selectivity, with an impressive TOF of up to 2718 $h^{-1}$ under ambient pressure.

**4.3.2. $H_2$-assisted photothermal $CO_2$ conversion.** In the photothermal enhanced $CO_2$ conversion process, in addition to $H_2O$, $H_2$ is another promising green reagent for facilitating $CO_2$ reduction. Owing to the strong reducing capability of $H_2$ and its different dissociation pathways, the mechanism and thermodynamic characteristics of $CO_2$RR using $H_2$ may differ substantially from those in the $CO_2$RR system using $H_2O$. In addition, the pronounced photothermal effect of NIR light

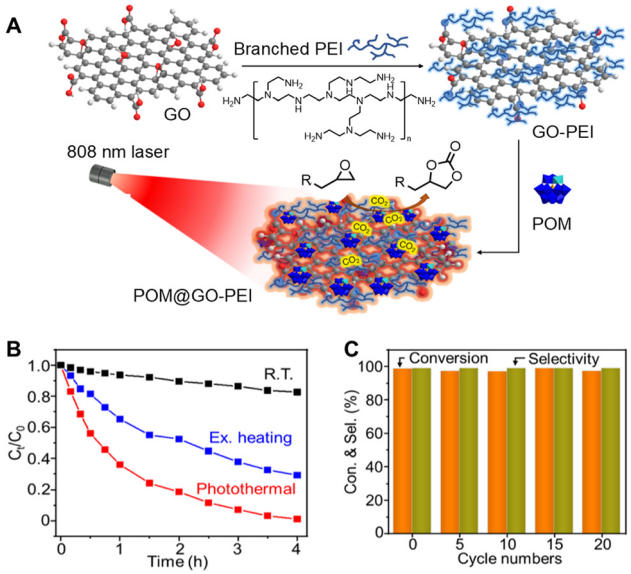


Fig. 25 Photothermal effect facilitates NIR-light-driven $CO_2$ reduction. (A) The preparation of POMs@GO-PEI catalysts and the diagram of photothermal catalytic cycloaddition of $CO_2$ with epoxides. (B) Kinetic curves of $CO_2$ cycloaddition with epichlorohydrin on SiWCo@GO-PEI under the three conditions of room temperature (R.T.), external heating (*ex.* heating), and photothermal condition, with NIR radiation. (C) Reusability of the SiWCo@GO-PEI catalyst. Reproduced with permission from ref. 73. Copyright 2022, American Chemical Society.

might render thermal catalysis a major contributor to $CO_2$ conversion. In $H_2$-assisted photothermal $CO_2$RR, particularly under conditions where thermochemical processes predominate, the process usually follows the mechanism where $H_2$ dissociates into active hydrogen atoms (*H) or hydride ($H^-$), which then participate in the subsequent reduction of adsorbed $CO_2$ molecules.[116,159–161] It is worth noting that the elevated temperatures resulting from the photothermal effect not only promote the activation of adsorbed $H_2$ and $CO_2$ molecules but also accelerate surface mass transfer processes, including adsorption–desorption and diffusion processes. Although conventional thermal catalysis is effective, it generally demands high temperatures and pressures. In comparison, catalysts that harness the photothermal effect under NIR light irradiation can achieve high catalytic activity under milder conditions. In the following section, we will briefly discuss the applications of the photothermal effect and supra-photothermal effect in promoting $H_2$-assisted $CO_2$ conversion (Fig. 26).

*4.3.2.1. Photothermal effect.* For instance, Jia *et al.* designed a series of $TiO_2$ catalysts loaded with Ni NPs, named *x*Ni/$TiO_2$, which exhibited excellent activity for the conversion of $CO_2$ and hydrogen under IR irradiation (Fig. 27A).[116] Notably, the surface temperature of *x*Ni/$TiO_2$ is closely related to the nickel content, confirming that the Ni NPs are primarily responsible for photothermal conversion. In *x*Ni/$TiO_2$, the highly dispersed, small-sized Ni NPs are rich in oxygen vacancies, which enhance their exothermic plasmonic resonance behaviour. In this study, while pure $TiO_2$ exhibited no photocatalytic or photothermal

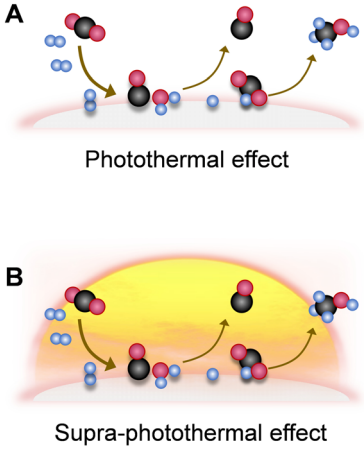


Fig. 26 (A) Photothermal effect and (B) supra-photothermal effect for promoting NIR-light driven $H_2$-assisted $CO_2$ conversion.

catalytic activity for $H_2$-assisted $CO_2$ conversion, the *x*Ni/$TiO_2$ catalyst was effectively activated under infrared light. As shown in Fig. 27B, the temperature of the 8Ni/$TiO_2$ catalyst increases almost linearly with the intensity of the IR light, and the corresponding $CH_4$ production rates also show a linear increase with the rise in the surface temperatures of 8Ni/$TiO_2$. Under optimized conditions, the catalyst achieves nearly 100% selectivity toward methane and a high production rate of 463.9 mmol $g_{Ni}^{-1}$ $h^{-1}$. *In situ* DRIFTS studies suggest that methane formation on the 8Ni/$TiO_2$ catalyst may proceed through a formate-mediated pathway (Fig. 27C). Hydrogen atoms generated from $H_2$ dissociation on the highly dispersed, small-sized Ni nanoparticles rapidly diffuse through overflow processes. These hydrogen species facilitate the conversion of $CO_2$ into formate intermediates, which subsequently lead to methane production. Further analysis revealed that the excellent photothermal catalytic performance of the 8Ni/$TiO_2$ catalyst can be attributed to the uniform distribution and small size of the nickel NPs. These features enable strong infrared light absorption, high photothermal conversion efficiency, and excellent capabilities for $CO_2$ and $H_2$ adsorption and activation.

Ozin *et al.*[162] developed a Ru/silicon nanowire (Ru/SiNW, Fig. 27D) catalyst through the sputter deposition of *ca.* 10 nm Ru nanoparticles onto black silicon nanowires (SiNWs). In this system, the Ru nanoparticles function as the catalytically active sites for the Sabatier reaction ($CO_2 + 4H_2 \rightarrow CH_4 + 2H_2O$), while the SiNWs act as a support and an efficient light-harvesting medium. Owing to its unique three-dimensional morphology, narrow electronic bandgap (1.1 eV), and inherently low optical reflectance, the Ru/SiNW catalyst achieves outstanding photon absorption across the ultraviolet, visible, and near-infrared spectral regions (Fig. 27E). Consequently, under an illumination intensity of 14.5 suns, the Ru/SiNW catalyst achieved a self-induced increase in temperature to approximately 125 °C at 15 psi solely through photothermal effects, without the need for external heating. To further elucidate the activation mechanism, the authors employed a series of high-pass optical filters during the Sabatier reaction (Fig. 27F). These controlled

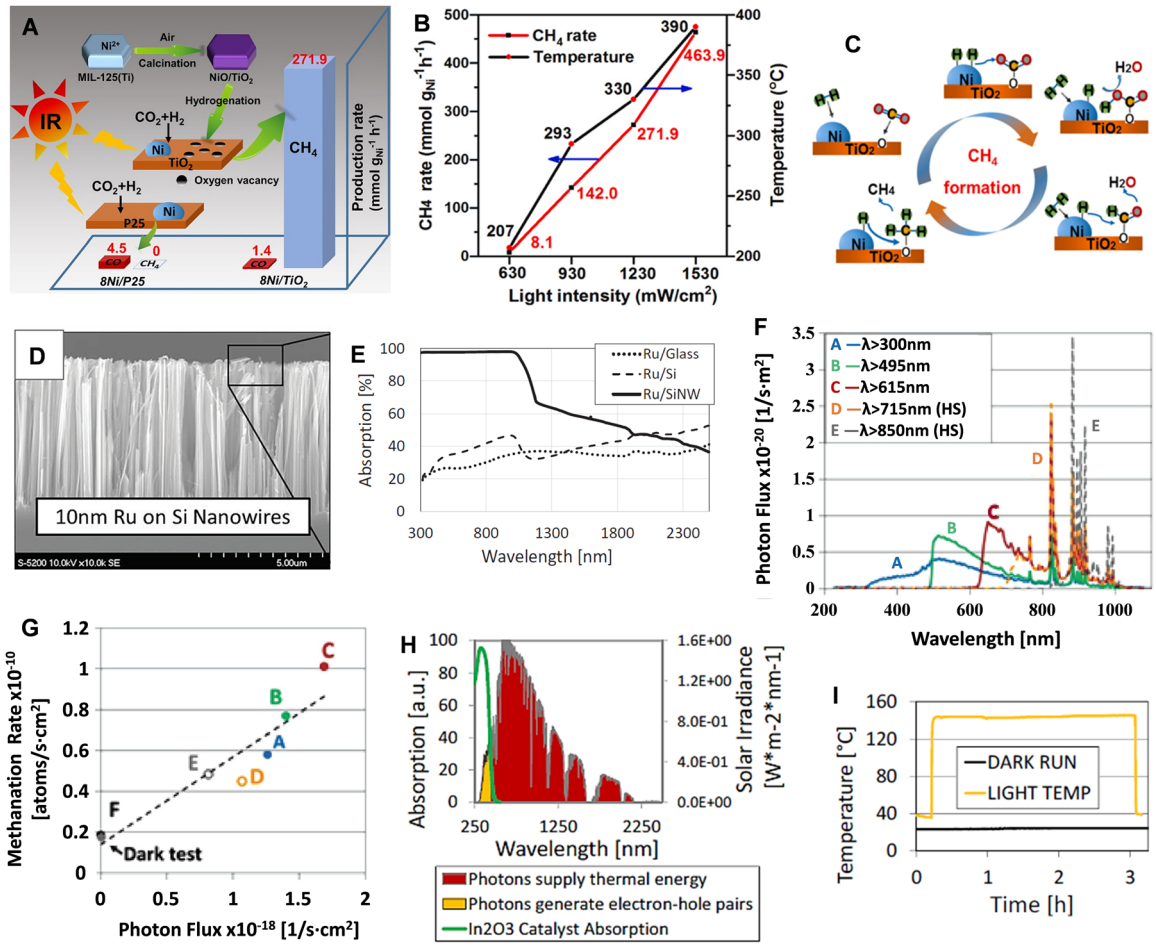


Fig. 27 $H_2$-assisted photothermal $CO_2$ conversion. (A) IR-light-driven photothermal conversion of $CO_2$ to methane over $Ni/TiO_2$. (B) Temperature and corresponding catalytic activity of $Ni/TiO_2$ under different IR irradiation intensities. (C) Schematic description of the $CO_2$ methanation pathways. Reproduced with permission from ref. 116. Copyright 2022, Elsevier. (D) SEM image of 10 nm Ru sputtered Si nanowires (SiNW). (E) The light absorption spectra of Ru/glass, Ru/Si, and Ru/SiNW catalysts. (F) The photon flux of different incident photons. (G) The relationship between the photon flux and $CO_2$ methanation rate. (H) The relative absorption spectrum of the $In_2O_3$ nanoparticle catalyst is shown by the green curve. The shaded areas in different colors represent distinct wavelength ranges within the solar spectrum. (I) Temperature profile over the SiNW materials carried out in the dark and under the Xe lamp. Reproduced with permission from ref. 162. Copyright 2023, Wiley-VCH.

experiments demonstrated that the Ru/SiNW catalyst can facilitate the Sabatier reaction through a synergistic combination of photochemical and thermochemical pathways. More specifically, photons with energies below the SiNW bandgap ($\lambda >$ 1100 nm) are incapable of directly driving the Sabatier reaction through photochemical pathways; instead, their absorption generates thermal energy that promotes the reaction *via* thermochemical activation. In contrast, as illustrated in Fig. 27G, a linear correlation was observed between the flux of photons with energies exceeding the SiNW bandgap (1.1 eV) and the rate of $CO_2$ methanation, thereby providing clear evidence of a photochemical contribution. Notably, the slope of this linear relationship ($\sim 4 \times 10^{-9}$ $CH_4$ molecules per photon) indicates that only a minor fraction of high-energy photons induces photochemical activity, while the majority of photogenerated charge carriers undergo thermalization and recombination, indirectly enhancing the reaction through heat generation. Despite the low quantum efficiency for photochemical activation, the contribution of these photons to the overall catalytic performance is nonetheless significant. In the synergistic process involving both photochemical and photothermal contributions, the Sabatier reaction rate over the Ru/SiNW catalyst was enhanced by a factor of five under photon irradiation within the spectral range of 615 nm $< \lambda <$ 1100 nm, compared to the rate observed under dark conditions at 95 °C. Remarkably, the reaction rate also exhibited an approximate twofold increase when solely irradiated with NIR photons (850 nm $< \lambda <$ 1100 nm). Furthermore, isotope labeling experiments utilizing $^{13}CO_2$ unequivocally verified that the methane product originated from the reduction of $CO_2$ rather than from adventitious carbon sources.

In addition, SiNWs hold significant potential as support materials capable of harvesting solar energy to provide heat to enhance the catalytic performance of various other catalysts immobilized on their surface. To prove this concept, Ozin *et al.* reported that indium oxide ($In_2O_3$) nanoparticles deposited on

 

SiNWs ($In_2O_3$/SiNW) effectively catalyzed the reverse water-gas shift reaction ($CO_2 + H_2 \rightarrow CO + H_2O$). As shown in Fig. 27H, the yellow-shaded region of the solar spectrum delineates the fraction of solar irradiance capable of photochemically activating the $In_2O_3$ nanoparticle catalysts, whereas the red-shaded region corresponds to the portion of solar energy that contributes to heating the catalyst *via* photothermal effects. Notably, the catalytic reaction can be driven entirely by radiant energy without reliance on an external heating source. Specifically, by increasing the irradiation intensity of the xenon lamp to levels exceeding 15 suns, photons within the ultraviolet and visible spectral ranges initiated photochemical activation of the reaction, while sub-bandgap photons—predominantly in the near-infrared (NIR) region—supplied sufficient energy to elevate the temperature of the SiNW support to approximately 145 °C (Fig. 27I). These studies present an effective strategy for the utilization of low-energy NIR light through the photothermal effect to boost $H_2$-assisted $CO_2$ conversion without the need for external heating.

*4.3.2.2. Supra-photothermal effect.* Through modulating the composition, structures, and morphology of catalysts, the photothermal effect can be further reinforced, leading to a supra-photothermal effect. For instance, inspired by the greenhouse effect, Ozin *et al.*[156] fabricated porous-$SiO_2$-encapsulated Ni nanocrystals (named Ni@p-$SiO_2$), which mimic the greenhouse gases, to trap IR photons and heat (Fig. 28A and B). Theoretical calculations demonstrate that the presence of the $SiO_2$ shell reduces thermal radiation by 43%, thereby achieving a supra-photothermal effect and resulting in a temperature increase of 60 K for the Ni particles. The local temperature ($T_{local}$) of Ni@p-$SiO_2$ is estimated to reach nearly 852 K under 2.8 W $cm^{-2}$ illumination due to the supra-photothermal effect

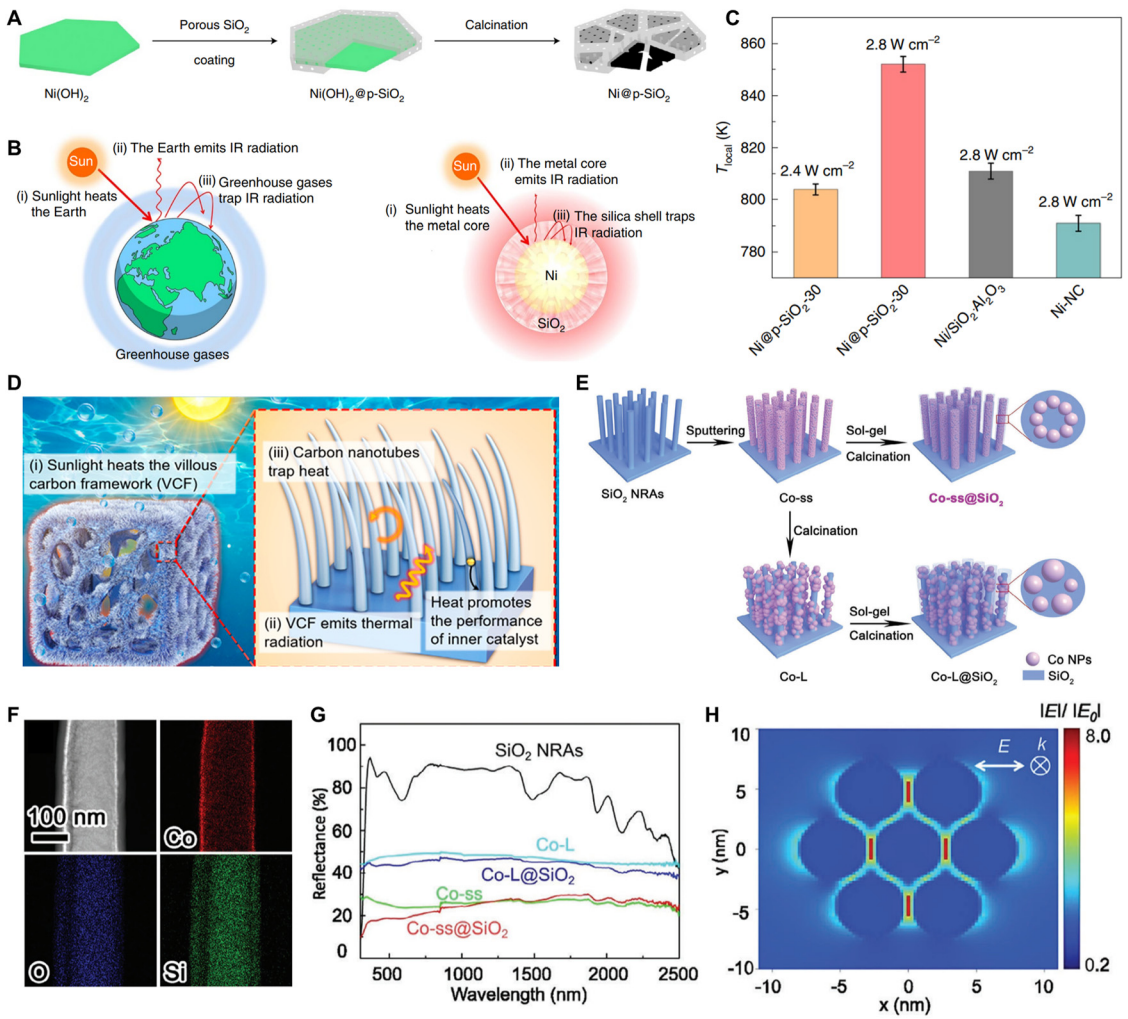


Fig. 28 Supra-photothermal effect facilitates NIR-light-driven $CO_2$ reduction. (A) The synthetic route for Ni@p-$SiO_2$. (B) Diagrams of the natural greenhouse effect and supra-photothermal effect. (C) The estimated local temperatures of different catalysts under various irradiation intensities. Reproduced with permission from ref. 156. Copyright 2021, Springer Nature. (D) Schematic illustration of the polar bear hair-like effect for trapping thermal radiation. Reproduced with permission from ref. 163. Copyright 2022, American Chemical Society. (E) Illustration of the synthetic procedure of Co-ss, Co-ss@$SiO_2$, Co-L, and Co-L@$SiO_2$ samples. (F) The morphological analysis and the elemental distribution images of Co-ss@$SiO_2$. (G) DRS spectra of $SiO_2$ NRAs, Co-ss, Co-ss@$SiO_2$, Co-L, and Co-L@$SiO_2$ samples. (H) Simulated electric field distribution around tightly packed small Co particles. Reproduced with permission from ref. 157. Copyright 2023, Wiley-VCH.

(Fig. 28C), which also contributes to its outstanding $CO_2$RR performance and product selectivity in the photothermal catalytic transformation of $CO_2$ to CO. In nature, animals such as polar bears usually use their fur to resist the cold environment. The fur can prevent heat exchange with the outside world, contributing to reducing the loss of heat. Inspired by this, Zou *et al.*[163] fabricated biomimetic villous carbon frameworks (VCF) which consist of carbon nanotube (CNT) arrays embedded with $FeNi_3$ alloys and carbon frameworks (CF) (Fig. 28D). The hair-like CNT arrays promote the efficient conversion of the energy of the broadband spectrum into heat by restricting heat convection and radiation, thereby achieving a supra-photothermal effect. Recently, leveraging the radiation trapping effect of array structures and the nano-greenhouse effect, He *et al.*[157] prepared $SiO_2$-coated ultrasmall Co nanoparticles (Co-ss@$SiO_2$) on $SiO_2$ nanorod arrays ($SiO_2$ NRAs) (Fig. 28E and F), which exhibit supra-photothermal $CO_2$ methanation activity with an impressive $CH_4$ productivity of 2.3 mol $g_{Co}^{-1}$ $h^{-1}$ and a selectivity of nearly 100%. The ultrasmall size of the Co nanoparticles and the silica shell endow Co-ss@$SiO_2$ with greenhouse-like plasmonic superstructures, which remarkably improve the light-trapping capacity and photothermal conversion ability of this composite photocatalyst (Fig. 28G). In addition, the finite-difference time-domain (FDTD) approach demonstrates that the light-induced electric field around Co-ss@$SiO_2$ is firmly confined within the gaps between adjacent Co atoms of Co-ss@$SiO_2$ catalysts, and the peak intensity of the electric field ($\Delta E/\Delta E_0$) over Co-ss@$SiO_2$ is much higher than that of Co-L@$SiO_2$ ($SiO_2$-coated large Co particles) (Fig. 28H), which is owing to the strong SPR effect of the ultrasmall Co particles. Additionally, the simulated electric field indicates that $SiO_2$ NRAs will promote the light absorption and heat retention abilities of this plasmonic superstructure. Consequently, the supra-photothermal effect contributes to the excellent catalytic performance and selectivity of the Co-ss@$SiO_2$ catalyst. In brief, making full use of the (supra-)photothermal effect induced by low-energy photons holds significant potential in facilitating $CO_2$ photoreduction.

# 5. Summary and outlook

NIR-light-driven $CO_2$ reduction has garnered substantial attention for mitigating climate warming and the energy crisis due to the superiority of NIR light, including deep penetration depth, weak competitive absorption, and photothermal effects. However, developing a photocatalyst with robust NIR light response and desirable conversion efficiency for NIR-light-driven $CO_2$RR is still a formidable task. To tackle this challenge, the key is to design high-efficiency catalysts.

In this review, several design strategies for NIR-responsive photocatalysts have been discussed, including energy band structure regulation strategy, energy transfer strategy, and photothermal utilization strategy. Although these strategies exhibit significant advantages in promoting NIR-light-driven $CO_2$RR, they still have certain limitations (Table 4). To overcome these limitations, the photocatalysts for NIR-light-driven $CO_2$RR should be improved according to the following aspects (Fig. 29).

## 5.1. Prospects for the next NIR-photocatalytic $CO_2$ reduction systems

At present, converting $CO_2$ into multi-carbon ($C_{2+}$) products using NIR light is hindered by poor efficiency and productivity. Therefore, it is crucial to address strategic factors in designing

Table 4 The characteristics and limitations of typical NIR-photocatalysts mentioned in the context

| Design strategy | Photocatalyst type | Characteristics | Limitations |
|---|---|---|---|
| Energy band structure regulation | Narrow-bandgap catalysts | Direct NIR light absorption | (1) Difficult to possess suitable band edge positions<br>(2) Often requiring sacrificial agents |
| | Intermediate-band catalysts | (1) Direct utilization of broad bandgap semiconductors<br>(2) Cascaded electron transitions | (1) Difficult to introduce the intermediate band<br>(2) Often low efficiency |
| | Metallic catalysts | (1) Zero band gap<br>(2) Superb IR light absorption<br>(3) High carrier concentration | Severe carrier recombination |
| | Heterojunction catalysts | (1) Multiple narrow bandgap components<br>(2) Effective charge separation | Complex to construct |
| Energy transfer strategy | Pure SPR catalysts | (1) Local electric field manipulation<br>(2) Hot-electron transfer | (1) Reliance on noble metals<br>(2) Difficult to possess suitable band edge positions |
| | SPR-semiconductor composites | (1) Local electric field manipulation<br>(2) Hot-electron transfer<br>(3) Energy transfer between SPR components with semiconductors<br>(4) Effective charge separation | (1) Reliance on noble metals<br>(2) Matching between SPR components and semiconductors |
| | Up-conversion catalysts | (1) Transforming low-energy photons into high-energy photons<br>(2) Tunable emission wavelength | (1) Low up-conversion quantum yield<br>(2) Reliance on specific wavelength lasers |
| Photothermal utilization strategy | (Supra-)photothermal catalysts | (1) (Supra-)photothermal effect<br>(2) Photothermal synergy | Commonly limited by photothermal conversion efficiency |

 

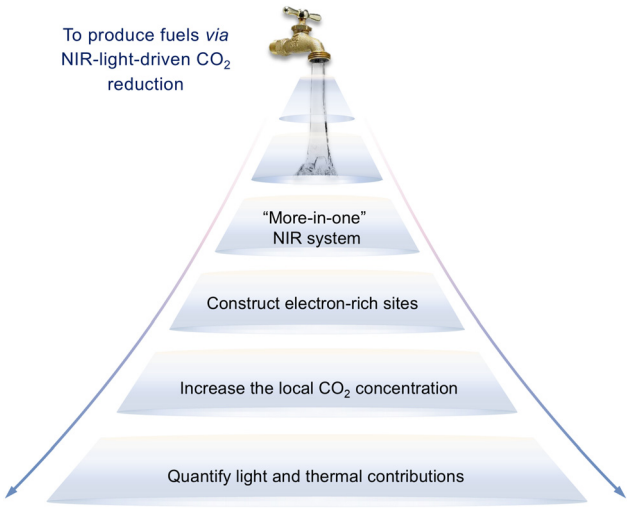


Fig. 29 Future directions to advance the NIR-light-driven $CO_2$RR system.

the next generation of NIR-responsive catalysts to enhance the production of drop-in fuels through the $CO_2$RR process: (1) developing a "more-in-one" NIR system: the efficiencies of single-component catalysts are often limited by factors such as unsuitable electronic structures, low carrier concentrations, weak $CO_2$ adsorption, poor NIR-light absorption, *etc.* To overcome these challenges, it is urgent to design novel multi-component NIR photocatalysts. Integrating cocatalysts, NIR light absorbers, and other functional components into a single system may effectively enhance the NIR light absorption and boost the PCO$_2$R efficiency. For example, incorporating UCNPs or plasmonic nanoparticles into photocatalysts can increase their ability to harvest low-energy NIR photons. Additionally, well-ordered redox-active architectures can improve charge transfer kinetics and the efficiency of surface redox reactions. Therefore, developing "more-in-one" NIR photocatalysts with spatially arranged and composition-tunable bandgaps is a compelling strategy to enhance SCC. (2) Constructing electron-rich sites: designing structures that provide electron-rich reactive sites is beneficial for the deep reduction of $CO_2$ into high-value chemicals. In this regard, materials with metallic properties are particularly effective, as they not only enhance NIR light absorption but also demonstrate excellent activity in converting $CO_2$ into $C_{2+}$ compounds. These metallic materials, usually with zero energy gaps, are highly effective in NIR light utilization and facilitating multiple electron/proton transfer for selective C–C coupling, even under low $CO_2$ concentration conditions. (3) Increasing local $CO_2$ concentration: increasing the local concentration of $CO_2$ near active sites has been shown to improve multi-carbon product selectivity.[164] Enhancing $CO_2$ adsorption, in turn, accelerates $CO_2$ reduction kinetics. Various catalyst modification techniques, such as defect engineering, integration with porous framework materials, and the construction of Lewis acid/base sites, can be employed to elevate local $CO_2$ concentrations around the active sites. (4) Quantify light and thermal contributions: to further optimize NIR-light-driven $CO_2$RR, it is essential to disclose the photothermal mechanism by quantifying the contributions of both light and heat. Cooperatively, the photoinduced carriers and the local thermal effect play pivotal roles in driving the $CO_2$RR process. The photothermal synergy may help steer the reactions by lowering the energy barriers for $CO_2$RR and lead to a greater apparent catalytic efficiency in the photothermal system than the sum of photochemistry and thermochemistry. NIR light, rather than UV or visible light, offers strong photothermal conversion efficiency, especially when using photocatalysts with inherent photothermal conversion capabilities.

However, accurately measuring the actual surface/local temperature of photocatalysts remains challenging, often leading to unreasonable evaluation of the contributions from photocatalytic and thermal catalytic processes.[165] To make reasonable evaluations of the photothermal effect, advanced techniques for accurate reaction temperature measurements should be developed. Additionally, control experiments related to temperatures and light are required simultaneously.

### 5.2. Developing advanced techniques

Nowadays, the progress of NIR-light-driven $CO_2$ reduction is very slow, due to a lack of understanding of its mechanism. To push the development of this field, advanced techniques are supposed to be explored to gain a deep insight into the structure–activity relationships of photocatalysts. Advanced characterization techniques can monitor the variations of $CO_2$ and the photocatalysts, revealing the real $CO_2$ reduction process on the catalyst surface. To make a better comprehension of NIR-light-driven $CO_2$ reduction, it is recommended to develop advanced techniques in the following aspects (Fig. 30).

**5.2.1. *In situ*/*operando* techniques.** To make mechanistic investigations more convincing, *in situ*/*operando* techniques are

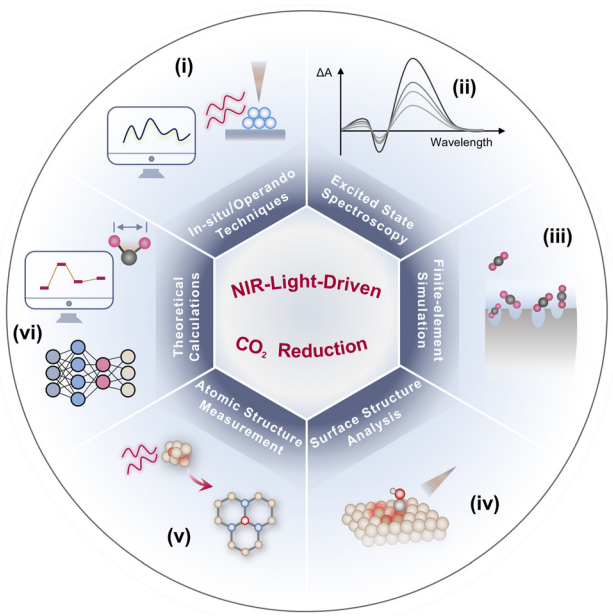


Fig. 30 Prospects of advanced characterization techniques for NIR-light-driven $CO_2$ reduction.

required, which can capture the dynamic changes of catalysts and reaction intermediates. For example, *in situ* RAIRS spectra can monitor the transformations of adsorbed intermediates, while *operando* XPS spectra can reveal surface chemical state changes and structural transformations of the photocatalysts.[31] Hence, the development of high time-resolved *in situ/operando* techniques is key to achieving more sensitive detection.

**5.2.2. Excited state spectroscopy.** Understanding the excited state properties is also crucial for improving the overall photocatalytic processes. For instance, the separation efficiency of carriers seriously impacts $PCO_2R$ efficiency. To understand carrier behaviors, excited state spectroscopy methods, such as TAS and PL spectroscopy, should be extensively studied.[18,166] The lower intensity of PL spectra indicates a longer lifetime of carriers, while the emission wavelength can reflect the energy band gaps for some semiconductors. TAS is an important technique for studying carrier dynamics, as it can measure charge separation efficiency, carriers' lifetime, and the carrier transfer process by monitoring the properties of excited states or unstable intermediates. Advanced excited state spectroscopy is essential for revealing the real carrier behaviors during the $PCO_2R$ process.

**5.2.3. *Operando* $CO_2$ distribution simulations.** Lewis-acid/base site construction[133] and defect engineering[32] are commonly employed to significantly enhance the $CO_2$ affinity of catalysts. However, it remains challenging for current techniques to effectively monitor the *operando* changes of $CO_2$ distribution on the photocatalyst surface. Therefore, to better depict local $CO_2$ concentration variations, finite element (FEM) simulations are conducted based on physical and chemical principles.[167] This approach visualizes the local $CO_2$ distribution around specific structures in photocatalysts, guiding the development of modification methods.

**5.2.4. Surface structure analysis.** Surface structure analysis is necessary for heterogeneous catalysis. For instance, XPS and surface-enhanced Raman spectroscopy (SERS) are usually conducted to analyze the chemical state and bond structures on the surface of photocatalysts.[168,169] Although these two techniques are well-established, analyzing the corresponding spectra remains challenging. How to make a reasonable curve fitting of XPS spectra and identify the bond information from Raman spectra are pivotal for recognizing the active sites of photocatalysts, which require further development. To obtain absolute energy band structures of photocatalysts, ultraviolet photoelectron spectroscopy (UPS) needs to be further studied and improved.[170] In addition, reflection–absorption infrared spectroscopy (RAIRS) is an essential method for capturing key intermediates adsorbed on the surface of photocatalysts,[171] which discloses the transformation process of $CO_2$ during the reduction reaction. In short, to determine the surface chemical states and bond information of catalysts, techniques such as XPS, UPS, SERS and RAIRS are recommended.

**5.2.5. Atomic structure measurement.** Precisely measuring the atomic structures of active sites is a necessary step for exploring the structure–activity relationship of photocatalysts. Generally, the changes in the coordination structure around the active site can significantly influence the catalytic activity. Thus, further progress in atomic structure measurement techniques, such as EXAFS and X-ray absorption near edge structure spectroscopy (XANES),[47,72] is conducive to investigating how the structures of catalytic sites affect the photocatalytic performance, which in return can guide the design of active sites.

**5.2.6. Theoretical calculations.** Based on the measured catalyst structures and the adsorbed intermediates, possible reaction pathways can be proposed. Unfortunately, current experimental conditions cannot definitively determine the real pathway; therefore theoretical approaches, such as DFT calculations, are used to figure out the most favored reaction route. By calculating the electronic properties of photocatalysts and analyzing the Gibbs energy variations of potential mechanisms, the structure–activity relationships of photocatalysts can also be well elucidated.[172] However, the calculated models of the catalysts are still approximate and simplified, failing to fully present the real reaction conditions. In addition, to improve the efficiency of the optimization for catalysts and experimental conditions, machine learning (ML) methods have been developed.[173] With reasonable models and efficient algorithms, the most likely catalyst and reaction condition can be figured out quickly, saving significant time in designing suitable catalysts and screening optimal reaction conditions. However, ML methods exhibit a strong reliance on the size of the database and the authenticity of the training set data, which further restricts both the applicability and reliability of the computational results. Therefore, in order to enhance the alignment of computational models with real-world reaction scenarios, it is urgent to develop novel computational methodologies and cutting-edge computer techniques in greater depth.

Overall, the progress of NIR-light-driven $CO_2$ reduction requires the advancement of various characterization techniques, and these advanced techniques can offer a guidance for designing reasonable photocatalysts and photocatalytic systems.

### 5.3. Making a reasonable evaluation of NIR-light-driven $CO_2$RR performance

Recent studies have revealed that some published research claims on NIR-light-driven $CO_2$RR and its catalytic mechanisms may be thermodynamically unfeasible.[91,92,174] These errors might arise from a limited understanding of NIR-light-driven $CO_2$RR, improper experimental methods, overlooking key factors in the analysis, or carbon contamination interference. Any mistakes can lead to a range of issues, such as prolonged experimental durations, excessive resource wastes, incorrect interpretations of structure–activity relationships, and erroneous conclusions. Thus, to obtain reliable experimental results, researchers must critically assess the reported literature and perform experiments with meticulous care. In this section, two main components for promoting best practices toward reliable NIR-driven $CO_2$RR are presented, namely general steps and key considerations (Fig. 31).

As shown in Fig. 31, step-by-step guides regarding catalyst preparation, experimental system building, performance evaluation, and mechanism investigation are summarized. When preparing catalysts, the key is to design catalysts that can

 

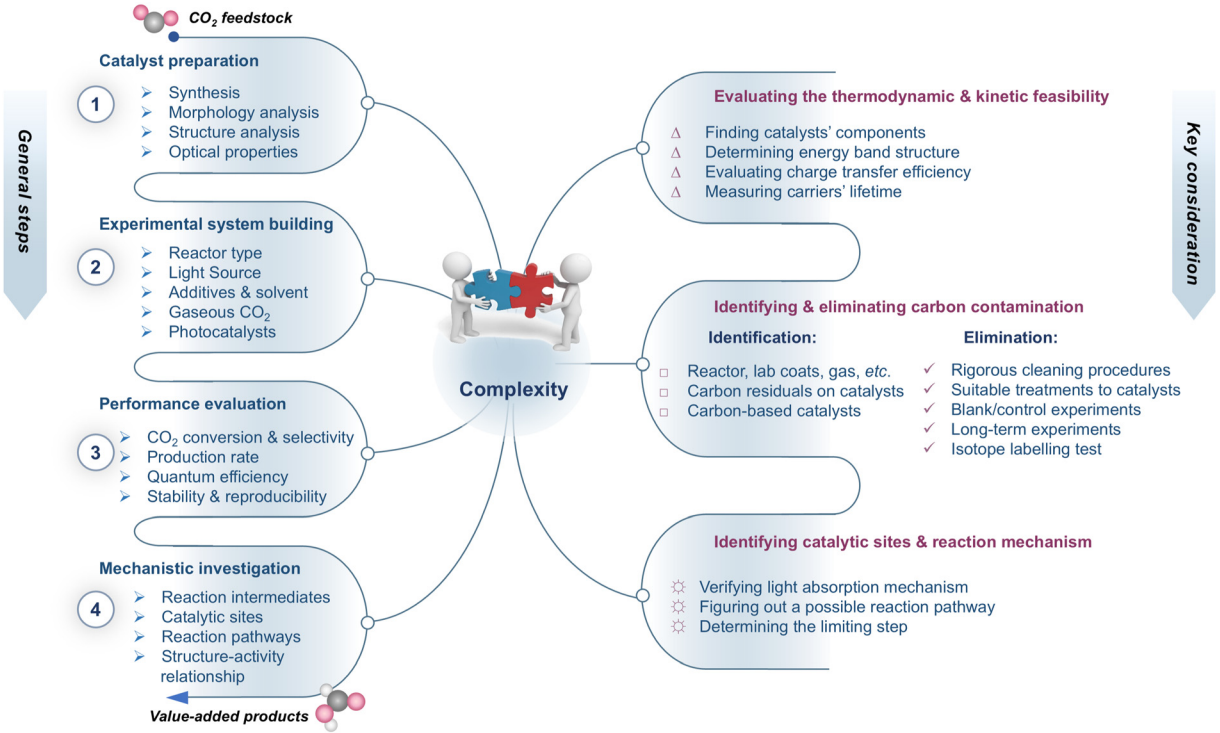


Fig. 31 General steps for reliable NIR-light-driven $CO_2$ reduction.

effectively respond to NIR light, promote carrier separation, and facilitate $CO_2$RR. The process typically involves several steps, including synthesis, basic structural and morphological characterization, and optical property analysis. Depending on their efficiency in capturing NIR light, the synthesized catalysts can be narrow-bandgap materials, or they can be functionally assembled components. Then, it is feasible to conduct some basic characterization, such as morphology, structure, and optical properties, which lays the foundation for understanding the characteristics of the catalyst and further elucidating its chemical state and electronic structure.

To build an experimental system, a suitable reactor, NIR light sources with different intensities, solvents with or without additives, gaseous $CO_2$, and the designed photocatalyst must be properly assembled for the next step of performance testing. In this system setup, key operational details such as irradiation intensities and wavelengths, reaction temperature, $CO_2$ feed pressure and concentration, cocatalyst presence, catalyst dosage, reaction time, and solvent pH are crucial for optimizing $CO_2$ conversion processes. Precise control over these factors ensures experimental consistency, which is critical for reliable and robust fundamental research. Once these parameters are established, the photocatalytic $CO_2$ reduction performance can then be evaluated.

For performance evaluation, important metrics include SCC, $CO_2$ conversion efficiency, product selectivity, production rate, quantum efficiency, and stability of the photosynthetic system under NIR light. These metrics offer deep insights into efficiency benchmarking, enabling the comparison of state-of-the-art results across different photocatalysts.

The mechanistic investigation primarily focuses on interfacial charge behaviors and reaction pathways. In this step, detailed studies using excited-state spectroscopic techniques, such as TAS and time-resolved photoluminescence (TRPL), are essential for understanding the charge-carrier dynamics in semiconductors and identifying key efficiency-limiting factors in the possible mechanism under NIR light excitation. Moreover, advanced experimental methods like *in situ*/*operando* XPS, XAS, and RAIRS are essential for detecting and differentiating the information at the reaction interfaces. Additionally, modeling studies using DFT calculations are instrumental in exploring and understanding the structure–property–performance relationship to achieve high photocatalytic performance.

To enhance the reliability of NIR-light-driven $CO_2$RR results, three key aspects should be considered. Firstly, before conducting experiments, it is crucial to fully understand the complexities associated with NIR-light-driven $CO_2$RR processes and recognize the factors that can interfere with the results. Proper planning is essential to ensure that the experiment is carried out with care and consideration. The complexity arises from four main factors: (1) thermodynamic and kinetic complexity: long-wavelength light-activatable $CO_2$RR has inherent challenges. The C═O bond in $CO_2$ is chemically inert, necessitating a huge input of energy to break it.[4,23] The $CO_2$RR process involves multiple steps with numerous electron/proton transfers, leading to various intermediates that may recombine at different stages. (2) Interaction of photo-reduction and -oxidation reactions: the interaction between the paired reactions adds additional complexity to the research. (3) Influence of various parameters: the reactivity is highly sensitive to

parameters such as the type of photocatalyst, the choice of reaction device, pH, and the addition of cocatalysts and sacrificial agents (if used).[23] (4) Challenges of excluding carbon contamination: because of the low yield of products in NIR-light-driven $CO_2$RR, carbon contamination can lead to indistinguishable false and true positive results.[92]

It is widely acknowledged that understanding the thermodynamic and kinetic factors, along with their mechanisms, has always been a key challenge in $PCO_2R$ research. Thus, the first key consideration in performing NIR-light-driven $CO_2$RR is to evaluate the thermodynamic and kinetic feasibility of the system. This can be estimated by identifying catalysts' components, determining the energy band structure, evaluating charge transfer efficiency, and measuring carrier lifetimes. We have learned much from conventional $H_2$-assisted $CO_2$ reduction in terms of catalyst design. However, different catalysts used in photocatalytic systems may follow distinct mechanisms, which require specific thermodynamic forces to drive the reactions accordingly. Thus, to successfully achieve NIR-light-driven $CO_2$RR, the catalysts' components—including substrates, semiconductors, cocatalysts, and other light-absorbing components—must first be carefully checked. For example, photocatalysis in conventional semiconductor-based systems typically involves photon absorption, which requires the energy of incident light to be higher than the band gaps.[18,62] The band edge positions of conventional semiconductors should be adjusted to provide sufficient thermodynamic driving force, allowing the paired reactions to occur concurrently. For another example, SPR-mediated catalysis (see Section 4.2.1) differs from conventional semiconductor-based systems, which cannot drive reactions without sufficient photon energy.[98,175] Quite differently, the SPR-induced highly energetic hot electrons in plasmonic materials can directly drive redox reactions. The generated hot carriers are engaged in these processes including photo/thermo-conversion, and then may boost the reaction with $CO_2$ under the lower thermodynamic driving force. For example, Hu *et al.* demonstrated that Au rod@CuPd core–shell composites have achieved $CO_2$ reduction under near-infrared light illumination (800 nm, *ca.* 1.55 eV). A key issue in this study is that, without a sacrificial agent, the low-energy photons are insufficient to overcome the reaction barrier of $CO_2$RR. To address this issue and better understand how low-energy photons interact with catalysts and $CO_2$, the research team employed *in situ* XPS to study SPR-mediated light–matter interactions within the reaction system.[59]

Another important consideration is the exclusion of carbon contamination.[91,92,176,177] The process of eliminating carbon contamination throughout the experiment involves lots of details. Carbon contamination from organic reagents present in reactors, lab coats, low-purity gases, *etc.*, can be eliminated through rigorous cleaning procedures. Carbon contamination on the surface of photocatalysts, originating from solvents, reactants, and surfactants used during synthesis, can be mitigated by employing suitable treatment methods: washing the catalysts with ethanol/water, annealing the catalysts under high-temperature conditions, and using Ar or $O_2$ plasma to clean the surfaces of catalysts. Carbon contamination originating from the light-induced self-degradation of carbon-containing catalysts can be eliminated or recognized by selecting stable carbon-based photocatalysts, using low-energy photon-driven systems, and conducting structural stability characterization before and after reactions. Further, carbon contamination can also be eliminated *via* blank/control experiments, long-term performance tests, and isotope labeling experiments. These solutions help enhance data reliability and avoid the false-positive results.

The third consideration is the identification of the catalytic sites as well as reaction mechanisms. The distribution, numbers, and nature of these active sites directly influence the overall performance of the catalyst. Identifying these active sites is crucial for understanding the parameters that determine activity and for uncovering potential catalytic mechanisms. This review does not delve further into this aspect.

Inspired by the above general steps and key considerations for conducting NIR-light-driven $CO_2$RR studies, we hope this section also serves as a valuable reference for conducting $PCO_2R$ experiments that utilize the full spectrum of sunlight. A dependable breakthrough in the field of $PCO_2R$ can establish a robust basis for both fundamental studies and industrial applications.

### 5.4. Increasing the feasibilities in practical application for $CO_2$ capture

In this section, the considerations for scaling up laboratory $PCO_2R$ to the industrial level are discussed, along with the relevant application examples. Current systems of artificial photosynthesis are far from meeting the requirements for practical application, because of their low efficiency ($<1\%$) and productivity.[23] To break through the low-efficiency bottleneck of the $PCO_2R$ system and improve its potential for practical application, it is crucial to consider the future strategic design of the $PCO_2R$ system. This includes many specific considerations for scaling up $PCO_2R$-based applications or integrating them as part of a chain partnership with existing applications in the industry (Fig. 32): (i) regulating the paired half-reactions in NIR-light-driven $CO_2$ reduction systems,[20] (ii) using $CO_2$ as a building block in direct organic synthesis,[73] (iii) making full use of the photothermal effect to enhance $CO_2$ conversion *via* the integration of $CO_2$ conversion with existing high-temperature catalytic reactions, including Sabatier reaction,[162] reverse water gas shift (RWGS) reaction,[178] reverse Boudouard (RB) reaction,[179] and (iv) engineering cascaded $CO_2$ conversion systems.[180]

**5.4.1. Regulation of the paired half-reactions in NIR-light-driven $CO_2$ reduction systems.** One of the feasible directions to further reinforce the overall activity of NIR-light-driven $CO_2$ reduction systems is to elaborately regulate the paired half-reactions. Typically, $CO_2$RR is coupled with water oxidation half-reaction. Unfortunately, water oxidation reaction possesses sluggish charge transfer kinetics and relatively high reaction potential, lowering the efficiency of the overall $CO_2$ photoreduction system.[20,181,182] This disadvantage is particularly pronounced in NIR-light-driven $CO_2$ reduction processes, where

 

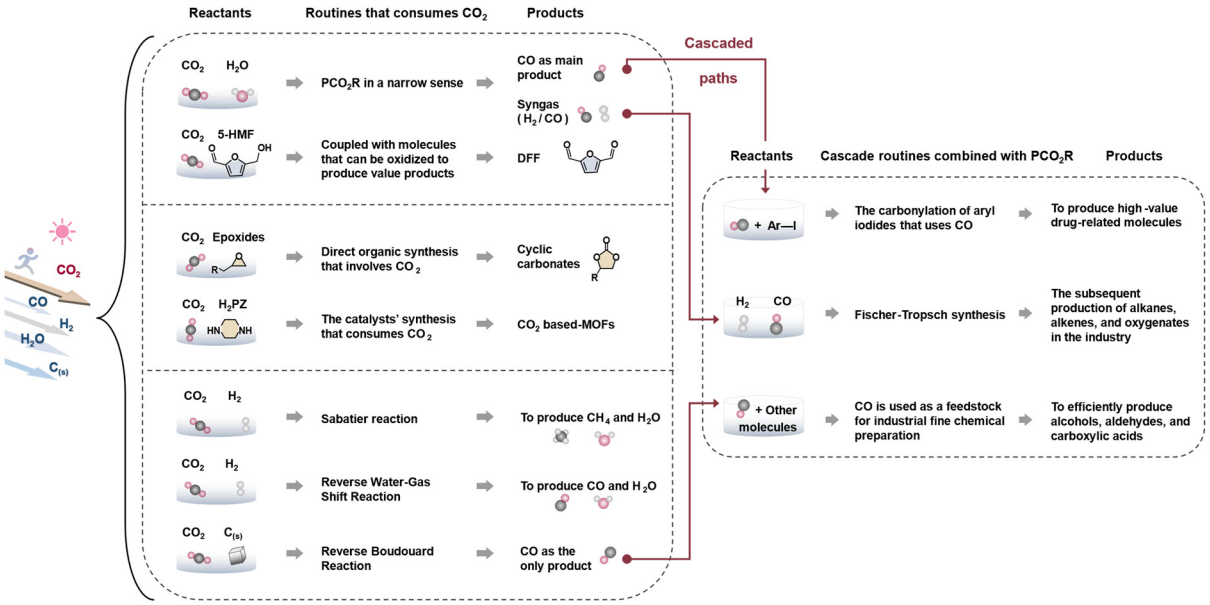


Fig. 32 Future design directions of $CO_2$ chemical utilization systems driven by NIR light.

the electronic structures of the photocatalysts must be rigorously manipulated to ensure that both water oxidation and $CO_2$ reduction can occur simultaneously and efficiently. To get rid of this limitation and enhance efficiency, the water oxidation reaction has been replaced by some sacrificial agent oxidation reactions, such as the oxidation of TEOA, $Na_2S$, $Na_2S_2O_3$, *etc.* While this approach can improve the performance of the NIR-light-driven $CO_2$ reduction system,[56] it comes with significant drawbacks. Sacrificial agents are costly and environmentally unfriendly, and the oxidation products generated from these agents typically have low economic values, which limits the practicality and sustainability of the system. Therefore, to further elevate the efficiency and economic values of the overall NIR-light-driven $CO_2$RR process, the water oxidation reaction could be substituted by high-value oxidation reactions, like the oxidation reactions of biomass, biomass-derived molecules, or plastics-derived molecules.[183–187] For instance, Zhang *et al.* fabricated a binuclear Re-Ru heterogeneous catalyst, co-upgrading plastic waste and $CO_2$ into value-added chemicals by photocatalysis.[184] Recently, the oxidation reaction of 5-hydroxymethylfurfural (5-HMF), a by-product generated during the biodiesel production, is regarded as a good replacement for water oxidation (Fig. 32).[188] Moreover, narrow-band gap photocatalysts, such as $WS_2$, $Bi_2S_3$, and $MoS_2$, are candidates for NIR-light-driven 5-HMF oxidation. Chu *et al.*[187] developed a NiOOH/$MoS_2$ catalyst, achieving a high 5-HMF conversion rate (5.24 mmol $g^{-1}$ $h^{-1}$) and an outstanding 5-formyl-2-furancarboxylic acid (FFCA) product selectivity of 95.4% by NIR irradiation. Hence, this coupling approach not only enhances the efficiency of $CO_2$ photoreduction but also adds significant economic value by enabling the upgrading of biomass and waste plastics, contributing to a more sustainable and economically viable NIR-light-driven photocatalysis system. Noteworthily, to achieve this goal, novel NIR-light-responsive catalysts need to be developed with the capability to effectively catalyze multiple reactions simultaneously. In a word, rationally designing paired half-reactions for the NIR-light-driven $CO_2$ reduction system holds great promise but requires further in-depth exploration.

**5.4.2. Using $CO_2$ as a building block in organic synthesis.** It is noteworthy that great efforts are currently being made to enable the fixation of $CO_2$, with a focus on advancing carbon capture and storage techniques.[189] However, the high bond energy of C=O bonds in $CO_2$ molecules (750 kJ $mol^{-1}$) limits the efficient conversion of $CO_2$. Fortunately, many other chemical bonds possess much lower bond energies than that of C=O in $CO_2$ (*e.g.*, C–H: 430 kJ $mol^{-1}$, C–C: 336 kJ $mol^{-1}$, C–O: 327 kJ $mol^{-1}$).[190,191] Introducing $CO_2$ molecules into the activation processes of these bonds helps lower the activation barriers of $CO_2$ and promote its conversion into fine chemicals. In other words, $CO_2$ can be a building block for photocatalytic synthesis of organic compounds. In this approach, $CO_2$ can be utilized from two main perspectives: (i) conducting an organic chemical reaction that involves $CO_2$ as a reactant and (ii) conducting the catalyst synthesis that consumes $CO_2$. As shown in Fig. 32, conducting an organic chemical reaction that involves $CO_2$ as a reactant is a feasible approach for $CO_2$ utilization.[192] For instance, using NIR as the driving energy, the synthesis of cyclic carbonates from the cycloaddition of $CO_2$ with epoxides has been successfully conducted on multicomponent catalysts, demonstrating the effectiveness of using NIR photons.[73] From the perspective of sustainable chemistry, the onsite NIR-driven organic photoredox catalysis involving $CO_2$ conversion becomes an extendable routine that consumes this greenhouse gas. The second direction is to synthesize the catalysts that consume $CO_2$. Recently, it has been reported that $CO_2$ can be inserted into the terminal alkynes or N–H bonds to form carboxylate ligands, which can then be used to prepare

$CO_2$-based MOFs.[193,194] It should be noted that these $CO_2$-based MOFs require a synthetic temperature of 25–70 °C. Therefore, because of the photothermal effect, NIR light can be utilized as an easily available heat source to elevate the reaction temperature to facilitate the synthesis of $CO_2$-based MOFs, further promoting $CO_2$ capture. In short, with the unique photothermal effect of NIR photons, $CO_2$ can be involved in various organic reactions, consumed in the synthesis of functional catalysts, and applied in other applications. These developments in $CO_2$ fixation are regarded as potential pathways to realize solar energy utilization and environmental sustainability.

**5.4.3. Integration of $CO_2$ conversion with existing catalytic reactions in the industry.** Given the pioneering works that initially demonstrated photothermal catalytic $CO_2$RR,[162,195,196] research on catalysts exhibiting photothermal effects for $CO_2$RR has since begun to proliferate. It is noted that the targeted activation of $CO_2$ and $H_2$ can be mutually promoted by heat in the presence of light, making it attractive to use a photochemical and thermochemical hybrid method for the enhanced conversion of $CO_2$. During the photo-promoted thermal catalytic process, the excited carriers and the localized photothermal effect co-contribute to promoting the $CO_2$RR, further boosting the reactivity, particularly in the $CO_2$ methanation. For example, the Ru@SiNW catalyst, one of the earliest attempts focusing on photothermal catalysis for the Sabatier reaction ($CO_2 + H_2 \rightarrow CH_4 + H_2O$), can absorb a wide range of wavelengths across the full spectral regions.[162] Consequently, photocatalytic $CO_2$ methanation rates over these light harvesters are impressively high. Such photothermal catalysts could achieve excellent performance under mild conditions, offering competitive advantages over conventional heterogeneous catalysts used in thermal catalytic processes. Moreover, photothermal $CO_2$ conversion holds the promise to be incorporated into the current chemical industrial infrastructures. As shown in the schematic representation (Fig. 32), the integrability of $PCO_2R$ with other industrial-scale technologies is highly feasible, offering promising routes for producing valuable products from gaseous $CO_2$ through established reactions. Recently, $PCO_2R$ has been popularly integrated into the RWGS reaction ($CO_2 + H_2 \rightarrow H_2O + CO$) in which the process has been achieved using $H_2$ as a reductant.[178] The RWGS reactions occur spontaneously at mild temperatures as their Gibbs free energy remains negative until the temperature reaches 820 °C, producing $H_2$/CO syngas. Another scenario is the RB reaction, where $CO_2$ and solid-phase carbon are used as reactants. This reaction is also favored and has been evidenced by many studies, with CO being generated as the product ($CO_2 + C \rightarrow CO$).[179,197] In a word, these pioneering discoveries are highly crucial for enabling the transition of $CO_2$ conversion from the laboratory-level stage to the industrial-level stage.

**5.4.4. Engineering cascaded $CO_2$ conversion systems.** While $PCO_2R$ processes can produce many valuable chemical raw materials, such as CO, $CH_4$, and syngas, existing studies rarely consider the continuous utilization and transformation of these products. Thus, effectively converting the downstream products of $CO_2$ photoreduction into value-added chemicals through cascaded reactions will open new research avenues toward practical applications. Among the products of $CO_2$ photoreduction, CO and syngas ($H_2$/CO) have been commonly used in industrial production, such as in Fischer–Tropsch synthesis (FTS) and carbonylation processes. Based on the above, two considerations are envisioned for the cascaded $CO_2$ conversion: (i) direct cascading $PCO_2R$ with FTS technologies and (ii) tandem upgrading $PCO_2R$ products with the carbonylation reactions. It should be noted that there may be other strategies for directly utilizing $CO_2$ photoreduction products; here, we present only two examples to illustrate how $CO_2$ fixation can be achieved in this aspect. In the $PCO_2R$ process, many photocatalysts have been dedicated to producing syngas, simultaneously generating CO and $H_2$. For example, the SCM-Ni/$SiO_2$ composites can produce $H_2$ and CO with 1 : 1 mole ratio by photocatalysis.[198] $Bi_2S_3/Cd_XZn_{1-X}S$ catalysts have demonstrated their extremely high activity for the production of $H_2$ and CO (33.10 and 32.11 μmol $g^{-1}$ $h^{-1}$).[158] Being a mature route, syngas (a mixture of $H_2$ and CO in different ratios) has been widely used as a reactant in the FTS procedures.[4] Thus, more efforts should be devoted to the direct combination of the $PCO_2R$ and FTS technologies to scale up the solar-driven $CO_2$ reforming. In another cascaded $CO_2$ conversion system, CO can be utilized as a reactant in carbonylation reactions. For instance, during the carbonylation process to synthesize diethyltoluamide, the CO conversion rate can reach more than 85%. At the same time, these cascaded conversion approaches also provide easy and affordable strategies for labeling organic molecules with $^{13}C$ isotopes. The successful achievement of cascaded reactions offers an important and feasible way for upgrading $PCO_2R$ products into fine products.[180] We believe that, by ingeniously designing the cascaded catalytic systems, more exciting discoveries leading to practical and scalable $CO_2$ chemical utilization systems driven by NIR light are on the horizon.

In summary, various significant advances and breakthroughs in NIR-light-driven $CO_2$ reduction have been realized over the past decade, making a step towards the full utilization of sunlight for $CO_2$RR. Several strategies, including energy band structure regulation strategy, energy transfer strategy, and photothermal utilization strategy, have been explored for synthesizing NIR-photocatalysts. Many NIR-photocatalysts fabricated using these strategies have expanded the spectral absorption range of the photocatalytic systems from the UV to the NIR wavebands, while simultaneously possessing suitable energy band structures for $CO_2$RR and its paired half-reaction. However, the efficiency of $PCO_2R$ under NIR irradiation is still not satisfactory and falls short of requirements for practical applications. One of the main problems is the severe carrier recombination during the $PCO_2R$ process. To enhance the charge separation efficiency, strategies such as heterojunction engineering and energy transfer strategies are recommended for catalyst design. To enhance the $PCO_2R$ activity and product selectivity, we have also outlined potential directions for the next generation of NIR-light-responsive $CO_2$RR

 

systems. Additionally, the lack of deep understanding of the mechanisms underlying NIR-light-driven $CO_2$RR limits the development of this field. Meanwhile, carbon contamination resulting from the photodegradation of organic additives can further complicate the mechanism. Thus, it is essential to explore advanced characterization methods and establish a reasonable workflow to avoid false-positive results and deepen the understanding of NIR-light-driven $CO_2$RR. To increase the feasibility of $PCO_2R$ in practical applications, a promising approach is to combine the downstream products of $PCO_2R$ with other valuable reactions to achieve cascaded conversion of $CO_2$. Besides, the economic value of the photocatalytic system can be effectively increased by coupling the $CO_2$ reduction process with value-added paired half-reactions. Overall, the study of NIR-light-driven $CO_2$ reduction is still in its early stage despite progress in recent years. As NIR-photocatalytic $CO_2$ reduction is continuously developing, there is no doubt that it will find applications in diverse fields, such as biological therapy, photoelectrocatalysis, and organic synthesis. Hence, selecting suitable application scenarios and continuously developing NIR-photocatalysts will be crucial in advancing $CO_2$ photoconversion toward industrial applications.

## Data availability

No primary research results, software or code have been included and no new data were generated or analysed as part of this review.

## Conflicts of interest

There are no conflicts to declare.

## Acknowledgements

This work was supported by the National Natural Science Foundation of China (22105133), Natural Science Foundation of Sichuan Province of China (2023NSFSC1085), China Scholarship Council, Science and Technology Project of the State Administration for Market Regulation (2022MK111), Fundamental Research Funds for the Central Universities, and the Creative Research Initiative (CRI, RS-2023-00221668) program through the National Research Foundation (NRF) of Korea.

## References

1 C. F. Shih, T. Zhang, J. Li and C. Bai, *Joule*, 2018, **2**, 1925–1949.
2 Thoning: Trends in globally-averaged $CO_2$ determined from NOAA Global Monitoring Laboratory measurements, DOI: 10.15138/9N0H-ZH07, (accessed May 2024).
3 Climate at a Glance: Global Time Series, https://www.ncei.noaa.gov/access/monitoring/climate-ata-glance/global/time-series, (accessed May 2024).
4 S. Fang and Y. H. Hu, *Chem. Soc. Rev.*, 2022, **51**, 3609–3647.
5 E. V. Kondratenko, G. Mul, J. Baltrusaitis, G. O. Larrazábal and J. Pérez-Ramírez, *Energy Environ. Sci.*, 2013, **6**, 3112–3135.
6 C. Song, *Catal. Today*, 2006, **115**, 2–32.
7 G. Centi and S. Perathoner, *Catal. Today*, 2009, **148**, 191–205.
8 S. Mori, W.-C. Xu, T. Ishidzuki, N. Ogasawara, J. Imai and K. Kobayashi, *Appl. Catal., A*, 1996, **137**, 255–268.
9 I.-Y. Jeon, Y.-R. Shin, G.-J. Sohn, H.-J. Choi, S.-Y. Bae, J. Mahmood, S.-M. Jung, J.-M. Seo, M.-J. Kim, D. Wook Chang, L. Dai and J.-B. Baek, *Proc. Natl. Acad. Sci. U. S. A.*, 2012, **109**, 5588–5593.
10 S. Bhattacharjee, M. Rahaman, V. Andrei, M. Miller, S. Rodríguez-Jiménez, E. Lam, C. Pornrungroj and E. Reisner, *Nat. Synth.*, 2023, **2**, 182–192.
11 J. Zhu, G. Zhou, Y. Tong, L. Chen and P. Chen, *Adv. Funct. Mater.*, 2024, 2420177.
12 H. Wang, Y. Tong and P. Chen, *Nano Energy*, 2023, **118**, 108967.
13 M. Asadi, K. Kim, C. Liu, A. V. Addepalli, P. Abbasi, P. Yasaei, P. Phillips, A. Behranginia, J. M. Cerrato, R. Haasch, P. Zapol, B. Kumar, R. F. Klie, J. Abiade, L. A. Curtiss and A. Salehi-Khojin, *Science*, 2016, **353**, 467–470.
14 J. Tian, J. Yu, Q. Tang, J. Zhang, D. Ma, Y. Lei and Z.-T. Li, *Mater. Futures*, 2022, **1**, 042104.
15 S. Wang, X. Han, Y. Zhang, N. Tian, T. Ma and H. Huang, *Small Struct.*, 2021, **2**, 2000061.
16 L. K. Putri, B.-J. Ng, W.-J. Ong, S.-P. Chai and A. R. Mohamed, *Adv. Energy Mater.*, 2022, **12**, 2201093.
17 Y. Li, M. Wen, Y. Wang, G. Tian, C. Wang and J. Zhao, *Angew. Chem., Int. Ed.*, 2021, **60**, 910–916.
18 J.-Y. Zeng, X.-S. Wang, B.-R. Xie, Q.-R. Li and X.-Z. Zhang, *J. Am. Chem. Soc.*, 2022, **144**, 1218–1231.
19 Y. Wang and T. He, *J. Mater. Chem. A*, 2021, **9**, 87–110.
20 Q. Hu, Z. Zhang, D. He, J. Wu, J. Ding, Q. Chen, X. Jiao and Y. Xie, *J. Am. Chem. Soc.*, 2024, **146**, 16950–16962.
21 M. Halmann, *Nature*, 1978, **275**, 115–116.
22 T. Inoue, A. Fujishima, S. Konishi and K. Honda, *Nature*, 1979, **277**, 637–638.
23 S. Fang, M. Rahaman, J. Bharti, E. Reisner, M. Robert, G. A. Ozin and Y. H. Hu, *Nat. Rev. Methods Primers*, 2023, **3**, 61.
24 J. Xu, Z. Ju, W. Zhang, Y. Pan, J. Zhu, J. Mao, X. Zheng, H. Fu, M. Yuan, H. Chen and R. Li, *Angew. Chem., Int. Ed.*, 2021, **60**, 8705–8709.
25 S. Yang, W. J. Byun, F. Zhao, D. Chen, J. Mao, W. Zhang, J. Peng, C. Liu, Y. Pan, J. Hu, J. Zhu, X. Zheng, H. Fu, M. Yuan, H. Chen, R. Li, M. Zhou, W. Che, J.-B. Baek, J. S. Lee and J. Xu, *Adv. Mater.*, 2024, **36**, 2312616.
26 X. Li, Y. Sun, J. Xu, Y. Shao, J. Wu, X. Xu, Y. Pan, H. Ju, J. Zhu and Y. Xie, *Nat. Energy*, 2019, **4**, 690–699.
27 S. Bai, W. Jing, G. He, C. Liao, F. Wang, Y. Liu and L. Guo, *ACS Nano*, 2023, **17**, 10976–10986.
28 L. Hurtado, A. Mohan, U. Ulmer, R. Natividad, A. A. Tountas, W. Sun, L. Wang, B. Kim, M. M. Sain and G. A. Ozin, *Chem. Eng. J.*, 2022, **435**, 134864.

29 W. Ma, J. Sun, S. Yao, Y. Wang, G. Chen, G. Fan and Y. Li, *Angew. Chem., Int. Ed.*, 2023, **62**, e202313784.
30 X. Shi, Y. Huang, Y. Bo, D. Duan, Z. Wang, J. Cao, G. Zhu, W. Ho, L. Wang, T. Huang and Y. Xiong, *Angew. Chem., Int. Ed.*, 2022, **61**, e202203063.
31 X. Zu, Y. Zhao, X. Li, R. Chen, W. Shao, L. Li, P. Qiao, W. Yan, Y. Pan, Q. Xu, J. Zhu, Y. Sun and Y. Xie, *Angew. Chem., Int. Ed.*, 2022, **62**, e202215247.
32 Y. Shen, C. Ren, L. Zheng, X. Xu, R. Long, W. Zhang, Y. Yang, Y. Zhang, Y. Yao, H. Chi, J. Wang, Q. Shen, Y. Xiong, Z. Zou and Y. Zhou, *Nat. Commun.*, 2023, **14**, 1117.
33 C. Gao, S. Chen, Y. Wang, J. Wang, X. Zheng, J. Zhu, L. Song, W. Zhang and Y. Xiong, *Adv. Mater.*, 2018, **30**, 1704624.
34 A. Mavridi-Printezi, A. Menichetti, M. Guernelli and M. Montalti, *Nanoscale*, 2021, **13**, 9147–9159.
35 H. Kumagai, Y. Tamaki and O. Ishitani, *Acc. Chem. Res.*, 2022, **55**, 978–990.
36 F. Yu, X. Jing, Y. Wang, M. Sun and C. Duan, *Angew. Chem., Int. Ed.*, 2021, **60**, 24849–24853.
37 L. Ye, H. Wang, X. Jin, Y. Su, D. Wang, H. Xie, X. Liu and X. Liu, *Sol. Energy Mater. Sol. Cells*, 2016, **144**, 732–739.
38 T. Arai, S. Sato and T. Morikawa, *Energy Environ. Sci.*, 2015, **8**, 1998–2002.
39 B. Tahir, M. Tahir and N. S. Amin, *Appl. Surf. Sci.*, 2015, **338**, 1–14.
40 J. C. S. Wu, H.-M. Lin and C.-L. Lai, *Appl. Catal., A*, 2005, **296**, 194–200.
41 T.-V. Nguyen and J. C. S. Wu, *Appl. Catal., A*, 2008, **335**, 112–120.
42 X. Ji, R. Guo, J. Tang, Y. Miao, Z. Lin, L. Hong, Y. Yuan, Z. Li and W. Pan, *ACS Appl. Energy Mater.*, 2022, **5**, 2862–2872.
43 J. Wang, T. Bo, B. Shao, Y. Zhang, L. Jia, X. Tan, W. Zhou and T. Yu, *Appl. Catal., B*, 2021, **297**, 120498.
44 S. Si, H. Shou, Y. Mao, X. Bao, G. Zhai, K. Song, Z. Wang, P. Wang, Y. Liu, Z. Zheng, Y. Dai, L. Song, B. Huang and H. Cheng, *Angew. Chem., Int. Ed.*, 2022, **61**, e202209446.
45 S. Chakraborty, R. Das, M. Riyaz, K. Das, A. K. Singh, D. Bagchi, C. P. Vinod and S. C. Peter, *Angew. Chem., Int. Ed.*, 2023, **62**, e202216613.
46 L. Zhao, J. Bian, X. Zhang, L. Bai, L. Xu, Y. Qu, Z. Li, Y. Li and L. Jing, *Adv. Mater.*, 2022, **34**, 2205303.
47 H. Ou, S. Ning, P. Zhu, S. Chen, A. Han, Q. Kang, Z. Hu, J. Ye, D. Wang and Y. Li, *Angew. Chem., Int. Ed.*, 2022, **61**, e202206579.
48 Q. Liu, Z. Chen, W. Tao, H. Zhu, L. Zhong, F. Wang, R. Zou, Y. Lei, C. Liu and X. Peng, *J. Mater. Chem. A*, 2020, **8**, 11761–11772.
49 R. Xu, D.-H. Si, S.-S. Zhao, Q.-J. Wu, X.-S. Wang, T.-F. Liu, H. Zhao, R. Cao and Y.-B. Huang, *J. Am. Chem. Soc.*, 2023, **145**, 8261–8270.
50 X. Li, L. Li, G. Chen, X. Chu, X. Liu, C. Naisa, D. Pohl, M. Löffler and X. Feng, *Nat. Commun.*, 2023, **14**, 4034.
51 S. Wang, Z. Ding and X. Wang, *Chem. Commun.*, 2015, **51**, 1517–1519.
52 J. Zhu, W. Shao, X. Li, X. Jiao, J. Zhu, Y. Sun and Y. Xie, *J. Am. Chem. Soc.*, 2021, **143**, 18233–18241.
53 X. Chen, Y. Zhou, Q. Liu, Z. Li, J. Liu and Z. Zou, *ACS Appl. Mater. Interfaces*, 2012, **4**, 3372–3377.
54 J. Di, C. Chen, C. Zhu, P. Song, M. Duan, J. Xiong, R. Long, M. Xu, L. Kang, S. Guo, S. Chen, H. Chen, Z. Chi, Y.-X. Weng, H. Li, L. Song, M. Wu, Q. Yan, S. Li and Z. Liu, *Nano Energy*, 2021, **79**, 105429.
55 B. Su, Y. Kong, S. Wang, S. Zuo, W. Lin, Y. Fang, Y. Hou, G. Zhang, H. Zhang and X. Wang, *J. Am. Chem. Soc.*, 2023, **145**, 27415–27423.
56 L. Liang, X. Li, J. Zhang, P. Ling, Y. Sun, C. Wang, Q. Zhang, Y. Pan, Q. Xu, J. Zhu, Y. Luo and Y. Xie, *Nano Energy*, 2020, **69**, 104421.
57 X. Li, L. Liang, Y. Sun, J. Xu, X. Jiao, X. Xu, H. Ju, Y. Pan, J. Zhu and Y. Xie, *J. Am. Chem. Soc.*, 2019, **141**, 423–430.
58 C. Chen, C. Ye, X. Zhao, Y. Zhang, R. Li, Q. Zhang, H. Zhang and Y. Wu, *Nat. Commun.*, 2024, **15**, 7825.
59 C. Hu, X. Chen, J. Low, Y.-W. Yang, H. Li, D. Wu, S. Chen, J. Jin, H. Li, H. Ju, C.-H. Wang, Z. Lu, R. Long, L. Song and Y. Xiong, *Nat. Commun.*, 2023, **14**, 221.
60 M. Yu, X. Lv, A. Mahmoud Idris, S. Li, J. Lin, H. Lin, J. Wang and Z. Li, *J. Colloid Interface Sci.*, 2022, **612**, 782–791.
61 L.-Y. Lin, S. Kavadiya, B. B. Karakocak, Y. Nie, R. Raliya, S. T. Wang, M. Y. Berezin and P. Biswas, *Appl. Catal., B*, 2018, **230**, 36–48.
62 L. Liang, X. Li, Y. Sun, Y. Tan, X. Jiao, H. Ju, Z. Qi, J. Zhu and Y. Xie, *Joule*, 2018, **2**, 1004–1016.
63 C. Liao, Z. He, F. Wang, Y. Liu and L. Guo, *ACS Nano*, 2024, **18**, 35480–35489.
64 X. Wu, W. Zhang, J. Li, Q. Xiang, Z. Liu and B. Liu, *Angew. Chem., Int. Ed.*, 2023, **62**, e202213124.
65 F. Zhuang, L. Jing, H. Xiang, C. Li, B. Lu, L. Yan, J. Wang, Y. Chen and B. Huang, *Adv. Sci.*, 2024, **11**, 2402256.
66 X. Xu, C. Randorn, P. Efstathiou and J. T. S. Irvine, *Nat. Mater.*, 2012, **11**, 595–598.
67 G. Wang, B. Huang, X. Ma, Z. Wang, X. Qin, X. Zhang, Y. Dai and M.-H. Whangbo, *Angew. Chem., Int. Ed.*, 2013, **52**, 4810–4813.
68 X. Y. Kong, W. L. Tan, B.-J. Ng, S.-P. Chai and A. R. Mohamed, *Nano Res.*, 2017, **10**, 1720–1731.
69 Y. L. Wang, T. Nie, Y. H. Li, X. L. Wang, L. R. Zheng, A. P. Chen, X. Q. Gong and H. G. Yang, *Angew. Chem., Int. Ed.*, 2017, **56**, 7430–7434.
70 J. Li, X. Wu, W. Pan, G. Zhang and H. Chen, *Angew. Chem., Int. Ed.*, 2018, **57**, 491–495.
71 H. Jia, A. Du, H. Zhang, J. Yang, R. Jiang, J. Wang and C. Zhang, *J. Am. Chem. Soc.*, 2019, **141**, 5083–5086.
72 J. Li, W. Pan, Q. Liu, Z. Chen, Z. Chen, X. Feng and H. Chen, *J. Am. Chem. Soc.*, 2021, **143**, 6551–6559.
73 X. Chen, M. Wei, A. Yang, F. Jiang, B. Li, O. A. Kholdeeva and L. Wu, *ACS Appl. Mater. Interfaces*, 2022, **14**, 5194–5202.
74 Y. Cai, F. Luo, Y. Guo, F. Guo, W. Shi and S. Yang, *Molecules*, 2023, **28**, 2142.

 

75 V. R. Nair and V. S. Kodialbail, *Environ. Sci. Pollut. Res.*, 2020, **27**, 14441–14453.
76 Y. Pan, X. Yuan, L. Jiang, H. Wang, H. Yu and J. Zhang, *Chem. Eng. J.*, 2020, **384**, 123310.
77 C. Han, B. K. Kundu, Y. Liang and Y. Sun, *Adv. Mater.*, 2024, **36**, 2307759.
78 R. Chen, K. Qiu, D. C. Y. Leong, B. K. Kundu, C. Zhang, P. Srivastava, K. E. White, G. Li, G. Han, Z. Guo, C. G. Elles, J. Diao and Y. Sun, *Biosens. Bioelectron.*, 2023, **239**, 115604.
79 B. D. Ravetz, A. B. Pun, E. M. Churchill, D. N. Congreve, T. Rovis and L. M. Campos, *Nature*, 2019, **565**, 343–346.
80 B. K. Kundu, C. Han, P. Srivastava, S. Nagar, K. E. White, J. A. Krause, C. G. Elles and Y. Sun, *ACS Catal.*, 2023, **13**, 8119–8127.
81 A. M. Smith, M. C. Mancini and S. Nie, *Nat. Nanotechnol.*, 2009, **4**, 710–711.
82 Pragti, B. K. Kundu, R. Chen, J. Diao and Y. Sun, *Adv. Healthcare Mater.*, 2025, **14**, 2403272.
83 X. Zhao, S. He, W. Chi, X. Liu, P. Chen, W. Sun, J. Du, J. Fan and X. Peng, *Adv. Sci.*, 2022, **9**, 2202885.
84 X. Wang, F. Wang, Y. Sang and H. Liu, *Adv. Energy Mater.*, 2017, **7**, 1700473.
85 D. C. Cabanero and T. Rovis, *Nat. Rev. Chem.*, 2025, **9**, 28–45.
86 B. Kumar Kundu, N. Bashar, P. Srivastava, C. G. Elles and Y. Sun, *Chem. – Eur. J.*, 2024, **30**, e202402856.
87 B. K. Kundu, G. Han and Y. Sun, *J. Am. Chem. Soc.*, 2023, **145**, 3535–3542.
88 J. Hou, Z. Wang, W. Kan, S. Jiao, H. Zhu and R. V. Kumar, *J. Mater. Chem.*, 2012, **22**, 7291–7299.
89 J. Dankar, V. Rouchon, C. Pagis, M. Rivallan and M. El-Roz, *Inorg. Chem. Front.*, 2023, **10**, 7155–7166.
90 Y. Liu, D. Shen, Q. Zhang, Y. Lin and F. Peng, *Appl. Catal., B*, 2021, **283**, 119630.
91 J. You, M. Xiao, S. Liu, H. Lu, P. Chen, Z. Jiang, W. Shangguan, Z. Wang and L. Wang, *J. Mater. Chem. A*, 2023, **11**, 10149–10154.
92 Y. Zhang, D. Yao, B. Xia, M. Jaroniec, J. Ran and S.-Z. Qiao, *ACS Energy Lett.*, 2022, **7**, 1611–1617.
93 A. M. Alotaibi, S. Sathasivam, B. A. D. Williamson, A. Kafizas, C. Sotelo-Vazquez, A. Taylor, D. O. Scanlon and I. P. Parkin, *Chem. Mater.*, 2018, **30**, 1353–1361.
94 J. Wang, Y. Li, L. Deng, N. Wei, Y. Weng, S. Dong, D. Qi, J. Qiu, X. Chen and T. Wu, *Adv. Mater.*, 2017, **29**, 1603730.
95 M. Sun, B. Zhao, F. Chen, C. Liu, S. Lu, Y. Yu and B. Zhang, *Chem. Eng. J.*, 2021, **408**, 127280.
96 F. Fresno, A. Iglesias-Juez and J. M. Coronado, *Top. Curr. Chem.*, 2023, **381**, 21.
97 M. Evstigneev, in *Introduction to Semiconductor Physics and Devices*, ed. M. Evstigneev, Springer International Publishing, Cham, 2022, pp. 171–196.
98 X. Meng, L. Liu, S. Ouyang, H. Xu, D. Wang, N. Zhao and J. Ye, *Adv. Mater.*, 2016, **28**, 6781–6803.
99 S. Yang, W. Dai, W. Zheng and J. Wang, *Coord. Chem. Rev.*, 2023, **475**, 214913.
100 J. Kim, J.-A. Lin, J. Kim, I. Roh, S. Lee and P. Yang, *Nat. Catal.*, 2024, **7**, 977–986.
101 W. Ghosh and B. Dam, *FEMS Microbiol. Rev.*, 2009, **33**, 999–1043.
102 J. Li, Y. Tian, Y. Zhou, Y. Zong, N. Yang, M. Zhang, Z. Guo and H. Song, *Trans. Tianjin Univ.*, 2020, **26**, 237–247.
103 L. Jiang, K. Wang, X. Wu and G. Zhang, *Sol. RRL*, 2021, **5**, 2000326.
104 L. Shi, X. Ren, Q. Wang, W. Zhou and J. Ye, *J. Mater. Chem. A*, 2021, **9**, 2421–2428.
105 B. Wang, H. Chen, W. Zhang, H. Liu, Z. Zheng, F. Huang, J. Liu, G. Liu, X. Yan, Y.-X. Weng, H. Li, Y. She, P. K. Chu and J. Xia, *Adv. Mater.*, 2024, **36**, 2312676.
106 J. Hao, D. Yang, J. Wu, B. Ni, L. Wei, Q. Xu, Y. Min and H. Li, *Chem. Eng. J.*, 2021, **423**, 130190.
107 W. Dai, J. Yu, S. Luo, X. Hu, L. Yang, S. Zhang, B. Li, X. Luo and J. Zou, *Chem. Eng. J.*, 2020, **389**, 123430.
108 Z. Zhang, X. Liu, Y. Li, H. Yu, W. Li and H. Yu, *Appl. Catal., B*, 2022, **319**, 121960.
109 J. Li, X. Liu, X. Wu, Z. Liu, Z. Zhao, Y. Liu, S. Dou and Y. Xiao, *Adv. Sci.*, 2024, **11**, 2405668.
110 C. Lu, X. Li, J. Li, L. Mao, M. Zhu, Q. Chen, L. Wen, B. Li, T. Guo and Z. Lou, *Chem. Eng. J.*, 2022, **445**, 136739.
111 S. Li, Z. Li, J. Yue, H. Wang, Y. Wang, W. Su, G. I. N. Waterhouse, L. Liu, W. Zhang and Y. Zhao, *Angew. Chem., Int. Ed.*, 2024, **63**, e202407638.
112 Z. Guo, B. Shen, Z. Jiang, N. Wu and Y. You, *Ind. Eng. Chem. Res.*, 2024, **63**, 18931–18939.
113 L.-Y. Lin, C. Liu and T.-T. Hsieh, *J. Catal.*, 2020, **391**, 298–311.
114 X. Y. Kong, Y. Y. Choo, S.-P. Chai, A. K. Soh and A. R. Mohamed, *Chem. Commun.*, 2016, **52**, 14242–14245.
115 H. Jiang, S. Gong, S. Xu, P. Shi, J. Fan, V. Cecen, Q. Xu and Y. Min, *Dalton Trans.*, 2020, **49**, 5074–5086.
116 Q. Li, Y. Gao, M. Zhang, H. Gao, J. Chen and H. Jia, *Appl. Catal., B*, 2022, **303**, 120905.
117 X. Jiao, K. Zheng, Z. Hu, Y. Sun and Y. Xie, *ACS Cent. Sci.*, 2020, **6**, 653–660.
118 X. Wang, K. Maeda, A. Thomas, K. Takanabe, G. Xin, J. M. Carlsson, K. Domen and M. Antonietti, *Nat. Mater.*, 2009, **8**, 76–80.
119 B. V. Lotsch and W. Schnick, *Chem. – Eur. J.*, 2007, **13**, 4956–4968.
120 Z. Hu, G. Liu, X. Chen, Z. Shen and J. C. Yu, *Adv. Mater.*, 2016, **26**, 4445–4455.
121 X. Jiao, Z. Hu, Y. Wu, K. Zheng, L. Li, S. Zhu, W. Shao, J. Zhu, Y. Pan and Y. Sun, *Sci. China Mater.*, 2022, **65**, 985–991.
122 W. L. Barnes, A. Dereux and T. W. Ebbesen, *Nature*, 2003, **424**, 824–830.
123 S. A. Maier, *Plasmonics: Fundamentals and Applications*, Springer US, New York, NY, 2007.
124 S. Linic, P. Christopher and D. B. Ingram, *Nat. Mater.*, 2011, **10**, 911–921.
125 M. Rycenga, C. M. Cobley, J. Zeng, W. Li, C. H. Moran, Q. Zhang, D. Qin and Y. Xia, *Chem. Rev.*, 2011, **111**, 3669–3712.
126 F. J. García de Abajo, *ACS Photonics*, 2014, **1**, 135–152.

127 K.-L. Lee, M.-L. You and P.-K. Wei, *ACS Appl. Nano Mater.*, 2019, **2**, 1930–1939.
128 S. Song, C. Xin, W. Liu, W. Shang, T. Liu, W. Peng, J. Hou and Y. Shi, *Angew. Chem., Int. Ed.*, 2025, **64**, e202415173.
129 T. Atay, J.-H. Song and A. Nurmikko, in *Conference on Lasers and Electro-Optics/International Quantum Electronics Conference and Photonic Applications Systems Technologies*, Optica Publishing Group, San Francisco, California, 2004, p. IPDB7.
130 K. Kolwas, A. Derkachova and M. Shopa, *J. Quant. Spectrosc. Radiat. Transfer*, 2009, **110**, 1490–1501.
131 J. J. Mock, M. Barbic, D. R. Smith, D. A. Schultz and S. Schultz, *J. Chem. Phys.*, 2002, **116**, 6755–6759.
132 K. L. Kelly, E. Coronado, L. L. Zhao and G. C. Schatz, *J. Phys. Chem. B*, 2003, **107**, 668–677.
133 S. Gong, Y. Niu, X. Liu, C. Xu, C. Chen, T. J. Meyer and Z. Chen, *ACS Nano*, 2023, **17**, 4922–4932.
134 A. A. Ansari and M. Sillanpää, *Renewable Sustainable Energy Rev.*, 2021, **151**, 111631.
135 W. Yang, X. Li, D. Chi, H. Zhang and X. Liu, *Nanotechnology*, 2014, **25**, 482001.
136 B. S. Richards, D. Hudry, D. Busko, A. Turshatov and I. A. Howard, *Chem. Rev.*, 2021, **121**, 9165–9195.
137 G. Chen, H. Qiu, P. N. Prasad and X. Chen, *Chem. Rev.*, 2014, **114**, 5161–5214.
138 X. Zhao, Q. Liu, X. Li, H. Li, Z. Shen, H. Ji and T. Ma, *Angew. Chem., Int. Ed.*, 2023, **62**, e202219214.
139 Q. Zhang, F. Yang, Z. Xu, M. Chaker and D. Ma, *Nanoscale Horiz.*, 2019, **4**, 579–591.
140 J. Xiao, X. Hou, L. Zhao and Y. Li, *J. Catal.*, 2017, **346**, 70–77.
141 X. Chang, T. Wang and J. Gong, *Energy Environ. Sci.*, 2016, **9**, 2177–2196.
142 A. Corma and H. Garcia, *J. Catal.*, 2013, **308**, 168–175.
143 F. Wang, Y. Huang, Z. Chai, M. Zeng, Q. Li, Y. Wang and D. Xu, *Chem. Sci.*, 2016, **7**, 6887–6893.
144 M. Ghoussoub, M. Xia, P. N. Duchesne, D. Segal and G. Ozin, *Energy Environ. Sci.*, 2019, **12**, 1122–1142.
145 L. Wang, Y. Wang, Y. Cheng, Z. Liu, Q. Guo, M. N. Ha and Z. Zhao, *J. Mater. Chem. A*, 2016, **4**, 5314–5322.
146 F. Yu, C. Wang, Y. Li, H. Ma, R. Wang, Y. Liu, N. Suzuki, C. Terashima, B. Ohtani, T. Ochiai, A. Fujishima and X. Zhang, *Adv. Sci.*, 2020, **7**, 2000204.
147 Y. Li, C. Wang, M. Song, D. Li, X. Zhang and Y. Liu, *Appl. Catal., B*, 2019, **243**, 760–770.
148 Y. Li, D. Hui, Y. Sun, Y. Wang, Z. Wu, C. Wang and J. Zhao, *Nat. Commun.*, 2021, **12**, 123.
149 D. Mateo, J. Albero and H. García, *Energy Environ. Sci.*, 2017, **10**, 2392–2400.
150 Y.-F. Xu, P. N. Duchesne, L. Wang, A. Tavasoli, F. M. Ali, M. Xia, J.-F. Liao, D.-B. Kuang and G. A. Ozin, *Nat. Commun.*, 2020, **11**, 5149.
151 S. Ning, H. Xu, Y. Qi, L. Song, Q. Zhang, S. Ouyang and J. Ye, *ACS Catal.*, 2020, **10**, 4726–4736.
152 Z. Ma, W. Liu, W. Yang, W. Li and B. Han, *Fuel*, 2021, **286**, 119490.
153 L. Zhang, C. Li, Y. Liu, C. Xu and Y. Zhang, *npj Comput. Mater.*, 2024, **10**, 132.
154 C. Foo, Y. Li, K. Lebedev, T. Chen, S. Day, C. Tang and S. C. E. Tsang, *Nat. Commun.*, 2021, **12**, 661.
155 B. Han, W. Wei, L. Chang, P. Cheng and Y. H. Hu, *ACS Catal.*, 2016, **6**, 494–497.
156 M. Cai, Z. Wu, Z. Li, L. Wang, W. Sun, A. A. Tountas, C. Li, S. Wang, K. Feng, A.-B. Xu, S. Tang, A. Tavasoli, M. Peng, W. Liu, A. S. Helmy, L. He, G. A. Ozin and X. Zhang, *Nat. Energy*, 2021, **6**, 807–814.
157 M. Cai, C. Li, X. An, B. Zhong, Y. Zhou, K. Feng, S. Wang, C. Zhang, M. Xiao, Z. Wu, J. He, C. Wu, J. Shen, Z. Zhu, K. Feng, J. Zhong and L. He, *Adv. Mater.*, 2024, **36**, 2308859.
158 H. He, X. Gao, K. Xu, H. Li, Y. Hu, C. Yang and F. Fu, *Chem. Eng. J.*, 2022, **450**, 138266.
159 B. An, Z. Li, Y. Song, J. Zhang, L. Zeng, C. Wang and W. Lin, *Nat. Catal.*, 2019, **2**, 709–717.
160 S. Kattel, P. Liu and J. G. Chen, *J. Am. Chem. Soc.*, 2017, **139**, 9739–9754.
161 Z. Feng, C. Tang, P. Zhang, K. Li, G. Li, J. Wang, Z. Feng and C. Li, *J. Am. Chem. Soc.*, 2023, **145**, 12663–12672.
162 P. G. O'Brien, A. Sandhel, T. E. Wood, F. M. Ali, L. B. Hoch, D. D. Perovic, C. A. Mims and G. A. Ozin, *Adv. Sci.*, 2014, **1**, 1400001.
163 Y. Cao, L. Gao, B. Wang, Y. Yao, C. Wu, Q. Shen, J. Feng, Y. Zhou, Z. Li and Z. Zou, *ACS Mater. Lett.*, 2022, **4**, 1912–1920.
164 Y. C. Tan, K. B. Lee, H. Song and J. Oh, *Joule*, 2020, **4**, 1104–1120.
165 X. Bian, Y. Zhao, G. I. N. Waterhouse, Y. Miao, C. Zhou, L.-Z. Wu and T. Zhang, *Angew. Chem., Int. Ed.*, 2023, **62**, e202304452.
166 C. Zhang, Z.-C. Shao, X.-L. Zhang, G.-Q. Liu, Y.-Z. Zhang, L. Wu, C.-Y. Liu, Y. Pan, F.-H. Su, M.-R. Gao, Y. Li and S.-H. Yu, *Angew. Chem., Int. Ed.*, 2023, **62**, e202305571.
167 B. Ren, Z. Zhang, G. Wen, X. Zhang, M. Xu, Y. Weng, Y. Nie, H. Dou, Y. Jiang, Y.-P. Deng, G. Sun, D. Luo, L. Shui, X. Wang, M. Feng, A. Yu and Z. Chen, *Adv. Mater.*, 2022, **34**, 2204637.
168 G. Wang, J. Chen, Y. Ding, P. Cai, L. Yi, Y. Li, C. Tu, Y. Hou, Z. Wen and L. Dai, *Chem. Soc. Rev.*, 2021, **50**, 4993–5061.
169 N. Kuhar, S. Sil and S. Umapathy, *Spectrochim. Acta, Part A*, 2021, **258**, 119712.
170 R. Beranek, *Adv. Phys. Chem.*, 2011, **2011**, 786759.
171 J. Kubota, Z. Ma and F. Zaera, *Langmuir*, 2003, **19**, 3371–3376.
172 L. Li, H. Guo, G. Yao, C. Hu, C. Liu, Z. Tian, B. Li, Q. Zhang and L. Chen, *J. Mater. Chem. A*, 2020, **8**, 22327–22334.
173 H. Mai, T. C. Le, D. Chen, D. A. Winkler and R. A. Caruso, *Chem. Rev.*, 2022, **122**, 13478–13515.
174 J. Hong, W. Zhang, J. Ren and R. Xu, *Anal. Methods*, 2013, **5**, 1086–1097.
175 Y. Xin, K. Yu, L. Zhang, Y. Yang, H. Yuan, H. Li, L. Wang and J. Zeng, *Adv. Mater.*, 2021, **33**, 2008145.
176 J. Yu, K. Wang, W. Xiao and B. Cheng, *Phys. Chem. Chem. Phys.*, 2014, **16**, 11492–11501.

 

177 R. Li, J. Hu, M. Deng, H. Wang, X. Wang, Y. Hu, H.-L. Jiang, J. Jiang, Q. Zhang, Y. Xie and Y. Xiong, *Adv. Mater.*, 2014, **26**, 4783–4788.
178 X.-B. Li, Z.-K. Xin, S.-G. Xia, X.-Y. Gao, C.-H. Tung and L.-Z. Wu, *Chem. Soc. Rev.*, 2020, **49**, 9028–9056.
179 A. Velty and A. Corma, *Chem. Soc. Rev.*, 2023, **52**, 1773–1946.
180 Y.-S. Xia, M. Tang, L. Zhang, J. Liu, C. Jiang, G.-K. Gao, L.-Z. Dong, L.-G. Xie and Y.-Q. Lan, *Nat. Commun.*, 2022, **13**, 2964.
181 S. Verma, S. Lu and P. J. A. Kenis, *Nat. Energy*, 2019, **4**, 466–474.
182 S. Kar, M. Rahaman, V. Andrei, S. Bhattacharjee, S. Roy and E. Reisner, *Joule*, 2023, **7**, 1496–1514.
183 E. Lam and E. Reisner, *Angew. Chem., Int. Ed.*, 2021, **60**, 23306–23312.
184 M. Li and S. Zhang, *ACS Catal.*, 2024, **14**, 6717–6727.
185 J. Fan, X. Yue, Y. Liu, D. Li and J. Feng, *Chem. Catal.*, 2022, **2**, 531–549.
186 M.-Y. Qi, Q. Lin, Z.-R. Tang and Y.-J. Xu, *Appl. Catal., B*, 2022, **307**, 121158.
187 L. Hong, H. Zhang, L. Hu, R. Xiao and S. Chu, *Sci. Adv.*, 2024, **10**, eadn9441.
188 T. Wang, L. Tao, X. Zhu, C. Chen, W. Chen, S. Du, Y. Zhou, B. Zhou, D. Wang, C. Xie, P. Long, W. Li, Y. Wang, R. Chen, Y. Zou, X.-Z. Fu, Y. Li, X. Duan and S. Wang, *Nat. Catal.*, 2022, **5**, 66–73.
189 H.-L. Wu, X.-B. Li, C.-H. Tung and L.-Z. Wu, *Adv. Mater.*, 2019, **31**, 1900709.
190 R. Zhai, L. Zhang, M. Gu, X. Zhao, B. Zhang, Y. Cheng and J. Zhang, *Small*, 2023, **19**, 2207840.
191 Bhawna, S. Kumar, R. Sharma, S. J. Borah, A. Gupta, M. K. Gupta, R. Kumar, K. K. Dubey, Y. K. Mishra and V. Kumar, *Sustainable Energy Fuels*, 2023, **7**, 4354–4395.
192 L. Yuan, M.-Y. Qi, Z.-R. Tang and Y.-J. Xu, *Angew. Chem., Int. Ed.*, 2021, **60**, 21150–21172.
193 B. Song, Y. Liang, Y. Zhou, L. Zhang, H. Li, N.-X. Zhu, B. Z. Tang, D. Zhao and B. Liu, *J. Am. Chem. Soc.*, 2024, **146**, 14835–14843.
194 K. Kadota, Y. Hong, Y. Nishiyama, E. Sivaniah, D. Packwood and S. Horike, *J. Am. Chem. Soc.*, 2021, **143**, 16750–16757.
195 F. Sastre, A. V. Puga, L. Liu, A. Corma and H. García, *J. Am. Chem. Soc.*, 2014, **136**, 6798–6801.
196 X. Meng, T. Wang, L. Liu, S. Ouyang, P. Li, H. Hu, T. Kako, H. Iwai, A. Tanaka and J. Ye, *Angew. Chem., Int. Ed.*, 2014, **53**, 11478–11482.
197 S. A. Chernyak, M. Corda, J.-P. Dath, V. V. Ordomsky and A. Y. Khodakov, *Chem. Soc. Rev.*, 2022, **51**, 7994–8044.
198 M. Mao, Q. Zhang, Y. Yang, Y. Li, H. Huang, Z. Jiang, Q. Hu and X. Zhao, *Green Chem.*, 2018, **20**, 2857–2869.